UNIVERSITY OF NAPLES FEDERICO II

AND

UNIVERSITY OF LISBON IST

PH.D. THESIS

IN

INFORMATION TECHNOLOGY AND ELECTRICAL ENGINEERING

Magnetic material characterization and magnet axis displacement measurement for particle accelerators

Supervisors:
Prof. Pedro Ramos
Prof. Annalisa Liccardo

Candidate:
Alessandro Parrella

2017 - 2018

To the memory of my beloved grandmother Maria

Abstract

Bending and focusing magnets, both normal- or super-conducting, are crucial elements for the performance of any particle accelerator. Their design requirements are always more tighten regarding components' misalignment and magnetic properties. This dissertation proposes new solutions for characterizing magnetic materials and monitoring solenoids' magnetic axis misalignments.
A superconducting permeameter is designed to characterize the new-generation superconducting magnet yokes at their operational temperature and saturation level. As proof of principle, the magnetic characterization of ARMCO® Pure Iron was performed at the cryogenic temperature of 4.2 K and a saturation level of nearly 3 T. A case study based on the new HL-LHC superconducting magnets quantifies the impact of the magnetic properties of the yoke on the performances of the superconducting magnets.
A flux-metric based method is proposed to identify the relative magnetic permeability of weakly magnetic materials. As proof of principle, the magnetic properties of the ITER TF coils quench detection stainless steel are analyzed. This method is not suitable to test materials with a relative permeability lower than 1.1. Hence, a measurement system based on a new magneto-metric method is conceived and validated employing a standard reference sample. The methods proposed in this thesis are currently employed at CERN's magnetic laboratory to face an increasing number of requests concerning not only the magnetic characterization of materials for magnets but also for shielding systems and compatibility of various components with high magnetic fields.
In this thesis, the results of the evaluation of ARMCO® Pure Iron as the yoke of the new LHC superconducting magnets and CRYOPHY as the magnetic shield for the cryomodule prototypes of HL-LHC Crab Cavities are reported.
Finally, a new Hall-sensor method is conceived and implemented for monitoring the coils alignment in multi-coil magnets, directly during their operation in particle accelerators. The proposed method is suitable even for those cases when almost the whole magnet aperture is not accessible. Requiring only a few measurements of the magnetic field at fixed positions inside the magnet aperture, the method overcomes the main drawback of the other Hall sensor-based methods which is having to deal with sturdy mechanics of the moving stages. The method is validated numerically on a challenging case study related to the Solenoid B of the project ELI-NP.

Keywords: Instrumentation for particle accelerators, characterization of magnetic materials, superconductivity and magnet protection, cryogenic measurements, superconducting magnets.

Sommario

I magneti per il bending e la messa a fuoco delle particelle, sia normali che superconduttori, sono elementi cruciali per le prestazioni di qualsiasi acceleratore. I loro requisiti di progettazione sono sempre più stringenti, in particolare riguardo al disallineamento e alle proprietà magnetiche dei loro componenti principali. Questa tesi propone nuove soluzioni per caratterizzare una vasta gamma di materiali magnetici e monitorare in tempo reale l'allineamento degli assi magnetici di solenoidi in operazione.
Un permeametro superconduttore è proposto per caratterizzare i nuovi yoke dei magneti superconduttori di ultima generazione a temperatura e livello di saturazione operativi. Come dimostrazione di principio, le proprieta' magnetiche di ARMCO® Pure Iron sono state misurate alla temperatura criogenica di 4,2 K e un livello di saturazione di circa 3 T. Un caso studio basato sui nuovi magneti superconduttori per HL-LHC quantifica l'impatto delle proprietà magnetiche dello yoke sulle prestazioni dei magneti superconduttori.
Inoltre, questa tesi propone un nuovo approccio, basato sul metodo flusso-metrico standard, per identificare la permeabilità magnetica relativa di materiali debolmente magnetici. Come dimostrazione di principio, vengono analizzate con successo le proprietà magnetiche dell'acciaio usato per la quench detection delle bobine di ITER TF. Tuttavia, questo metodo non è adatto per testare materiali con una permeabilità relativa inferiore a 1.1. Un sistema di misurazione basato su un nuovo metodo magneto-metrico è stato, quindi, proposto, implementato e validato tramite l'utilizzo di un campione standard di riferimento.
I metodi proposti in questa tesi sono attualmente impiegati presso il laboratorio di misure magnetiche del CERN per far fronte ad un numero crescente di richieste riguardanti non solo la caratterizzazione magnetica di materiali per magneti ma anche sistemi di schermatura e compatibilità di vari componenti con alti campi magnetici.
In questa tesi si riportano le analisi sperimentali delle proprieta' magnetiche di ARMCO® Pure Iron, materiale utilizzato come yoke dei nuovi magneti superconduttori nell'LHC e CRYOPHY, materiale utilizzato come scudo magnetico per i prototipi delle Crab Cavity.
Infine, un nuovo metodo basato su sensori ad effetto Hall è stato concepito ed implementato per monitorare l'allineamento delle bobine nei solenoidi multibobina direttamente durante il loro funzionamento negli acceleratori di particelle. Il metodo proposto è adatto anche per quei casi in cui quasi tutta l'apertura del magnete non è accessibile. Il metodo è validato numericamente su un caso studio relativo al solenoide B del progetto ELI-NP.

Keywords: Strumentazione per acceleratori di particelle, caratterizzazione di materiali magnetici, superconduttività e protezione da quench, misure criogeniche.

Resumo

Os ímanes de focagem e direcionamento, normais e supercondutores, são elementos cruciais para o desempenho de qualquer acelerador de partículas. Os requisitos para o seu desenvolvimento são sempre mais rígidos em relação ao correto alinhamento dos seus componentes e às suas propriedades magnéticas. Esta dissertação propõe novas soluções para caracterizar materiais magnéticos e monitorizar os desalinhamentos em eixos magnéticos de solenoides.
Um instrumento capaz de medir a permeabilidade é projetado para caracterizar as armaduras de ímanes supercondutores de nova geração na sua temperatura de operação e os seus níveis de saturação. Numa fase inicial, a caracterização magnética do material ARMCO Pure Iron foi realizada à temperatura criogénica de 4,2 K e um nível de saturação de aproximadamente 3 T. Um estudo baseado nos novos ímanes supercondutores para o HL-LHC quantifica o impacto das propriedades magnéticas das armaduras no desempenho dos ímanes supercondutores.
Um método fluxométrico é proposto para caracterizar a permeabilidade magnética relativa de materiais com baixas propriedades magnéticas. Como prova de conceito, as propriedades magnéticas do aço ITER TF são analisadas. Este método não é adequado para testar materiais com uma permeabilidade relativa inferior a 1,1. Assim, um novo sistema de medição foi desenvolvido e validado usando uma amostra de referência padrão. Ambos os métodos são particularmente adequados para a produção em série industrial: a duração e o custo da medição são drasticamente reduzidos em comparação com os métodos tradicionais VSM e AGFM de última geração.
Os métodos propostos nesta tese são atualmente usados no laboratório magnético do CERN para responder a um número crescente de solicitações não apenas para a caracterização magnética de materiais para ímanes, mas também para sistemas de proteção e compatibilidade de vários componentes sujeitos a campos magnéticos elevados.
Nesta tese, os resultados da avaliação do uso do material ARMCO como armadura dos novos ímanes supercondutores do LHC e CRYOPHY, assim com o escudo magnético para os protótipos do HL-LHC são analisados e documentados.
Finalmente, um novo método com um sensor Hall é desenvolvido e implementado para monitorizar o alinhamento de bobinas em ímanes de bobinas múltiplas, diretamente durante sua operação em aceleradores de partículas. O método proposto é adequado mesmo para casos em que quase toda a abertura do íman não é acessível. Exigindo apenas algumas medições do campo magnético em posições fixas dentro da abertura magnética, o método supera a principal desvantagem dos outros métodos baseados em sensores Hall, que é ter que lidar com a mecânica robusta dos componentes em movimento. O método é validado no caso

da Solenoide B do projeto ELI-NP.

Keywords: Instrumentação para aceleradores de partículas, caracterização de materiais magnéticos, supercondutividade e proteção contra têmpera, medidas criogênicas, ímanes supercondutores.

List of publications

Journal publications:

[1] Arpaia P, Celano B, De Vito L, Esposito A, Parrella A, Vannozzi A, *Measuring the magnetic axis alignment during solenoids working*, **Nature Scientific Reports**, Volume 8, Number 11426, July 2018.

[2] Arpaia P, Celano B, De Vito L, Esposito A, Parrella A, Vannozzi A, *On-field monitoring of the magnetic axis misalignment in multi-coils solenoids*, **IOP Journal of Instrumentation**, Volume 13, Number 8, August 2018.

[3] Arpaia P, Buzio M, Liccardo A, Parrella A, Pentella M, Principe M, Ramos P, *Magnetic properties of pure iron for the upgrade of the LHC superconducting dipole and quadrupole magnets*, **IEEE Transaction on Magnetics**, published online in October 2018, doi: 10.1109/TMAG.2018.2872163.

[4] Arpaia P, Buzio M, Capatina O, Langeslag S, Eiler K, Parrella A, Templeton N, *Effects of temperature and mechanical strain on Ni-Fe alloy CRYOPHY for magnetic shields*, **Journal of Magnetism and Magnetic Materials**, published online in December 2018, doi: 10.1016/j.jmmm.2018.08.055.

[5] Arpaia P, Buzio M, Liccardo A, Parrella A, Pentella M, Ramos P, *A superconducting permeameter for characterizing soft magnetic materials at high fields*, submitted to **Journal of Magnetism and Magnetic Materials**, 2018.

Conference proceeding:

[1] Parrella A, Arpaia P, Buzio M, Liccardo A, Ramos P, *Inverse Problem-Based Magnetic Characterization of Weakly Magnetic Alloys*, IPAC'17, Copenhagen, 2017.

[2] Arpaia P, Celano B, De Vito L, Esposito A, Moccaldi N, Parrella A, *Monitoring the magnetic axis misalignment in axially-symmetric magnets*, IEEE I2MTC, Houston, 2018, doi: 10.1109/I2MTC.2018.8409851.

[3] Eiler K, Parrella A, Arpaia P, Buzio M, Capatina O, Langeslag S, Templeton N, *Characterization of Magnetic Shielding Material for HL-LHC Crab Cavities*, SRF2017, Lanzhou, 2017.

[4] Arpaia P, Buzio M, Liccardo A, Parrella A, *On the Use of Flux-metric Methods for Characterizing Feebly Magnetic Materials*, IEEE I2MTC Conference Proceedings, Turin, 2017, doi: 10.1109/I2MTC.2017.7969928.

[5] Anglada J, Arpaia P, Buzio M, Liccardo A, Parrella A, Pentella M, Ramos P, *On the importance of magnetic material characterization for the design of particle accelerator magnets*, **Journal of Physics Conference Series**, Vol. 1065, No. 17, 2018, doi:10.1088/1742-6596/1065/5/052045.

Acknowledgements

The research presented in this thesis was carried out at CERN's magnetic laboratories in the framework of the Doctoral Student Programme, under a co-tutelage agreement between the University of Lisbon (Instituto Superior Técnico, Portugal) and the University of Naples ("Federico II", Italy). For three years I have been working in the magnetic measurement section of the CERN technology department (TE-MSC-MM), collaborating with the Instituto de Telecomunicações (Portugal) and the DIETI (Naples). I want to express my gratitude to all the people who made this agreement possible and effective.

I am profoundly pleased to thank my mentor, Prof. Pasquale Arpaia, for the very precious academic supervision of this thesis and for the opportunity to start my career at CERN, teaching me to embrace new challenges without fear and "to turn problems into opportunities".

My gratitude also goes to my CERN supervisor Dr Marco Buzio. I am really grateful to him for having always believed in me. Thanks for the constant guidance and all the excellent advice and opportunities for professional growth you have given to me.

I want to thank my University tutor, Prof. Pedro Ramos and Prof. Annalisa Liccardo for the academic supervision of this thesis and all the huge help they gave me during these years.

I would also like to express my gratitude to prof. Luca De Vito, Antonio Esposito and Alessandro Vanozzi for all the effort they have invested in the so-called "ELI project". I really appreciated being part of this team.

My thanks also go to Mariano Pentella, the first student I was responsible for, but also and mostly a precious friend. I enjoyed sharing the office and the several projects we dealt with. I wish for you all the best in your future career.

I would also like to thank my colleagues from the Magnetic Measurement section at CERN. I enjoyed all the vivid discussions we had, both professional and not-professional. During the many discussions regarding my work, I received several valuable advice and help from Stephan Russenschuck, Lucio Fiscarelli, Carlo Petrone, Giuseppe Montenero, Ernesto De Matteis, Giancarlo Golluccio, Mario Kazazi, Marco Roda and Domenico Caiazza. A special thank goes to Gianni Caiafa, the companion of this PhD adventure.

Furthermore, my acknowledgements go to the colleagues of the magnetic measurement workshop for all the technical support they always have provided. A special thanks to Ricardo Mercardillo for all the help and the samples he has wound for the experiments reported in this dissertation.

I also want to say thanks to Torsten Koettig, Sebastian Prunet and all the colleagues of the Cryolab for their help with the cryogenic experiments. Rosario Principe for the collaboration during the characterization of ARMCO for HL-LHC magnet. Lorenzo Bortot and Edvard Stubberurd for the help with quench protection simulations. Jaime Renedo Anglada and Susana Izquierdo Bermudez for the help with FE simulations.

Alessandro Parrella

Contents

Chapter 1

Introduction

Next-generation particle accelerators will produce a high number of collisions at very high energy, allowing the observation of new or rare phenomena of particle physics. This will be made possible by increasing the “luminosity” and the “beam energy”, the key performance parameters of an accelerator [67]. Inside the “European strategy for particle physics”, major examples of these technological trends are the High Luminosity Large Hadron Collider (HL-LHC) and the High Energy LHC [81].
Precise and accurate measurement of the permeability, coercivity and resistivity of magnetic materials is of paramount importance to design and qualify accelerator magnets. A few national and private metrology laboratories offer this kind of measurements on the market. However, they typically have long lead times, limited capability to adapt to special needs and high cost. The MSC (Magnets, Superconductors and Cryostats) group at the European Center for Nuclear Research (CERN) is facing an increasing number of requests concerning not only the magnetic characterization of materials for magnets, but also for shielding systems and compatibility of various components with high magnetic fields. Many of these applications stretch the envelope of test parameters beyond what is covered by international standards in terms of the range of values (accurate measurement of very low permeability), sample shape (such as wires, tapes or tubes, both in open and closed magnetic circuits) and volume (from a few grams of material to full-scale magnet yokes). Hence, an extensive upgrade of the instrument range of the CERN magnetic measurement laboratory has been necessary not only to adapt to these demands but also to face the campaigns of series tests as required by the High Luminosity upgrade of the Large Hadron Collider.
The CERN LHC is the world’s largest and most powerful particle accelerator. The LHC consists of a 27-kilometer ring of normal and superconducting magnets with a number of accelerating structures to boost the energy of the particles along the way. Inside the accelerator, two high-energy particle beams travel at close to the speed of light before they collide. The beams are guided around the accelerator ring by a strong magnetic field maintained by superconducting electromagnets, that requires an operational temperature of 1.9 K. Thousands of magnets of different varieties and sizes are used to direct the beams around the accelerator. These include 1232 dipole magnets 15 m in length which bend the beams, and 392 quadrupole magnets, each 5–7 m long, which focus the beams. Just prior to the collision, another type of magnet is used to "squeeze" the particles closer together to increase the chances of collisions. Magnetic materials are important elements

in the fabrication of magnets and take an important part in the overall accuracy. The selection of these materials and the development of measurement systems to support this selection have been considered carefully since the beginning of CERN.
The HL-LHC [31] is a project to upgrade the LHC to maintain scientific progress and exploit the LHC's full capacity [115]. By increasing its peak luminosity by a factor of five over nominal value, it will be possible to reach a higher level of integrated luminosity, nearly ten times the initial LHC design target. The HL-LHC will explore new beam configurations and new advanced technologies in the domain of superconductivity, cryogenics, rad-hard materials, electronics and remote handling.

Stronger superconducting dipole magnets will be installed in the dispersion

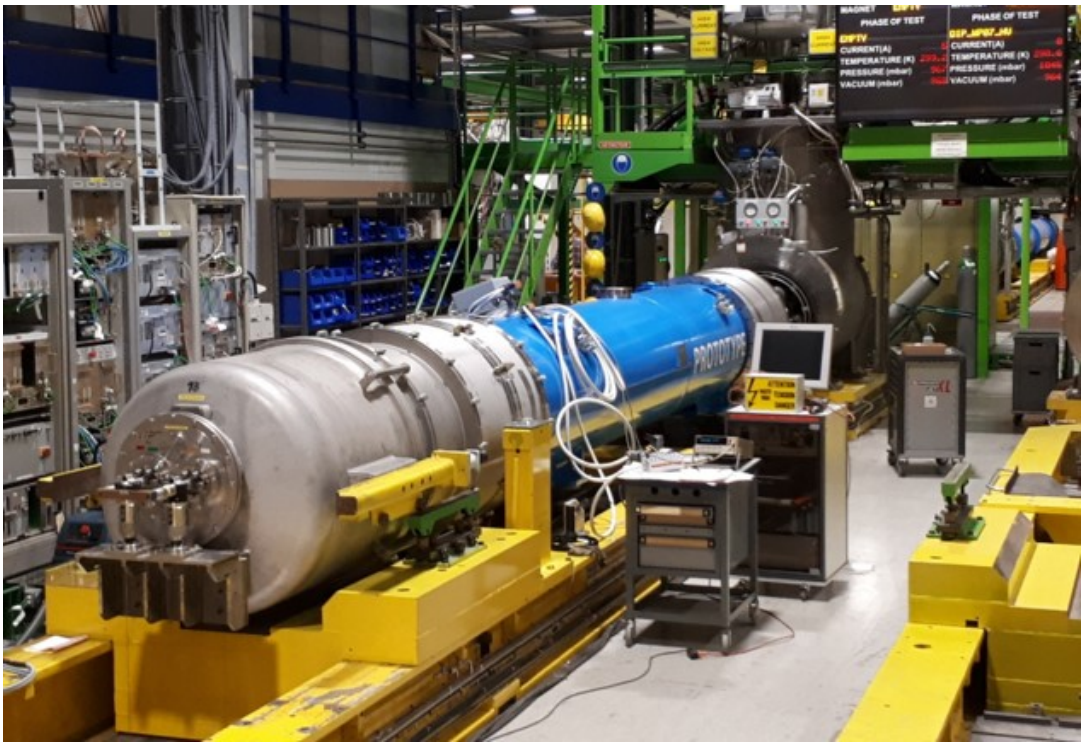

FIGURE 1.1: First Nb_3Sn magnet on the CERN cryogenic test facility (SM18) horizontal bench

suppression zone to make space for additional collimators that protect the superconducting magnets [134, 7]. The nominal magnetic field of the dipole magnets will increase from 8.6 T to 11.2 T. In Fig. 1.1 the first Nb_3Sn magnet's test at the CERN cryogenic test facility (SM18) horizontal bench is shown. New superconducting quadrupole magnets will be installed in the insertion region to increase the focusing properties of the machine, reaching the goal of a much higher luminosity. The nominal field gradient of the new inner triplet quadrupole magnets will change from 200 T/m in an aperture of 70 mm to 132.6 T/m in an aperture of 150 mm [29]. In Fig. 1.2 the flux density in the cross-section of a 11 T dipole magnet for HL-LHC [122] and of the MQXF inner triplet quadruple are shown. In proximity of the coils, the iron yoke shows a level of flux density higher than

3 T. This is due to the higher field generated in the aperture (11 T). The iron yoke

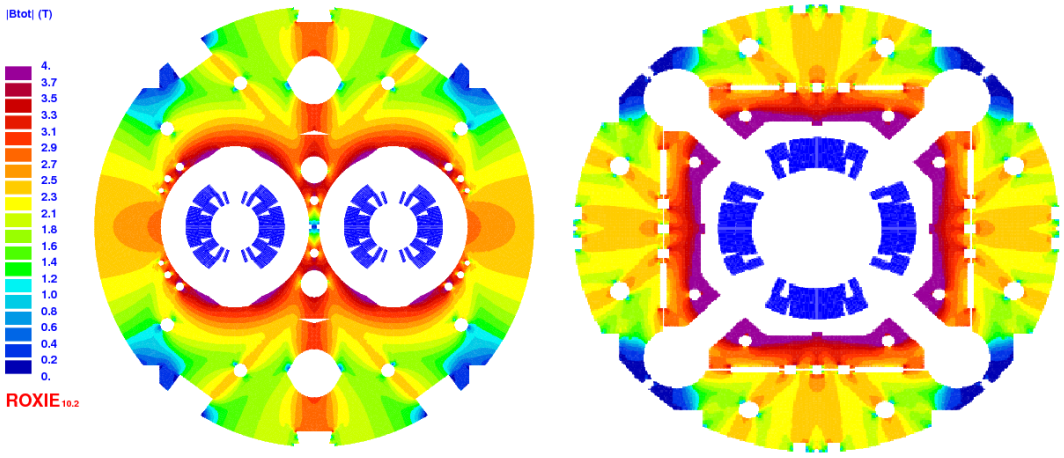

FIGURE 1.2: Flux density in the cross section of MBH 11 T dipoles (left) and in the MQXF quadrupole (right) for HL-LHC.

of a superconducting magnet is one of the key elements for its correct operation because it supplies the return path for the magnetic flux and, at the same time, gives mechanical rigidity to the cold mass.
In the past, low-carbon steel, known under the trade name MAGNETIL BL™ and produced by Cockerill Sambre-ARCELOR Group [61], was used for the production of the iron yoke laminations of the LHC main magnets. The magnetic characterization of this material is described in [20, 23]. This would have been the ideal choice also for the new HL-LHC magnets if it had still been available at the moment of the tender. Instead, ARMCO® Pure Iron Grade 4 produced by AK Steel has been chosen. 1800 tonnes of ARMCO® Pure Iron, to be used mainly for the single aperture Nb_3Sn quadrupole magnets (inner triplet) MQXF [50] and 11 T Nb_3Sn dipole magnets [122], needs to be firstly procured and then characterized magnetically to check that it satisfies certain requirements and quality control standard. The HL-LHC magnet specifications prescribe $B > 0.2$ T at $H = 40$ A/m, $B > 1.5$ T at $H = 1200$ A/m and $B > 2$ T at $H = 24000$ A/m.
Considering the increasing level of flux density in these new magnets, see Fig.1.2, a characterization of ARMCO behavior for magnetic fields above 24 kA/m and at a temperature of 4.2 K is necessary to understand the behavior of the magnets at the new operating conditions.
The increase of luminosity will cause an increment of the radiation dose inside the accelerator. The magnets most affected by this higher level of radiation are the LHC Warm Bending Magnets (MBW) and Warm Quadrupole Magnets (MQW) [4]. Protection of these normal conducting magnets in the LHC aims to reduce the radiation dose received by the magnet's coils and increase their lifespan. This will be done by specially manufactured Tungsten Heavy Alloy (WHA) pieces [3]. The selected commercial material, INERMET® IT180 [110] contains 5% of nickel and copper in unspecified proportion and it is marketed as non-magnetic. However, according to the available literature, its magnetic properties depend critically on

the precise composition. Even if slightly paramagnetic, an eventual residual magnetization of this material could interfere with the magnetic field generated by the magnets and decrease the whole accelerator performance. Therefore, magnetic testing of the actually delivered pieces will be necessary. In particular, CERN has requested that the tungsten alloy used as radiation shield shows a relative magnetic permeability, μ_r, lower than 1.005.
One of the main difficulties with accelerators is that the magnetic field that keeps particles in orbit must have the same configuration and intensity in all the dipoles. But when the magnets are on, a very strong force is produced, a force that can deform the 'soft' parts of the magnets, such as superconducting coils. The force loading one meter of a dipole is about 400 tonnes (comparable with the weight of a Boeing 747), hence a huge deformation would occur without a mechanical component to keep the whole structure rigid. This component is the collar situated around the superconducting coils to prevent undesirable movements of the conductors. The collars must have well-defined geometry and physical properties to confine the coils, to avoid deformations, and have consistent behavior when exposed to extreme heat and magnetic fields. The problem has been solved using a particular alloy, belonging to the class of austenitic steels, that has all the properties required: good thermal contraction and magnetic permeability. The material the collars are made of has to have a μ_r, lower than 1.003 to do not interfere with the flux density generated by the coil, as can be seen in Fig. 1.2. Hence, magnetic testing of the actually delivered pieces will be necessary also in this case.
Moreover, the High-Luminosity upgrade of the LHC will also exploit *crabbing* [133] for increasing and leveling the luminosity of the Large Hadron Collider (LHC). The idea is to deflect proton bunches so that their tilt at collision compensates for their crossing angle. This is achieved with bulk niobium superconducting radio frequency (SRF) cavity cryomodules to be installed before the interaction points. Before Hi-Lumi definitive commissioning, one pair of these deflecting (or *crab*) cavities has been successfully tested within a cryomodule with a proton beam in the Super Proton Synchrotron (SPS) at CERN in 2018 [31, 142]. Superconducting radio frequency (SRF) is considered as a promising technology in modern particle acceleration [46]. However, to guarantee optimum performance with a high quality factor, the initial magnetic field on RF surfaces of superconducting cavities should be minimized [41], [90]. In fact, in cryomodules for the SRF cavity, magnetic shielding is a key technology [35]. Materials with a very high maximum relative permeability are used as passive magnetic shields: the magnetic flux is forced into the shielding material, and thus the magnetic field is canceled inside the shield, where SRF cavities are operating. The shield is sometimes immersed in liquid helium at cryogenic temperatures, in order to be placed as close as possible to the SRF cavity. The cryogenic environment influences magnetic properties, and special magnetic shielding materials have been designed for use in liquid helium [66], [63]. The initial magnetic properties, and therefore the performance of the magnetic shield, depend mostly on its composition as well as on the applied heat treatment. The magnetic shielding in the crab cavity cryomodule is critical for achieving the operational stability required for HL-LHC. A solution with two layers of magnetic shielding consisting of a "warm" shield

in the vacuum around the helium tanks, made of MuMetal, and a "cold" shield inside the helium tank directly around the cavity, made of Ni-Fe alloy Cryophy, has been developed for the SPS prototype cryomodule [133]. A magnetic survey in the SPS concluded that an external field of no more than 200 μT is to be expected during operation [22]. This estimate includes the effect of the earth's magnetic field and neighboring magnets. Hence, the magnetic shields were designed to ensure that no more than 1 μT reaches the cavity surface, with an external field of 200 μT in the worst-case orientation [133]. The magnetic shield performance is strongly influenced by the material properties. Specifically, the design requirement for the cold shielding material is a relative magnetic permeability of minimum 10^5 at liquid helium temperature [5]. For the inner layer of the Crab Cavities' cryomodule, the Ni-Fe alloy Cryophy [1] has been used to reach optimum performance at cryogenic temperature [133]. Several works on magnetic shields and the related materials have been presented in literature, see Section 2.2.2. However, a magnetic characterization of the alloy Cryophy focused both on temperature and mechanical strain dependence, is not available [120].
Finally, accelerators performance is limited by "linear imperfections" induced by components misalignment and magnetic field errors. Therefore, the constraints on the position of the components for focusing, accelerating, or detecting the beam all along the accelerator must be increased and tightened [139]. These components are usually large and heavy, weighing often more than 100 kg and measuring several meters in length. They will have to be aligned to within a few of microns over a distance of several hundreds of meters. In the last decades, several methods have been developed to cope with the alignment of accelerator components [87, 95]. Of high importance is the alignment of focusing elements, mainly quadrupole and solenoid magnets. While several methods have been developed and successfully applied to the alignment of quadrupole magnets [137], several problems arise from standard methods for solenoids [13, 12]. For instance, the single-stretched-wire method, a standard method for finding quadrupole magnets' magnetic axis, has much lower sensitivity when applied to solenoids, because the intercepted transversal field components are significant only at the magnet's ends [11]. When a magnet is in operation, its coils are constantly subject to an electrodynamic strain. The main reason resides in deformations caused by thermal effects, even with the installed cooling system. This could result in a significant misalignment of the magnetic axis from the geometric axis. The thermal effects are especially present at the magnet start-up, but the misalignment can drift also during machine runnings, because of the heat generated by particle beams. Furthermore, when dealing with multi-coil solenoids, each coil may be affected by its peculiar misalignment. Hence, these misalignments have to be monitored when a strict constraint on the coils alignment is required, thus allowing to adjust the position of the coils to achieve/recover the solenoid design parameters. For instance, within the European project "ELI Nuclear Physics" (ELI-NP) [47], this can be done with adjustable screws to translate and/or rotate a single coil, even during its operation. This system provides six degrees of freedom, and the desired position can be totally recovered on-line with a precision of tens of micrometers. Most of the standard methods for the solenoid

axis identification are useless for on-line monitoring, owing to their need of accessing a wide area of the solenoid's air gap (evidently, almost full of the beamline and auxiliary accessories).

The research presented in this thesis proposes new solutions in the framework of magnetic material and axis displacement measurements for the challenges presented in this chapter. The structure of the thesis is as follows

- **Chapter 1: Introduction**, where the problem statement that motivated this research is explained.
- **Chapter 2: State of the art**, where the content of the work is introduced. After a review of the principal materials for particle accelerator magnets, a literature overview of methods for characterizing magnetic materials and for measuring magnetic axis displacements is presented.
- **Chapter 3: Proposal for characterizing soft magnetic materials**, where the measuring principle of the flux-metric method and the enhancements carried out in this work, in terms of measurement procedure and drift correction are illustrated. Firstly, the design aspects of the experimental supporting technologies for data acquisition and analysis are described. Then, a solution for characterizing soft magnetic materials at the operational temperature of 4.2 K and at a saturation level near 3 T is proposed. The measurement system employs superconducting coils. Hence, specific quench detection and magnet protection simulations are carried out.
- **Chapter 4: Proposal for characterizing weakly magnetic materials**, where a flux-metric based and a magneto-metric methods are proposed for characterizing weakly magnetic materials with a permeability between 1.1 and 6.0 and lower than 1.005, respectively. The former method is an adapted-to-low-permeability-materials approach based on the standard flux-metric method for soft magnetic materials previously introduced. The latter is a novel method based on inverse analysis approach coupled with a finite-element model.
- **Chapter 5: Proposal for monitoring magnetic axis misalignments**, where a novel Hall transducers-based method is proposed for the on-line monitoring of solenoids' magnetic axis. In particular, the basic idea and the mathematical formulations of the method in the case of a single-coil and a multi-coil solenoid are presented.
- **Chapter 6: Validation of the proposed method for soft magnetic materials**, where the proposed measurement system based on the flux-metric approach, are employed for characterizing two soft materials, namely, ARMCO for magnet yokes and CRIOPHY for magnetic shields. The importance of magnetic material measurements in the framework of the design of magnets for particle accelerator is discussed, as well.

- **Chapter 7: Validation of the methods for weakly magnetic materials**, where the proposed flux-metric method is validated on a series production of co-wound 1.430 stainless steel tapes for the quench detection in ITER TF coils and the proposed magneto-metric based method is validated by using a reference alloy sample with a known relative magnetic permeability.
- **Chapter 8: Validation of the proposed magnetic axis monitoring method**, where the proposed Hall sensors-based method for the real-time monitoring of single-coil and multi-coil solenoids is validated with a case study based on the requirements of the European project ELI-NP.
- **Chapter 9: Conclusions**, where the conclusions and future perspectives are outlined.

Chapter 2

State of the Art

This chapter summarizes the content of this PhD research. In particular, the most important materials for particle accelerator magnets are briefly reported and a literature overview of methods for their magnetic characterization is presented. Then, an overview of methods for measuring magnetic axis displacements are given. Finally, the objectives of this thesis are pointed out.

2.1 Materials for particle accelerator magnets

Magnetic materials are fundamental in satisfying the basic demands of our society, such as the generation, distribution, and conversion of electrical energy, the storage and retrieval of information, and even in media, telecommunications and biomedical applications. Nowadays, magnetic materials generate a market, whose value exceeds 10^{10} euros [52].
An in-depth treatment of magnetic materials goes well beyond the scope of this work. A general introduction to the magnetic properties of materials can be found in the text by Cullity an Graham [40]. The text by Bozorth [30] is a standard reference, where an overview of the magnetic properties of different materials can be found. Finally, the volume of O'Handley [34] and the comprehensive Handbook of Magnetism and Advanced Magnetic Materials [82] cover a number of advanced materials, including amorphous and nanocrystalline materials and advanced soft magnetic materials for power application.
This thesis is focused on the characterization of materials for particle accelerators. Before reviewing the measurement systems of magnetic materials mostly used in particle accelerators, it is necessary to survey those materials briefly. In particle accelerators, Iron-based alloys are widely employed for cores of accelerator and experiment magnets; Iron-nickel alloys are typically used as shields for the vacuum chambers of accelerator injection and extraction septa; soft spinel ferrites are used in collimators to damp trapped modes; nanocrystalline materials are envisaged for high-frequency transformers and amorphous materials for induction cores of heavy-ion inertial fusion-energy accelerators.
In particular, three categories have been distinguished and treated in this dissertation: i) materials for magnetic yokes, ii) materials for magnetic shielding and iii) weakly magnetic materials.

2.1.1 Soft magnetic materials for magnet yokes

Ferromagnetic materials are classifiable in two groups: Soft and hard magnetic materials. The difference between the two groups regards mainly the coercitive field, thus the current necessary to bring the magnetization of the sample to zero. As reported by Bozorth in [30], soft magnetic materials are defined as materials with high permeability and easy to be magnetized and demagnetized. Vice-versa, hard magnetic materials are defined as materials challenging to be magnetized. This means that the difference between the two categories of material stays mainly in the value of coercitivity. For a soft magnetic material, the value of coercitivity is typically lower than 1000 A/m. The value of the peak permeability is typically higher or much higher than 1000 and the value of the initial relative permeability is typically greater than 500. These materials are commonly used for applications such as electrical machines or electro-magnets as iron yokes, to give the return path to the flux lines due to their high permeability. In order to minimize the hysteresis effects, the coercitivity of a material used in the core of an accelerator magnet is desired to be as small as possible. Usually, materials with coercivity smaller than 100 A/m are used. For a hard magnetic material, the value of coercitivity is much higher than 1000 A/m, with values of about 800 kA/m for NdFeB magnets and 3.3 MA/m for SmCo magnets. This property of conserving their magnetic state makes hard magnetic material suitable for the application of the magnetic memories. Moreover, because of the remanent field in the range of [0.8, 1.8] T, they are also used as excitation poles of the electrical motors.
Hard magnetic materials will not be treated in this thesis, where the focus will be given to soft magnetic materials. In particular, the properties of two groups of soft magnetic materials related to the fabrication of magnets' yoke and magnetic shielding will be presented in the following paragraphs and next section, respectively.

Pure iron and low carbon steel for large accelerator DC magnet yokes

As reported by Sgobba in [124], a 'Pure iron' is an iron where the total concentration of impurities (mainly C, N, O, P, S, Si and Al) does not exceed a few hundred ppm. An example of the impurities of a Pure Iron, ARMCO® from AK Steel, is given in Tab.2.1. Otherwise, it is preferably referred to as low-carbon steel.
Very pure iron features a high electrical conductivity which makes it unsuitable for AC applications, due to the iron losses, its poor mechanical properties and its cost. When a few percentage of Si and Al are introduced in the alloy, it is usually referred to as "silicon steels". Fiorillo [52] reports several values for the magnetic properties of pure iron and low-carbon steels, shown in Tab.2.2. Generally, coercitivity values lower than 150 A/m and peak relative permeability significantly higher than 1000 are expected.

Saturation magnetization, depending only on the ferrite content in the lattice, is not influenced by the purity of the iron or by the operational temperature. Instead, impurities of the iron strongly influence coercitivity and relative permeability. Values of initial and maximum permeability typically drop for cold

Composition	Max. Analysis %
Carbon (C)	0.005
Manganese (Mn)	0.060
Phosphorus (P)	0.005
Sulfur (S)	0.003
Nitrogen (N)	0.005
Aluminum (Al)	0.005
Nickel (Ni)	0.03
Chromium (Cr)	0.03

TABLE 2.1
Impurities composition in ARMCO® Pure Iron Grade 4. [source: AK steel datasheet]

Material	H_c [A/m]	μ_{ri}	μ_{rp}
Ingot (99.8% Fe)	112	10	1000
ARMCO	80	200	7000
Commercially pure	20-100	200-500	3500-20000
Carbonyl iron powder	6	3000	20000
Vacuum-melted	25	-	21000
Electrolytic	7	1000	26000
Electrolytic annealed	18	-	41500
Vacuum-smelted and hydrogen-annealed	3	-	88400
Purified ARMCO (99.5% Fe)	4	10000	227000
Vacuum-annealed	-	14000	280000
Single-crystal	-	-	680000
Single-crystal, magnetically annealed	12	-	1430000

TABLE 2.2
Typical values of the magnetic parameters of soft magnetic materials. [52]

worked material, whereas coercitivity increases. Annealing cycles allow to improve magnetic properties or restore them by reducing internal strains, increasing the grain size and allowing better diffusion of the impurities. Two are the classes of anneals used commercially: Anneals below $900°C$ and anneals at or about $925°C$ or higher to promote grain growth. These anneals should be followed by slow cool. For further details about metallurgy and annealing processes, reference is made to the dedicated literature [60].

Low-carbon steel for LHC magnets yokes

For applications that require good magnetic properties but at a reasonable cost, low-carbon steels are frequently used. As reported by Fiorillo in [52], low-carbon steels for magnetic cores are generally produced as sheets, through a sequence of hot and cold rolling and thermal treatments. In order to improve the magnetic

properties, the laminations are often decarburized. Performance of low-carbon steels is described typically as AC magnetic properties at industrial range frequencies. In the absence of any purification treatments and high considerable silicon content, AC losses at 60 Hz and 1.5 T can reach 15 W/kg, with a relative permeability of $\mu_r = 500 - 1000$. The addition of roughly 1% of silicon combined with a proper composition control allows reducing power loss to 8 W/kg with a relative permeability of roughly 2000. Typically, they are delivered in laminations with a final thickness of 0.50-0.85 mm. Contrary to high-purity irons, low-carbon steels are affected by magnetic aging, where for aging it is intended an increase of the coercivity that occurs with time, due to the formation of cementite precipitates that give rise to domain wall pinning. Cementite is a phase of the steel where carbon is deposited on the boundary of the grains: since carbon is a diamagnetic material, this creates a domain wall pinning. Generally, pure iron and non-alloyed steels are mostly used for DC and quasi-DC magnets for their low-cost and because power losses are not considered.

Iron-silicon alloys for steering and corrector magnet yokes

The addition of few percents of silicon to a decarburized low-carbon steel changes the iron properties considerably. Silicon steels are classifiable in two groups: non-oriented and grain-oriented silicon steels. Non-oriented silicon steels are soft magnetic materials with isotropic grain texture, which covers the applications of the electrical rotating machines, where the isotropy of the material is strongly recommended. Grain-oriented silicon steels, differently from the non-grain oriented, exhibits a preferential direction of magnetization: this means that they are anisotropic and have minimum coercitivity and maximum permeability when magnetized in their preferential direction. The application of grain-oriented steels is restricted to most of the transformers cores, where it is necessary to have the best performances along the rolling direction, that gives the return path to the magnetic flux. A first advantage is that the electrical resistivity increases at a rate of 5x10^{-8} Ωm per soluted atomic percent, improving in this way the material performance in AC for the power losses. Other advantages of Silicon-iron alloys are availability, punchability, precisely defined characteristic, and low coercitivity value, an essential feature for the linearity of magnets working with variating fields of either polarity. As a drawback, it is possible to register a reduction of the saturation magnetization (from 1.6 T of low-carbon steels to 1.4-1.5 T) and higher costs. This is the reason why low carbon steels are preferred for large-scale magnet yokes, while silicon-iron are used for small magnet yokes such as steering and corrector magnet yokes.

2.1.2 Soft magnetic materials for magnetic shielding

Magnetic shielding is of paramount importance for guaranteeing good performance of cryomodules in particle accelerators. The effect of stray magnetic fields on the quality factor(Q_0 of the superconducting radio frequency (SRF) cavity is regulated by the following equation [119]: $Q_0 = \frac{G}{R_s}$, where G is the geometric

factor of the cavity and R_s is the cavity resistance. The latter can be divided into two contributions, namely the surface magnetic field (R_H) and other components. The R_H is directly proportional to the external magnetic field that, in case we consider only the earth's magnetic field, is roughly $50\ \mu T$. Hence, a high stray magnetic field increases the cavity surface resistance, causing a degradation of the cavity's quality factor. The standard way to prevent this is by employing magnetic shields [99]. Two classes of magnetic shields are generally employed, namely active shield [27] and passive shield [86]. The former is based on the use of a superconducting coil to generate a magnetic field that cancels out an eventual external magnetic field. The latter that provides a path for the field lines around the shielding volume, and minimizes the magnetic field inside the cryomodules, by drawing the field onto itself.
Materials with a very high maximum relative permeability are used as passive magnetic shields. The shield is sometimes immersed in liquid helium at cryogenic temperatures. The magnetic shielding in the HL-LHC crab cavity cryomodule is made of CRIOPHY. A registered trademark of Aperam, CRIOPHY is a Ni-based ferromagnetic alloy, namely 81% of Fe, 14% of Ni, and 5% of Mo in weight. It is specifically aimed to maximize magnetic permeability at cryogenic temperatures, by a tailored composition and a defined heat treatment. Cryophy is very similar in most properties to MuMetal (ASTM A753, alloy 4), which is used as the 'warm' magnetic shielding of the crab cavities outside of the helium tank. In general, Nickel-iron alloys present a wide range of behaviors depending on the percentage of nickel, in the range from the 35% to 80%. The percentage of nickel is what influences mostly the magnetic properties, giving an extensive range of possible application for such materials. For example, at a concentration of 36% it is possible to observe a significant drop of the Curie temperature which reaches a value of 230 °C, which increases the resistivity (75x10^{-8} Ωm) and makes the material performant at high frequencies. An alloy with this nickel content is mostly used for radar pulse transformers (Fe64-Ni36). By increasing the content of nickel at a value of 50% (Fe50-Ni50), the saturation polarization is of 1.6 T. Using thermal treatments [52], it is possible to achieve a squared hysteresis cycle, compatible with the application of magnetic amplifiers. With a content of nickel that keeps increasing, at a value of 55-60%, by annealing under a transverse saturation field, it is possible to achieve a remanent flux density of 0.9-1.2 T, compatible with the use of unipolar pulse transformers (power electronics devices) or ground fault interrupters. The highest permeabilities and lowest coercitivities are achieved with a content of nickel of 75-80%, where with the addition of elements like copper or chrome, it is possible to increase the resistivity of a factor 3 or 4, have a coercive field lower than 1 A/m and initial relative permeabilities higher than 100000. These kinds of alloys are known as supermalloys and their use is adopted for magnetic shielding applications. As a drawback, these alloys are all susceptible to heat treatments and the degree of cold working. Moreover, a heat treatment at very high temperatures (1100 $^\circ$ C) is always recommended after shaping.

2.1.3 Weakly magnetic materials

Weakly magnetic materials are materials with relative magnetic permeability in the range $\mu_r = 1.00001$ to 6. In science and industry, several technological issues arise where structural materials and components with vanishing (ideally zero) magnetic behavior are required. In practical alloys, such as austenitic steels, brass and bronze, traces of magnetism are present as a rule [53]. Non- magnetic materials are an issue for the design of particle accelerator equipment. Among metals, aluminum is undoubtedly the standard used, although its strength and elastic modulus are often too low for specific applications. Titanium has a better behavior in this sense, but it is used mainly in special vacuum chambers, because of its reduced availability and high costs. Ceramics are even better in many aspects, but even more expensive and brittle than the other materials listed above. Considering their high mechanical strength, stainless steels are the ideal choice as structural elements of particle accelerator components, but attention has to be paid to quality control of the vanishing magnetic properties.

Structural materials for fusion magnets

Austenitic stainless steels are widely used in hostile environments, such as nuclear reactors, naval vessels, and chemical plants, where the combination of good corrosion resistance with high strength, stiffness, and toughness is required. However, the metastable austenitic (γ) phase is easily transformed into ϵ or/and α' martensitic phase, owing to the deformation during manufacturing or fatigue during service. With an increase of martensitic transformation, the strength of the material increases, while ductility and corrosion resistance decreases.
Industrial specifications typically call for an upper limit of the magnetic susceptibility of these materials, ranging from a few units to some 10^{-3}, and practical methods to characterize faint susceptibility material are therefore needed. As an example, in the framework of quench detection in ITER Toroidal coils (TF), considering the strong field predicted, co-wound stainless steel tapes with a relative permeability lower than two must be used. Nevertheless, during production, these steel tapes are subjected to different levels of mechanical and thermal stresses [143]. In practice, after the manufacturing process, the magnetic and paramagnetic material properties are changed. Consequently, the measurement of the actual magnetic properties of the material is needed.

Stainless steel for collars of superconducting magnets

Superconducting magnets' coils are subjected to a strong force proportional to the flux density generated by the magnet itself. Generally, the coils are held in place by using stain steel holders, called 'collars'. The material the collars are made of has to have a μ_r, lower than 1.003 to do not interfere with the flux density generated by the coil, as it can be seen in Fig. 1.2. Hence, magnetic testing of the actual delivered pieces is critical.
For the collars of the new LHC superconducting magnets, the structural material chosen is an austenitic steel P506 produced by Voestalpine supplier. P506 is a

stainless steel specially developed by CERN belonging to the family of high Mn, high N stainless steels [126]. This special composition (approx. 0.012%C, 19%Cr, 11%Ni, 12%Mn, 0.9%Mo, 0.3%N) allows low relative magnetic permeability to be maintained down to cryogenic temperatures.

Tungsten-based alloys for coils' radiation protection

In the upcoming LHC upgrade at CERN, higher luminosity will boost the radiation dose received by the accelerator magnet's coil and consequently decrease its lifespan, as assessed in Chapter 2. Hence, a radiation shield with relative permeability less than 1.005 is required for some of the magnets closest to the detectors. The selected commercial material, INERMET® IT180 [110] contains 5% of nickel and copper in unspecified proportions and it is marketed as non-magnetic. However, according to the available literature, its magnetic properties depend critically on the precise composition. Even if slightly paramagnetic, an eventual residual magnetization of this material could interfere with the magnetic field generated by the magnets and decrease the whole accelerator performance. Tungsten composites are metal-metal composites produced by liquid phase sintering of mixed tungsten (90-97 %), nickel, iron, copper, molybdenum and cobalt powders. After proper sintering, the material consists of spherical tungsten particles embedded into a solid solution Ni-Fe-W(Co), Ni-Fe-W(Mo) or Ni-Cu-W matrix. These composites exhibit a unique combination of high density (17-18.6 g/cm3), high strength (700-900 MPa), excellent corrosion resistance, dumping capability, good thermal and electric conductivity and relatively high ductility, which allow them to withstand moderate amounts of cold working. Their properties make them attractive for many applications: balance weights, welding electrodes, extruding dies, anti-vibration holders for tools penetrators. The ductility and strength of tungsten composites strongly depend on their microstructure, which in turn is controlled by thermal treatment and trace impurity content.
Tungsten composites are increasingly used worldwide as radiation shields. They successfully replace lead, formerly used for this application. The advantage of tungsten composites over lead is the combination of radiographic density, machinability, good corrosion resistance, high radiation absorption, high strength, high melting temperature and, what is always emphasized, lack of toxicity [10]. Protection of the normal conducting magnets MQW and MBW in the LHC will be done by specially manufactured, non-magnetic Tungsten Heavy Alloy (WHA) pieces. These pieces shall comply with ASTM B-777 class 3 with the iron content, which has to be below 30 ppm. This yields the following material composition: density $>$ 18g/cm3; yield strength $>$ 600 MPa; tensile strength $>$ 650 MPa; elongation at breakage $>$ 1%.

2.2 Characterization of magnetic materials

The characterization of magnetic materials is of paramount importance not only during the electromagnetic design of magnets but also during the magnet's production for guaranteeing good quality control, especially for large-scale productions. In electromagnetic design, the knowledge of how a certain material replies to a certain applied field (normal magnetization curve) is essential. it depends on several factors, such as the quantum phenomenology at the atomic level and the composition of the lattice, that give rise to a resultant macroscopic effect of the response. The magnetic behavior of a material is also strongly influenced by the lattice content. In this thesis, it will be shown how the impurity content influences the property of pure iron or the percentage of nickel deeply influences the properties of an iron-nickel alloy, thus its destination of use.
On the other side, magnetic measurements of materials are, also, needed to ensure quality control during magnets' production. For example, magnets in particle accelerators are usually powered in series. What is essential for particle accelerator is that all the magnets behave the same. Hence, an excellent level of reproducibility of their magnetic behavior has to be guaranteed.
The magnetic characterization of materials can be directed both at the measurement of intrinsic properties, such as saturation magnetization, magnetic anisotropy and Curie temperature and at the determination of magnetic constitutive law, as embodied by the magnetization curves and the related hysteresis phenomena [52]. In this thesis, we will concentrate on the latter point and the related measuring techniques. Several methods and standards have been developed for measuring materials' magnetic properties. These methods depend on many different parameters, such as:

- Waveform and frequency of the excitation current: sinusoidal excitation (AC) at low, medium and high frequency or quasi-static excitation (DC) as described in the IEC 60404 series [38, 39, 70].
- Expected relative magnetic permeability of the material under test ($\mu_r \approx 1$, $\mu_r = 10^3$ - 10^4, $\mu_r > 10^5$).
- Sample shape (rings, laminations, needles, cylinders) and size.
- Portability of the instrumentation.
- Anisotropy of the material.
- Temperature at which the measurement is performed (cryogenic, room temperature, high temperatures).

A classification based on the specific physical effect exploited in revealing the magnetic state of the material is found in [53]: (i) Force techniques; (ii) Flux-metric techniques; (iii) Magneto-metric techniques; (iv) Magneto-optical techniques; (v) Magneto-strictive techniques; (vi) Magnetic resonance methods. This thesis's research will focus on the flux-metric and magneto-metric measuring methods. In

the former, a coil linked with the test sample is the location of an electromotive force following a change in the material magnetization engendered by the application of a magnetic field. The magnetization is determined by integrating the induced voltage. In the latter, the field lines emitted by an open sample are intercepted and related to the magnetization of the material. In the following three paragraphs an overview of the methods to characterize the three categories of magnetic materials previously distinguished (weakly magnetic materials, soft magnetic materials, and materials for magnetic shielding) is given.

2.2.1 Characterization of materials for magnet yokes

The characterization of soft magnetic materials is a very vast subject. The most recent book covering this field was written by Tumanski [136]. Collecting state-of-the-art knowledge from information scattered throughout the literature, Handbook of Magnetic Measurements describes magnetic materials and sensors, the testing of magnetic materials, and applications of magnetic measurements. In the text by Fiorillo [52] a review of the most important methods is presented as well. Several methods to characterize soft magnetic materials at several frequencies are presented, as well. These methods are essential in applications, such as transformers, generators, motors and for electric power generation, where the core loss in Watt/kg is the most critical parameter. On the contrary, in particle accelerator magnets, soft magnetic materials are mainly used as electromagnet yokes, where magnetic fields are fixed or slowly varying and core loss is no longer the important parameter. The rate of change of the induction in the gap of a particle accelerator magnet is in the order of 10 T/s. Therefore, quasi-static measurements (DC) provide the best estimate of material magnetic properties. In this section, the three main commonly used techniques to measure soft magnetic materials with consideration to the application of particle accelerator magnet core, namely ring method, Epstein frame and single sheet tester, are introduced. A particular focus is given to the instruments, based on these three techniques, developed at CERN magnetic laboratory. All the three hereafter described methods and apparatus follow the same flux- metric and close-loop principle and are based on the measurement of a transient voltage induced on a secondary winding by a step-like field variation applied on a primary winding.

Epstein frame

The Epstein frame is one of the most used standards for measuring the global magnetic properties of electrical steels. The IEC standard 60404-2 'Epstein frame' applies to non-oriented and grain-oriented sheets and strips for DC and AC measurements at frequencies up to 400 Hz [71]. The Epstein frame is a sort of unloaded transformer. It consists of a non-magnetic square form, where four sets of primary and secondary windings are wound. The sample consists of steel strips placed inside the non-magnetic square form in a way that a closed magnetic path is formed. The main advantages of this method are the wide ranges of magnetization frequencies (0-100 kHz) and magnetic field intensities (0.2 A/m - 10 kA/m);

the good accuracy of the results and the easy machining of the samples. The main drawbacks are the inhomogeneity of the magnetic circuit due to the overlapping corners and the definition of a mean path length, even though it varies with the peak flux density, excitation frequency, permeability and anisotropy of the material under test.
At CERN the Epstein frame has a somewhat limited application, while in the industry it is a standard for AC measurements (50 Hz losses). On the other side, it overcomes the ring method's problem of measuring anisotropy of magnetic materials. An adapted-to-CERN-needs version of the Epstein frame has been developed to measure thinner steel laminations than the standard Epstein frame. This makes the production of the sample quite easy, requiring just a simple cutting of the lamination. An Epstein frame can be used as a permeameter at the exception of the saturation where it is less and less precise due to the increasing flux leaks at the corners [24].

Single sheet tester

The single sheet tester is another standard method to measure the magnetic properties of electric sheets, as reported in the standard IEC 60404- Part 3: Methods of measurement of the magnetic properties of electrical steel strip and sheet utilizing a single sheet tester [37]. It is mainly designed for fast measures of the coercitivity H_c of the material under test. In [62] a compensated Single Sheet tester was developed to measure very soft materials with high precision. The main advantages of SST are that the excitation field can be limited to 1200 A/m. Considering that H_c is maximum at 1.5 T, it is possible to measure anisotropy. Generally, there is no sample preparation and measurements are very fast (a few minutes). The main disadvantages are the difficulty to guarantee a good contact between the sample and the yokes to minimize a parasitic air gap; the relative magnetic permeability in the yoke material must be considerably higher than in the sample, this limits the use of this method to the measure of iron-based alloy; accurate positioning is needed to avoid displacement of the yokes with respect to each other. In accelerators, a crucial parameter is the reproducibility between magnets of the same kind. Considering that magnets are powered in series, the main sources of differences between them are the mechanical accuracy and the magnetic properties of the yokes. In order to guarantee a good level of yoke to yoke reproducibility, a good quality control, of the coercitivity and the relative permeability of the material used for the production, is essential. Considering the good correlation exciting between these two parameters, a whole production can be sufficiently well controlled by an SST, saving costs and time. The Ring method can be used as a reference.
This is the reason why at CERN a customized version of the single-sheet tester, called coercimeter [25], has been designed and used for decades to characterize tons of steel laminations for magnet yokes of several large-scale projects, such as the Large Electron-Positron (LEP) collider (11000 tons) and the LHC (50000 tons). In particular, the coercimeter was designed to measure steel sheets without preparation and just before being punched. It uses a Mumetal yoke material

in order to guarantee a good flux return with minimum coercitivity. Nowadays, the main hardware components are still available. However, the interface and control software and several electronic components are obsolete.

Ring method

A series of standards, denoted by IEC 60404, groups basic magnetic measurements in electrical steels. In particular, in the standard IEC 60404- Part 4: Methods of measurement of d.c. magnetic properties of iron and steel [72] the ring method is presented. A detailed discussion of this method will be given in chapter 3. Here the main advantages and drawbacks are highlighted. Any air gap, ends or discontinuity in a magnetic circuit create a demagnetizing field, which opposes the applied field and reduces the induction level in the material under test. The main advantage of ring samples is that they are free from demagnetizing fields. On the contrary, the excitation field inside the sample is not constant and varies with the inverse of the radius. A ring sample is not too difficult to machine even if attention has to be paid to avoid heating or surface cold working during machining. A drawback is that with a ring method is not possible to take into account any anisotropy in the material, because, unlike the single sheet tester, it only gives an averaged value. With a ring method, the coercimeter value can be easily underestimated. If a sample is made of several laminations, with a relatively large anisotropy, stacked on each other, a sort of magnetic short-circuit could occur and generate a significant error on the coercitivity measure. The main disadvantage of this method is having to install new windings for each new sample, which can be quite a long and tedious work.
At CERN, this problem has been overcome by designing and developing the 'split-coil' permeameter [65], where the coils have been split into two halves. Good quality interconnections have been used considering the number of connection (two per turn all in series). The main advantage of this solution is the significant reduction of the measurement duration, allowing the use of this device for the quality control of large productions. On the other hand, a drawback is that the heat dissipation limits the maximum excitation field to 24000 A/m for some seconds, preventing the study of the saturation region.

Magnetic properties of materials at high fields

In this thesis, a distinction between the characterization at standard fields and high fields is made. Where standard fields mean a magnetic field lower than about 24000 A/m (approximately the magnetic field needed to bring the material in saturation).
Characterization at this field values is particularly required for normal-conducting magnets. Even though the characterization at standard fields allows to obtain the value of saturation magnetization, characterizing a ferromagnetic material at higher fields is essential for superconducting magnets: Typically the initial magnetization curves are delivered up to a field value of roughly 48 kA/m. Data for higher field values are extrapolated using empirical models and fitting algorithms. Characterization of magnetic materials at high fields allows these models

to be improved or validated.
A similar problem of characterizing the magnetic properties of a material for such a wide range of fields was described in [78] for the 10 T single and twin aperture dipoles developed at the National Laboratory for High Energy Physics in Japan (KEK) in collaboration with CERN. Moreover, a similar characterization was done for the iron yoke of the LHC magnets, reaching a magnetic field up to 2.5 T [20, 23].

2.2.2 Characterization of materials for magnetic shields

The methods presented in the previous section are also employed for characterizing magnetic shielding materials such as MuMetal and CRIOPHY, but the measurements are typically performed at very low fields. This because a magnetic field H of 10 A/m is already enough to bring these materials in saturation. In this section, the focus is given to characterizations and magnetic shielding applications of such materials, rather than on the method itself used.
Several interesting research works on magnetic shield have been presented in literature [135]– [94]– [56]– [6]. In [135], magnetic properties and shielding characteristics of multilayered Ni80Fe20/Cu film shields were investigated as a function of thickness and number of layers. Moreover, the main shielding mechanisms for multilayered Ni80Fe20/Cu film samples under different external influences were discussed. In [94], an experimental research on the magnetostatic shielding effectiveness of a single-layer cylindrical sample of the shields based on electrolytically deposited Ni80Fe20 alloy was carried out. It has been shown that in the magnetic fields range from 100 A/m up to 2700 A/m, the shields based on the Ni80Fe20 alloy are preferred over ones based on the 84KHSR amorphous ribbon.
Several further works specifically focused on the characterization of magnetic shield materials, have been presented [43]–[97]. In [43], first the effect of the magnetic field on the gain and charge collection of some large-aperture photomultiplier tubes were investigated. Then, the photomultiplier magnetic shield, made of the material FINEMET, was described. In the presence of the Earth's magnetic field, this type of shielding was proved capable of significantly increasing the collection efficiency of photoelectrons, as well as improving the response uniformity of these tubes.
In [120], the magnetic properties of two important passive magnetic shielding materials (A4K and AMuMetal) for accelerator applications, subject to various processing and heat treatment conditions, were studied over a wide temperature range. The effect of processing on the degradation of the magnetic properties of both materials was also investigated. The authors state that while some prior work exists on characterizing the magnetic properties of such materials, a comprehensive study of the effect of deformation during the manufacturing process and annealing on the magnetic permeability of shielding materials over a broad range of temperatures (from cryogenic to room temperature) is still not available in the literature. Their paper bridges this gap by performing such experimental studies, yet only for A4K and AMuMetal samples.

In [98], the magnetic properties of Cryophy, the material of interest for CERN crab cavity cryomodules [133], were measured at room and cryogenic temperatures. Furthermore, the permeability dependence on the maximum annealing temperature (1100 ° and 1170 ° C) was examined on ring samples. From these data, Cryophy was chosen as the magnetic shielding material for the superconducting cavities in the main linac section of the compact Energy Recovery Linac (cERL) at the High Energy Accelerator Research Organization (KEK), in Japan. The effect of mechanical deformation on the magnetic permeability of magnetic shields is investigated in [97], where a significant degradation of the magnetic permeability with mechanical strain was observed on high Ni-content alloys. However, their exact composition was not disclosed. Furthermore, although the magnetic properties are measured at room and cryogenic temperatures, the permeability dependence on the heat treatment conditions is studied in view of a specific application target for ERL.
Analyzing the results and conclusions in these papers, it is evident that:

[1] the requirements of the magnetic shield on the Cryophy magnetic permeability is challenging and requires experimental studies on samples of the same material used for the cryomodule;

[2] few magnetic characterizations of high Ni-content alloys are presented in literature, including Cryophy;

[3] a comprehensive magnetic characterization of this alloy, focused both on temperature and mechanical strain dependence, is not yet present in literature;

[4] moreover, as stressed in an inter-laboratory study on the precision and accuracy of determining the soft magnetic properties of high-permeability materials utilizing direct current (DC) methods, the repeatability and reproducibility of the results are low [129].

2.2.3 Characterization of weakly magnetic materials

In this section, an overview of the main methods to measure the relative permeability of weakly magnetic materials is presented. A special focus is given to the methods developed at CERN magnetic laboratory.
The ASTM international standard A342/A342M-2014 [18] describes four procedures for the determination of relative permeability of materials having a permeability below 6.0: Test method I - Fluxmetric method; Test method 3 - Low mu permeability indicator; Test method 4 - Flux distortion and Test method 5 - Vibrating sample magnetometry.
In the previous editions of the standard a test method number 2, called "Permeability of paramagnetic materials", was also included. However, in the last edition, it was eliminated as an acceptable method of testing. Nevertheless, in recent literature, a relevant number of authors still refer to this method, and so it has also been included in this overview.

Fluxmetric Method - Test method I

This method allows permeability between 1.0 and 4.0 to be measured. Usually, it is used for design purpose, specification acceptance, manufacturing control and R&D.
The classic layout of the method is illustrated in Fig. 2.1. The main components are a source of DC current; a magnetizing solenoid with a pair of test coils, one for measuring magnetic flux density and the other for compensating the air flux; and a fluxmeter for measuring the magnetic induction. The test specimens can have the shape of a bar, rod, wire, or strip with a uniform cross-section.

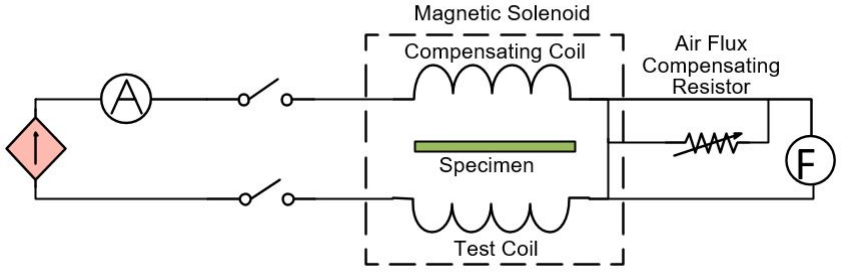

FIGURE 2.1: Example of fluxmetric measurement system layout. Adapted from [18]

It allows the selection of the magnetic field at which the permeability is measured by adjusting of the DC power supply. The use of compensating coils causes an increase of the method's accuracy. However, because of the specimen shape, a demagnetization field will be generated. This leads to an overestimation of the magnetic field strength and a reduction of the flux leakages in the B-coil.

Permeability of paramagnetic materials - Test method II

Even if excluded from the ASTM standard, an alternative to the flux metric approach is represented by a group of methods called "Force methods". These methods have high accuracy when dealing with permeability close to unit. The most common are the Faraday balance and the Gouy technique [114], [144]. These methods are suitable for measurement of materials with $\mu < 1.05$.
A general layout of the measurement system is depicted in Fig. 2.2.

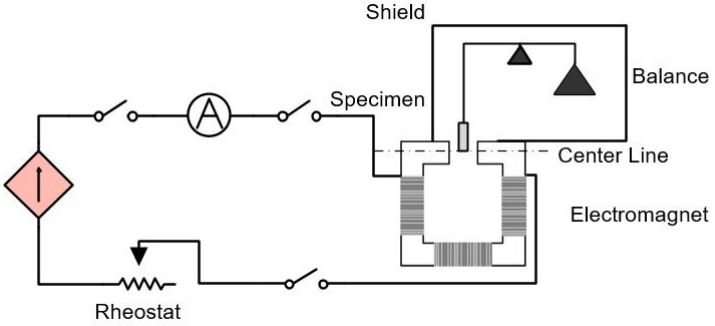

FIGURE 2.2: Classic layout of a force method measurement system. Adapted from [18].

After demagnetizing the sample and calculating its cross-sectional area, the specimen is suspended from the balance. A magnetizing current is turned on and set to such a value as to give a magnetic field strength of 80 kA/m, minimum. The permeability is calculated from the apparent change in mass of the specimen.
Force methods can display better sensitivity than flux metric methods, but they are rather cumbersome and time-consuming. Because of restrictions on the specimen shape (typically very small), these test methods are most often used to evaluate semifinished products before are manufactured.
At CERN, a built-in magnetic balance has been used for decades to measure weakly magnetic materials before and during the production of several components later installed in the LHC and several other CERN experiments [125]. Nowadays, the main hardware components are still available. However, the interface and control software and several electronic components are obsolete.

Low-μ permeability indicator - Test method III

The low-μ permeability indicator is based on comparing the permeability of a tested specimen with a standard insert, with known permeability [57]. Hence, it provides test values suitable for specification purpose, generally stated as "permeability is less than". Usually, these instruments are portable, commercially available and present the advantage of being able to test specimens of all forms and shapes, providing that there is a suitable flat surface [88]. A drawback of these instruments is that usually the measurements are made in a magnetic field strength of only 8 kA/m, where a magnetic field of roughly 80 kA/m is generally recommended.

Flux Distortion - Test method IV

Instruments based on other methods, for example, flux distortion, such as the Foerster Magnetoscop [73], are also commercially available. The method, schematically shown in Fig. 2.3, is suitable for materials with relative permeability between 1.0 and 2.0.
The permeability measuring method is based on the fact, that every permanent magnet possesses a defined distribution of lines of force. All lines of force of a cylindrical permanent magnet run in a plane through the center of the cylinder between the two poles that are parallel to the cylinder axis. A gradient probe is placed on either side of the cylindrical magnet in this plane perpendicular to the cylinder axis at the center of the permanent magnet. The lines of force of the magnet are perpendicular to the axis of the two probes. Therefore, they do not measure the magnetic field of the cylindrical magnet. If the cylindrical magnet is placed on a material whose permeability is greater than 1, there is a minute displacement of the magnetic zero of the cylindrical magnet towards the material on which the magnet has been placed. In the lower permeability ranges, this displacement is a measure of the permeability of the material.

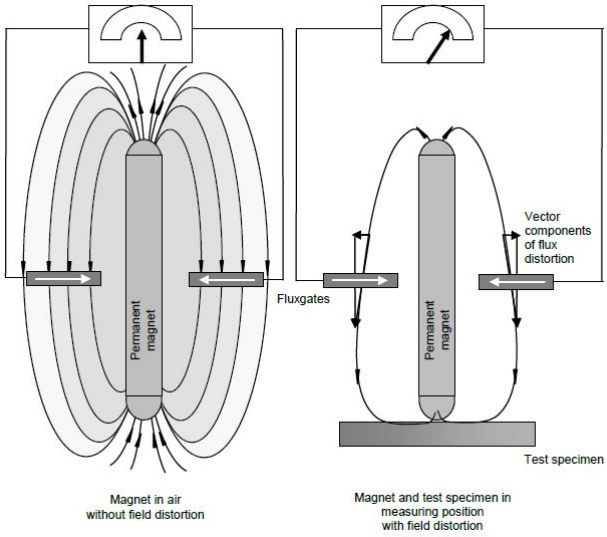

FIGURE 2.3: Schematic of the flux distortion meter arrangement and magnetic field distribution without (a) and with (b) test specimen. Adapted from [73]

In this method, a small volume of the specimen is subjected to a local magnetic field that varies in magnitude and direction, so it is not possible to specify the magnetic field strength at which the measurement is made. The field strength at the permeability probe tip is approximately 75 kA/m.
Materials to be measured with permeability probes should be thicker than approximately 8 mm whenever possible. Accurate measurements of materials that are thinner than 8 mm may be possible by stacking two pieces, but the air gap between the two pieces must be as small as possible.
The flat area on which the permeability probe is placed must not be less than approximately 20 mm in diameter. When testing on curved surfaces the radius of curvature must not be less than approximately 40 mm. If any of the required dimensions are less than those specified, the instrument will indicate permeability below the actual value [73].
At CERN, this instrument represents the standard to measure weakly magnetic materials at room temperatures.

Vibrating sample magnetometry - Test method V

In the literature, the most common method to characterize weak magnetic materials is the vibrating sample magnetometer (VSM) [54], [89], [102]. A classical VSM arrangement is presented in Fig. 2.4.

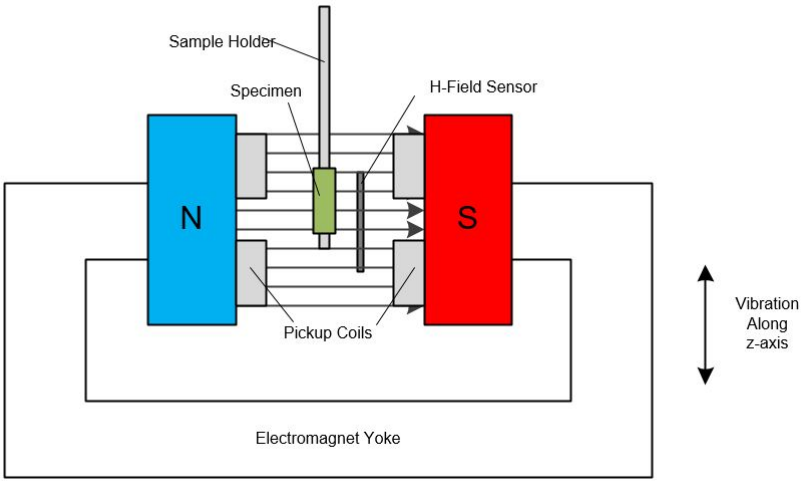

FIGURE 2.4: Schematic of a classical VSM arrangement. Adapted from [18].

The principle involved is the oscillation of a sample in a steady field, thereby inducing an alternating voltage in a pickup coil. This voltage is then amplified and measured by a voltmeter. For a routine laboratory magnetometer, the simplest geometry is to have the direction of the sample vibration parallel to the axes of the pickup coil and applied magnetic field [89].
Although VSM techniques are the most sensitive, their use is limited to specialized laboratories and they are not practical from an industrial point of view, such as for a series production, due to high costs and tight constraints on the specimen shape and volume. In [112], for instance, the thickness of the samples was 200-300 nm, and the lateral dimension 5 x 5 mm^2.

Inverse problem formulation

In recent years several works have focused their attention on inverse algorithms for the identification of the magnetic material characteristics [2], [49], [59], and [92].
In [2], the use of the electromagnetic inverse problem for the identification of magnetic material characteristic is reviewed. The inverse algorithm is combined with a generic stochastic uncertainty analysis for error estimation and reduction. The methodology is applied to characterize a commercial asynchronous machine magnetically. The case study shows good agreement between numerical and experimental results, validating the proposed inverse approach.
In [49], a new approach for the characterization of magnetic materials involved in electrothermal processes is presented. In this case, the inverse analysis techniques are coupled with an induction heating finite-element model. In particular, the magnetic permeability is identified as a function of temperature and internal magnetic field strength.
In [59], the authors present an approach based on the use of finite element analysis combined with a supervised feed-forward neural network. The idea is to use the finite element method to simulate a large number of parameters in a material

under test, then use this data for the training of the neural network. Finally, new materials are evaluated by the neural network obtained. The results presented in this paper prove the efficiency of the proposed approach, and encourage future works on this subject.

2.3 Measurement of magnetic axis displacements

2.3.1 Axially-symmetric magnets

In the last decades, resistive and superconductive axially-symmetric magnets have been investigated and employed at an increasing rate in several and heterogeneous research fields [121]. As an example, in particle accelerators, magnetic elements such as solenoids are applied in low-energy beam transport sections [15], and in modern radio-frequency (RF) linear accelerators (linacs), for emittance compensation, transverse focusing, and electron cooling. Examples of resistive solenoids employed as focusing lenses in RF linacs are Linac3 [36] and Linac4 [9] at CERN. Superconductive focusing solenoids are also adopted for the project High Intense Neutrino Source (HINS) at Fermilab and the High Intensity and Energy (HIE) upgrade of the ISOLDE facility at CERN [77]. The advantage of using short solenoidal lenses in high-power accelerators, instead of sequential pairs of quadrupoles, is the reduction of the emittance growth and the related particle losses [105]. However, the application of axially-symmetric magnets goes beyond the particle accelerator research. For instance, a low-field, large-bore High Temperature Superconductive solenoid for emittance compensation was designed for the superconducting radiofrequency electron gun for the WiFEL at the University of Wisconsin [26]. Magnets of this type have also been employed in many different devices, such as electron microscopes [140], particle therapy, and short-pulse radiographic diagnostics [68].
An axially-symmetric magnet is based on one or a series of axially-centered coils, producing a region of cylindrically-symmetric, radial, and axial magnetic fields. The solenoid field consists of two components: a dominant, axial component, with a maximum strength at the center of the solenoid, and a weak, radial component with relevant effects only towards the ends of the solenoid. Charged particles moving outside the magnetic axis are azimuthally accelerated by the radial field component, especially in the magnet's end regions. This leads to the helical motion of the charged particles in the longitudinal field region of the magnet. Therefore, particle beams require a strict determination of the magnetic axis.
In specific accelerator designs, a multi-coils solenoid could be preferred to a series of solenoids, or one bigger solenoid, as focusing element for particle beams or transport, for several reasons. Multi-coil solenoids with coaxial coils were studied for producing a uniform magnetic field [21, 107], or particular field configurations, e.g., a near-linear gradient axial magnetic field [111]. Furthermore, the use of multi-coil solenoids as focusing structures is of great interest, too. An example is the 8-GeV proton driver linear accelerator, proposed at Fermi National Accelerator Laboratory (FNAL), where superconducting solenoids have been employed

in the front-end focusing system of the High Intensity Neutrino Source (HINS) [106, 8]. In all these cases, the alignment of the coils axes is essential for the system performance or even functionality.

2.3.2 Measurement methods

Axially-symmetric magnets are hardly compatible with the standard instrumentation optimized for accelerator multi-pole magnets and are routinely tested with expensive and time-consuming mapping systems [108]. Recently, several methods have been developed to measure the magnetic field of axially-symmetric magnets and overcome the use of mappers. For instance, a novel method exploiting the inherent axial symmetry of the magnetic field was proposed. The method in [15, 12] is based on an induction transducer, sensitive to the longitudinal and radial components of the solenoid under test, moving along the magnet axis. The voltage induced in the transducer is then acquired and integrated digitally in order to yield the flux linkage as a function of the linear position, measured by a laser interferometer.
In the literature, the methods to align solenoids can be grouped in three main categories: (i) the single stretched-wire methods [44, 45], (ii) the vibrating-wire methods [14, 11, 138] and (iii) the Hall transducer-based methods [80, 109].
The single-stretched-wire method exploits the Faraday induction law: when a single conducting wire is moved inside a magnetic field, the integrated voltage across its connection terminals is a measurement of the magnetic flux linked with the surface traced out by the wire. The axis is obtained by iterating horizontal and vertical sweeps of the wire until symmetric start and end points, where the flux is null, are found. This is a standard method for finding quadrupole magnets' magnetic axes; however, in the case of solenoids, this method has a much lower sensitivity, because the intercepted transversal field components are significant only at the magnet's ends.
The vibrating-wire method, instead, is based on the Lorentz force. When a current pulse is driven through the wire, its interaction with the magnetic field generates mechanical vibrations, which can be measured and put in relation with the surrounding field. This method is a standard to measure magnetic axis position in quadrupole magnets for particle accelerators. The basic idea is to find the wire position in the magnet aperture where the smallest oscillations at first and second resonance frequencies are observed [11].
This same principle was applied to solenoids [14]. When the wire position coincides with the magnetic axis, the transversal field components cancel out and no motion is induced on the wire. Two wire resonance frequencies are excited for co-and counter-directional movements of the wire stages in the process of centering and aligning a solenoid. This procedure of finding the minimum oscillation amplitudes has a sensitivity to the misalignment in the order of the micrometer. The main drawback of this method is that the procedure is applicable only if the whole solenoid's aperture is accessible. Hence, these methods cannot be applied to real-time monitoring of an operational solenoid.

A different approach for estimating the magnetic axis consists of using Hall transducers. For example, the field generated by the rotation of a Hall transducer at several points along the axis of a solenoid can be recorded as a function of the rotation angle [80]. Then, the displacement of the axis of rotation from the magnetic axis is retrieved post-processing the solenoid field. A common way to determine the magnetic axis using Hall transducers to calculate the magnetic center is by measuring the 2D field profile of the solenoid at different positions along the z-axis and then estimating the magnetic axis position with a resolution of 0.01 mm [109]. In this case, the axial component of the magnetic field is measured, rather than the radial component. The drawback of the Hall transducer-based methods is the mapping of the full solenoid aperture, generally performed with moving stages through sturdy mechanics.
When a magnet is in operation, its coil is continuously subjected to an electrodynamic strain. This could quickly bring to a significant misalignment of the magnetic axis from the geometric axis. In the case of a multi-coil solenoid, this effect would be even more dramatic, because the different coils could show different misalignments. Hence, a system for monitoring in real time these misalignments is essential in all applications where a strict constraint on the coils alignment is required, giving the possibility to adjust each coil position to achieve/recover the solenoid design parameters. However, the standard methods to find the magnetic axis, introduced in this section, are not suitable for real-time monitoring, because they require that the whole solenoid's aperture be accessible.

2.4 Objectives of this thesis

This thesis describes the study, design and experimental activities related to the development of new methods for measuring magnetic materials and magnet axis displacements. These developments involve the following main achievements:

- **Revamp and upgrade of the split-coil and cryogenic permeameter.** A set of new analog to digital converter (ADC), digital to analog converter (DAC) and other components have been procured, characterized and integrated into the measurement system. New control and post-processing software have been developed in the established C++ framework of the CERN magnetic laboratories, FFMM [16]. An extensive suite of tests has been performed in order to validate both the control and the post-processing software components. An adapted-to-low-permeability-materials approach based on a time-saving, flux-metric method has been proposed for the characterization of weakly magnetic materials.

- **Design and implementation of a superconducting permeameter**. The measurement system is based on employing a ring sample at cryogenic temperatures and a superconducting excitation coil. Quench protection solutions have been studied and implemented as well. The problem has arisen from the necessity to retrieve the normal magnetization curve of ARMCO® Pure Iron, the material employed as the iron yoke for the new HL-LHC magnets [115, 132].

- **Design and validation of a novel method for characterizing weakly magnetic materials**. The method is based on an inverse analysis approach coupled with a finite-element model. A material with unknown permeability is inserted into the air gap of a dipole magnet and the consequent perturbations of the dipole background flux density are measured and acquired in FFMM utilizing a Metrolab NMR sensor. A positioning stage, controlled by an FFMM application, allows the sensor to move around the sample and to keep track of these positions. The relative magnetic permeability is then identified through grey-box inverse modelling, based on a finite-element approach.
- **Design and validation of a new method for solenoid magnetic axis alignment**. A method for monitoring the coils alignment in multi-coil solenoids, directly during their operation in particle accelerators has been proposed. Few measures of the magnetic field by Hall transducers and a local field model allows monitoring the magnetic axis position of each coil, and thus, to keep a particle beam strongly focused over its operation time. The method was validated on a challenging case study on the European project "ELI Nuclear Physics" (ELI-NP).

By employing these measurement systems, several materials have been characterized at their operational temperature and magnetic field. In particular, the magnetic properties of series production co-wound stainless steel tapes for quench detection in ITER TF coils have been measured by employing the proposed adapted-to-low-permeability-materials approach based on a flux-metric method. The magnetic properties of the ARMCO® Pure Iron, for the construction of the superconducting magnet yokes in the framework of the HL-LHC upgrade, have been measured, within annealing treatment sequences from 750 °C to 850 °C, at operating temperatures of 4 K to 300 K. The dependency on the operation temperature was shown by testing the material at the cryogenic temperature of roughly 4 K, 77 K and room temperature. Finally, tests performed before and after the application of mechanical stress have also been studied to validate the production process.
Another goal of this thesis has been to reduce the lack of data present in the literature and to validate the use of Cryophy as the cold magnetic shield material of the crab cavities cryomodule prototype. Accurate experimental studies on samples from the same heat treatment as the parts of the actual shields at CERN have been performed.

In Fig.2.5 a classification of the developed measurement systems is presented. The classification is based on: (i) maximum magnetic field, (ii) expected relative magnetic permeability and (iii) operational temperature.
The characterization of materials for magnet yokes and magnetic shielding (relative permeability in the range 10^3-10^6 is performed utilizing a split-coil permeameter and an Epstein frame at room temperature and a cryogenic permeameter at cryogenic temperatures, respectively. Measurement systems, based on the flux-metric method, are explained in detail in chapter 3. In particular, the Epstein frame is used to perform the characterization in AC, at a frequency up to 400

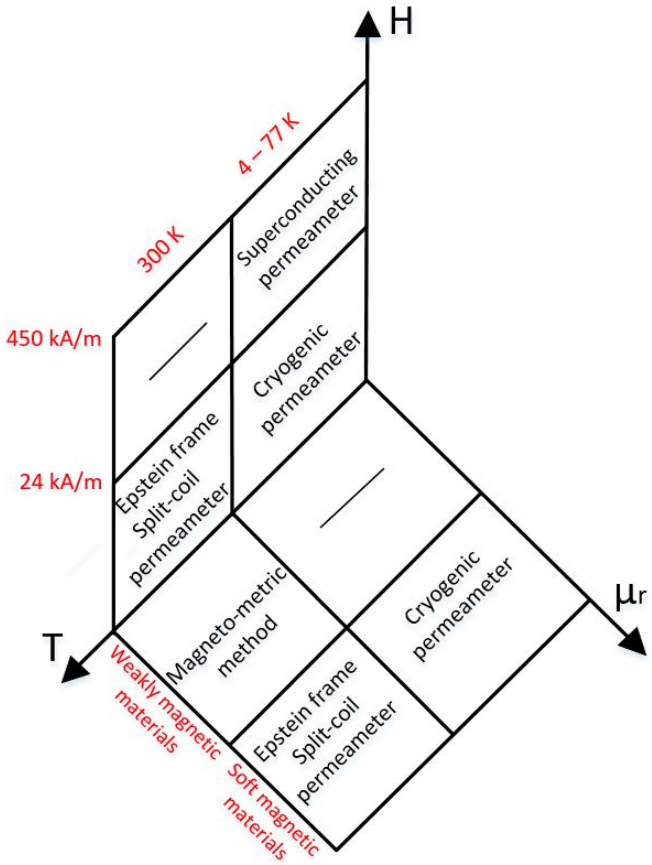

FIGURE 2.5: Classification of the main measurement systems developed during this activity and employed at CERN for characterizing magnetic materials.

Hz and the split-coil and cryogenic permeameters are used to perform measurements in quasi-static conditions. Hardware limits make it impossible to exceed an excitation magnetic field of 24 kA/m.
This limit has been exceeded by designing and employing a superconducting permeameter. Its design, implementation and quench simulations will be described in Chapter 3. It allows measurements to be performed up to 450 kA/m in a region of the normal magnetization curve where the material is heavily saturated. The results of the characterization of ARMCO for HL-LHC at this level of saturation are presented in chapter 6.
Concerning weakly magnetic materials, an adapted-to-low-permeability-materials of the flux-metric method is used in a range of permeability among 1.1 and 6.0, whereas the results in therm of uncertainty are not satisfying when μ_r goes below 1.1. Hence, for weakly magnetic materials with a relative magnetic permeability μ_r less than 1.05, a measurement system based on a novel magneto-metric method has been developed and validated. These two measurement systems are explained in detail in chapter 4.

Chapter 3

Proposal for characterizing soft magnetic materials

In this chapter, the measuring principle of the flux-metric method and the enhancements carried out in this work, concerning measurement procedure and drift correction are illustrated. Firstly, the design aspects of the experimental supporting technologies for data acquisition and analysis are described. Then, a solution for characterizing soft magnetic materials at the operational temperature of 4.2 K and a saturation level near 3 T is proposed. The measurement system employs superconducting coils. Hence, specific quench detection and magnet protection simulations are carried out. An uncertainty model and a study of repeatability and reproducibility of the measurement procedure are presented as well.

3.1 The measurement principle

The experimental methods adopted in this dissertation for characterizing soft magnetic material are based on the flux-metric method described in the standard IEC 640404-4 "Magnetic materials - Part 4: Methods of measurement of d.c. magnetic properties of iron and steel." [70].
Fig.3.1 shows a schematic representation of a standard measurement system. A sensing coil and an excitation coil are wound around the sample. The excitation coil carries the excitation current to magnetize the sample under test. This current is supplied by a current generator which is controlled by the signal provided by a digital-to-analogical converter. The sensing coil detects the induced voltage, that after integration allows the flux to be calculated and, consequently, estimate the magnetic flux density.

The magnetic field $H(r,t)$ is evaluated from the current using

$$H(r,t) = \frac{N_e i(t)}{2\pi r} \tag{3.1}$$

where N_e is the number of turns in the excitation coil, $i(t)$ is the imposed current and r is the distance from the center of the toroid. H is represented as a scalar for symmetry reasons.
The magnetic field is variable within the cross-sectional area of the toroid. Since

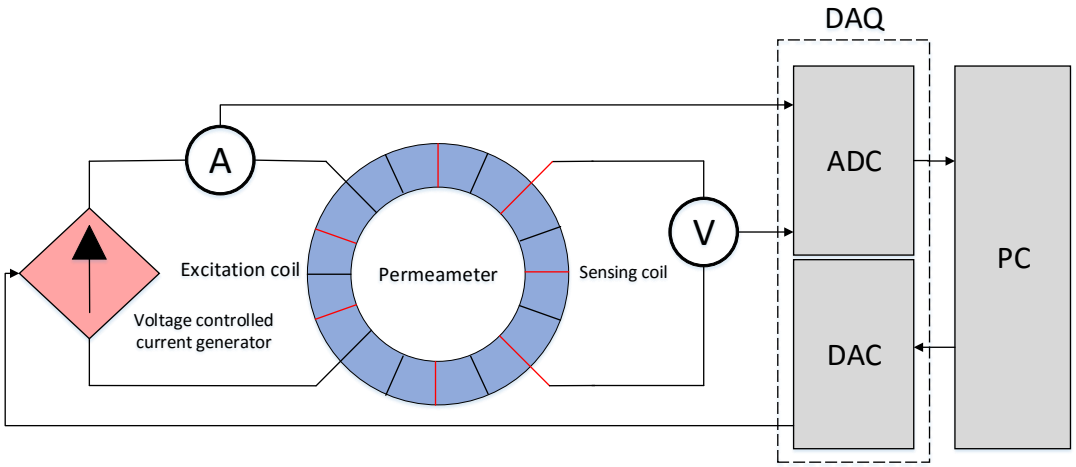

FIGURE 3.1: Architecture of the measurement system

the difference between external and internal diameter is much lower than the length of the circumference, the magnetic field is assumed constant in the cross-section and equal to its integral average between the inner and the outer radius, $H_0(t)$

$$H_0(t) = \frac{1}{r_2 - r_1} \int_{r_1}^{r_2} H(r,t)dr = N_e i(t) \frac{\ln \frac{r_2}{r_1}}{r_2 - r_1} = \frac{N_e i(t)}{2\pi r_0}. \tag{3.2}$$

After acquiring the induced voltage on the sensing coil, the magnetic flux is determined by integration

$$\Phi(t) = -\int_0^t v(\tau)d\tau. \tag{3.3}$$

The magnetic flux density $B(t)$ is

$$B(t) = \frac{1}{A_s}\left(\frac{\Phi(t)}{N_s} - \mu_0 H_0(t) A_a\right) \tag{3.4}$$

where A_s is the cross-sectional area of the sample, A_a is the cross-sectional area of the air, as represented in Fig. 3.2.

The magnetic relative permeability is

$$\mu_r(H) = \frac{B(H)}{\mu_0 H} \tag{3.5}$$

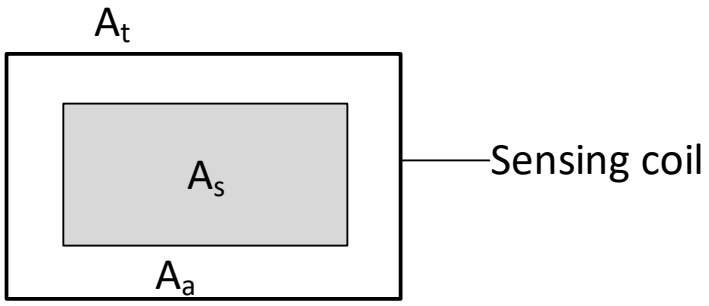

FIGURE 3.2: Representation of the cross-sectional area of the sample A_s and of the sensing coil A_a. The cross-sectional area of the air gap is $A_s = A_t - A_s$.

3.2 Procedure and drift correction

The procedure adopted for the tests, consists of three steps: i) demagnetization; ii) magnetization; and iii) post-processing.
Firstly, the sample needs to be demagnetized to remove memory-effects from the measurements. Demagnetization is performed by applying an excitation current with a decreasing exponential envelope. Magnetization is performed by ramping the current back and forth between positive and negative values, with the amplitude of each plateau slightly increasing. The ramp rates and the plateau durations are selected so that dynamical effects, predominantly eddy currents, are reduced after a certain percentage of the plateau. The current during this step follows the evolution represented in Fig. 3.3.
The waveforms acquired are post-processed by applying the relations from Section 3.1, but firstly, it is necessary to correct the voltage acquisition by means of a drift correction algorithm. The acquired voltage $v(t)$ can be expressed as the sum of three contributions

$$v(t) = v_s(t) + v_o(t) + v_n(t) \tag{3.6}$$

where $v_s(t)$ is the zero-mean induced voltage at the terminals of the sensing coil, $v_n(t)$ is a zero-average random noise and $v_o(t)$ is the offset error, a contribution that depends on various disturbance causes. By integrating $v(t)$

$$\Phi(t) = -\int_0^t [v_s(\tau) + v_o(\tau) + v_n(\tau)]d\tau \approx \Phi_s(t) + \Phi_o(t) \tag{3.7}$$

where $\Phi_s(t)$ is the magnetic flux and $\Phi_o(t)$ is the drift error. The contribution of the random noise is neglected because of the integration operation.
In the literature, several drift correction approaches have been proposed [55, 83, 128, 69]. The method proposed in this work can be split into the following steps:

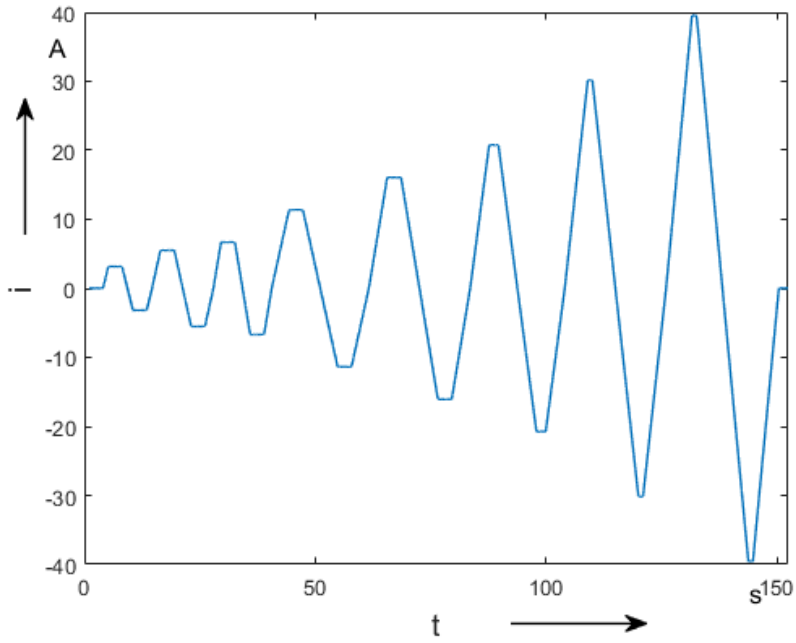

FIGURE 3.3: An example of a magnetizing current waveform

[1] Identify on each positive and negative plateau, the first and the last point, triangle and square symbols in Fig. 3.4.

[2] Estimate the point of the plateau corresponding to the end of the transient due to the ramp-up dynamic effects, circle symbol in Fig. 3.4.

[3] Evaluate for each plateau the offset of the sensing coil signal as the average value of the voltage between the circle and the square symbols in Fig. 3.4.

[4] On the ramps, the offset is estimated by linear interpolation between the offsets of the previous and successive plateau.

Fig. 3.5 and Fig. 3.6 show the estimated voltage offset and its effect on the flux, respectively.
The normal magnetization curve is evaluated by taking the points of each hysteresis loop corresponding to the plateau after the transient. The values of the pairs (H, B) are evaluated by averaging the values on the positive and negative plateaus, excluding the points that correspond to the transients.

3.3 System architecture

Fig. 3.7 shows the general architecture of the proposed measurement system. The sample is magnetized employing an excitation coil, which is supplied by a voltage-controlled current generator. First, a demagnetization cycle is carried out to put the sample in a reproducible magnetic state. Then, measurements are performed by ramping the current between positive and negative values. Each ramp

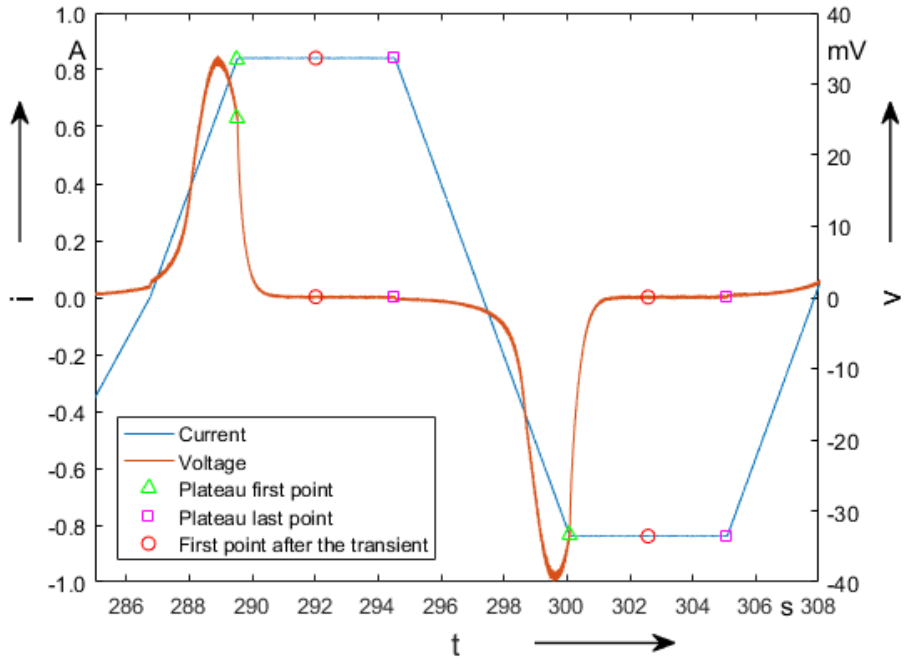

FIGURE 3.4: Normailized excitation current (light blue) and normalized sensing coil voltage curve (red). The triangle, circle and square symbols denote the begin of the plateau, the end of the transient phase and the end of the plateau, respectively.

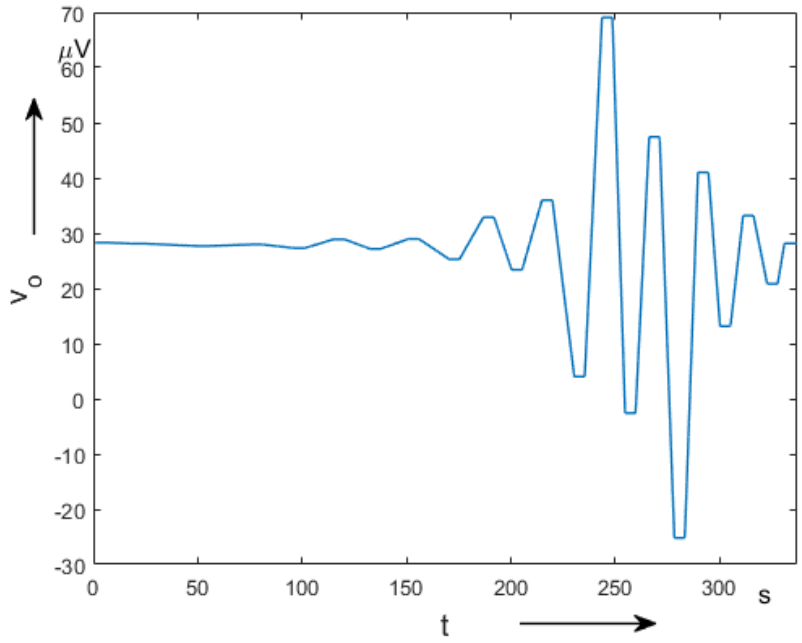

FIGURE 3.5: Example of estimated voltage offset.

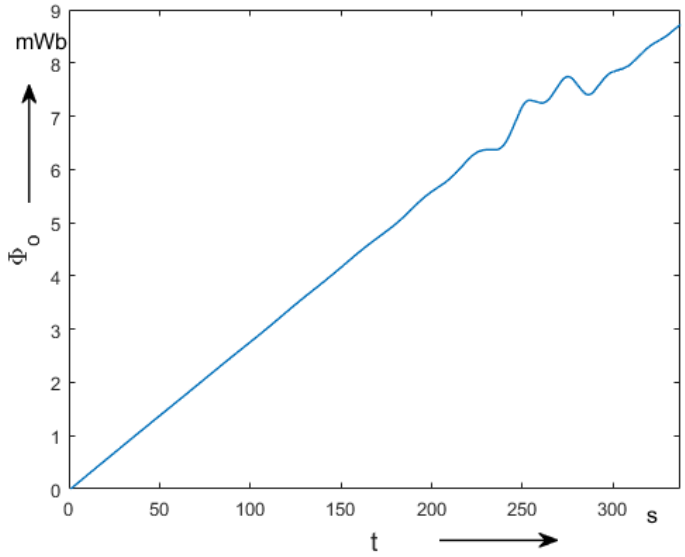

FIGURE 3.6: Flux offset corresponding to the voltage offset of Fig.3.5.

is followed by a current plateau, allowing for eddy currents to decay. Every time the current is ramped the amplitude is slightly increased to explore the initial magnetization curve progressively. During the excitation, the output voltages at both the measurement coil and the DCCT current sensor are continuously sampled and recorded. The voltage-controlled current generator, the digitizer, and the data acquisition board are integrated into an automatic PXI-based measurement station, linked to an external personal computer (PC). A suite of interactive programs, generated through the Flexible Framework for Magnetic Measurement (FFMM [10]), controls the station in order to i) calibrate both the power supply and the measuring instruments, ii) demagnetize the sample under test, iii) generate the magnetizing current, iv) acquire and scale the signal in order to display the hysteresis curve, and v) measure the permeability at field values defined by the operator. In the following, the specifications of the main hardware components are described.

A voltage-controlled current generator powers the excitation coils with a current within the range $\pm$ 40 A. The current ripple must be as small as possible to avoid modulations in the DC magnetizing field and variations of the flux density along minor hysteresis loops. The current ripple and noise peak-peak is 0.5 mA on a reference load inductance of 10 mH. The power supply is also equipped with an interlock panel that sets the output to zero in case of overload/overheating. In Tab.3.1 the electrical specifications of the power supply are shown. A DCCT current transducer measures the current carried by the excitation coils with high accuracy (nearly 10^{-5} A), allowing correcting the power supply's offset. The sensor used is a compact MACC^{PLUS} [131], a current measuring system based on the Zero-Flux principle. The acquisition system is hosted in an Analog Device PXI crate. It consists of an ADLINK PC, an NI PXI DAQ 4461 [74] and an NI PXI DAQ series M-6289 [75], as it can be seen in Fig 3.8. The specifications of the two NI acquisition systems are shown in Tab.3.2. The two input channels of

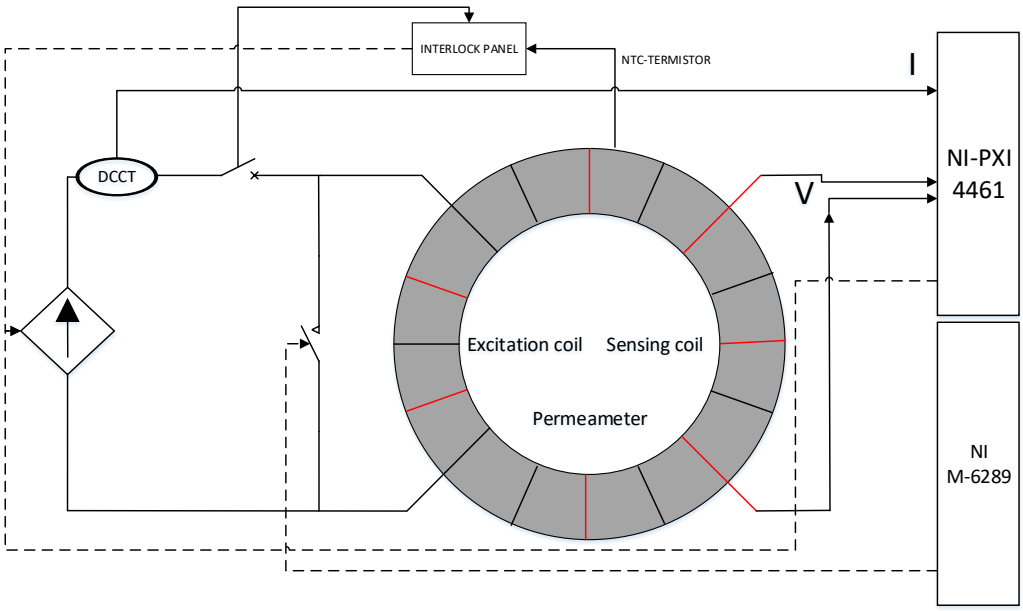

FIGURE 3.7: Layout of the measurement system.

Parameter	Quantity
Supply voltage	230±23 V
Output voltage	±15 V
Non-linearity	± 0.1 %
Ripple and noise	± 0.5 mA pk-pk
Rise time	± 8 A/s
Temperature coefficient	0.2 % /K

TABLE 3.1: Power supply specifications

(a) (b)

FIGURE 3.8: (a): NI DAQ series M-6289; and (b): NI DAQ 4461

the NI DAQ 4461 are used to measure the current in the excitation coil and the voltage at the terminals of the sensing coil. The high number of bits allows measurements to be performed with very high resolution. Another advantage is the possibility of using a very high sample rate (up to 204.8 kS/s). The NI DAQ 4461

Parameters	NI 6289	NI 4461
Analog input (ADC) resolution	18 bit	24 bit
Maximum range	$\pm$ 10 V	$\pm$ 42.4 V
Minimum range	$\pm$ 0.1 V	$\pm$ 0.316 V
Sample rate	625 kS/s	2014.8 kS/s
Analog output (DAC) resolution	16 bit	24 bit
Maximum range	$\pm$ 10 V	$\pm$ 10 V
Minimum range	$\pm$ 1 V	$\pm$ 0.1 V

TABLE 3.2: Specification of the NI DAQ M-6289 and 4461.

also generated the signal that controls the power supply with a high-resolution digital-to-analogical converter. A drawback is the poor stability of the first samples, due to an initial transient. The adopted solution solves this problem by adding an automatic switch in parallel to the excitation coil. Switch controlled by a digital signal generated by the M-6289. During the transient, the switch is closed and it short-circuits the excitation coil. When the current is stabilized, the switch opens, the current passes through the excitation coil, and measurements can be performed. The measurements are performed by using a customized software developed in C++ and embedded in the FFMM (Flexible Framework for Magnetic Measurements) [17] framework.

3.3.1 Split-coil permeameter

The split-coil permeameter is an instrument conceived at CERN in the 1967 [64]. It is shown in Fig. 3.9. The split-coil permeameter consists of three toroidal coils

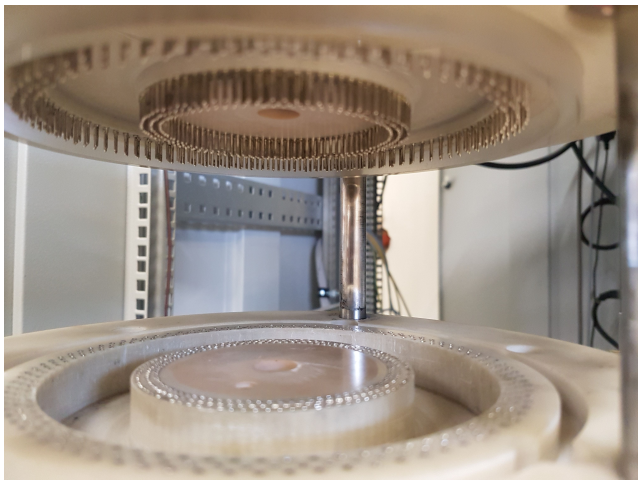

FIGURE 3.9: The split-coil permeameter.

that can be opened and closed using a customized mechanism. The design of the instrument is shown in Fig. 3.10. This system allows room temperature tests of

materials' magnetic properties to be performed much faster than using a standard flux-metric based measurement system. Splitting the coils into two halves has the drawback of localized heating, having two connections per turn, all in series. To curtail this problem interconnections of excellent quality have been used. The two outer coils are, generally, connected in series forming an excita-

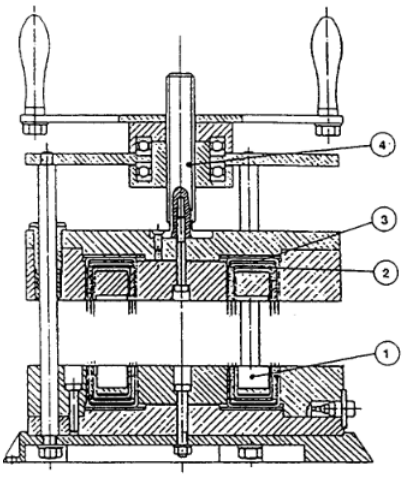

FIGURE 3.10: Section drawing of a split-coil permeameter: 1; Ring sample; 2. Sensing coil; 3. Excitation coil; 4. Opening system.

tion coil of 180 turns. With this configuration and a current of 40 A, a maximum field of 24000 A/m can be generated. The choice of the maximum current is due to a thermal limit. A circuit breaker is used to protect the instrument against overload. The circuit breaker is equipped with an auxiliary contact that monitors the position of the breaker. When the breaker opens, the auxiliary contact closes send a command to an interlock panel that blocks the power supply. An NTC-thermistor monitors the temperature of the coil. When the temperature of the coils is above a certain threshold, a digital signal is sent to the interlocking panel to block the power supply. The inner coil of 90 turns is, generally, adopted as sensing coil. The instrument can accommodate a ring sample up to 19.5 mm thick, having inner and outer diameters of 76 and 114 mm, respectively, and a cross-sectional area A_s usually derived from the geometry.

3.3.2 Cryogenic permeameter

The split-coil permeameter cannot be employed at the typical temperatures of the superconducting magnets for particle accelerators (T<=4.2 K). Hence, a cryogenic permeameter has been developed and installed at CERN' Cryolab test facility. The cryogenic permeameter allows magnetic characterization of materials to be performed at the cryogenic temperatures of 4.2 K in liquid helium and 77 K in liquid nitrogen. The layout of the system architecture is shown in Fig. 3.11. The measurement principle is the same as for the split-coil permeameter. At cryogenic temperature, the effect of the temperature variations can be neglected because the heat generated from the excitation coil is much lower than the cooling power of the cryogenic bath.

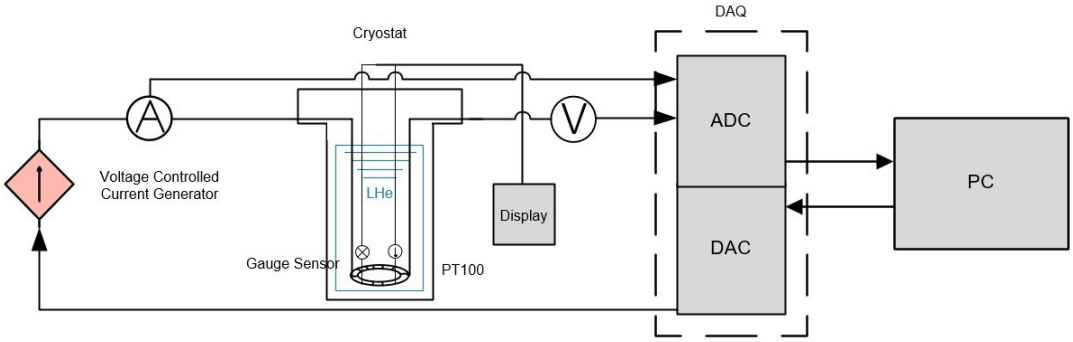

FIGURE 3.11: Layout of the Cryogenic measurement system

The sample under test needs to be manually wound with a sensing and an excitation coil. Generally, the sample is inserted in a case of non-thermo-shrinkable material, typically aluminum. In this way, the sample is protected from the mechanical strain generated by the shrinkage of the coil around the sample, which may alter the sample's magnetic properties. Usually, the sample is wound with an excitation coil with 180 turns and a sensing coil of 90 turns. In the standard configuration for soft magnetic materials, the coils are made of a copper strand of 0.5 mm^2. During a measurement, the sample and the coils are immersed in a cryogenic liquid inside a cryostat. The level of the cryogenic liquid has to be monitored because it evaporates during the process of measurement. A complete cryogenic test requires at least a working day. Fig.3.12 shows the sample prepared

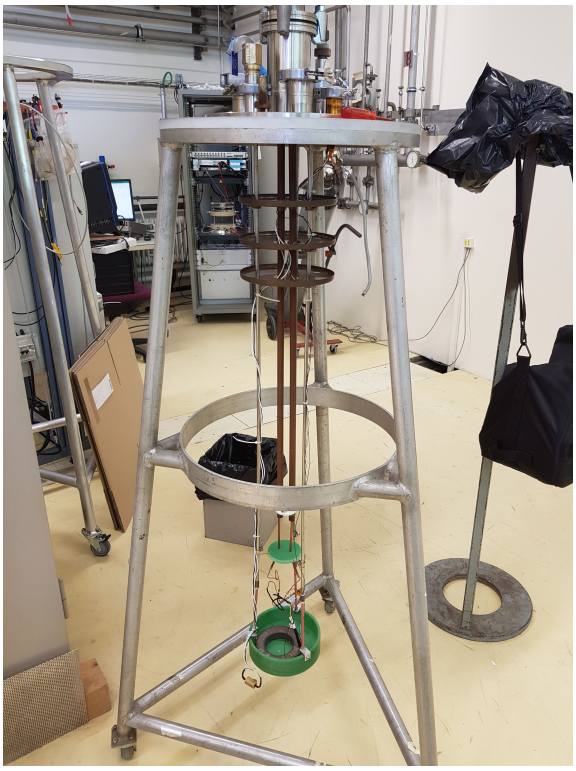

FIGURE 3.12: Sample installed in the cryostat.

to be inserted in the cryostat.

3.3.3 Superconducting permeameter

The superconducting permeameter is an upgrade of the cryogenic permemeter based on a superconducting excitation coil. This leads to differences concerning sample preparation and to adopting a quench protection system. Two power diodes with a nominal current of 90 A and 600 V of nominal voltage are placed in anti-parallel for the quench protection. In Fig.3.13, a sample cross-section is shown. The sample is inserted in a case of Bluestone to prevent mechanical strain due to thermal shrink. Bluestone has been chosen among other alternatives, such as Nylon Glass Fiber, for its very low thermal coefficient (0.01% /K). In order to avoid sharp edges, the case has been designed to host a sample with a squared cross-section, but has the corners shaped as in Fig. 3.13.

Coils are wound directly on the case. The innermost layer is the sensing coil

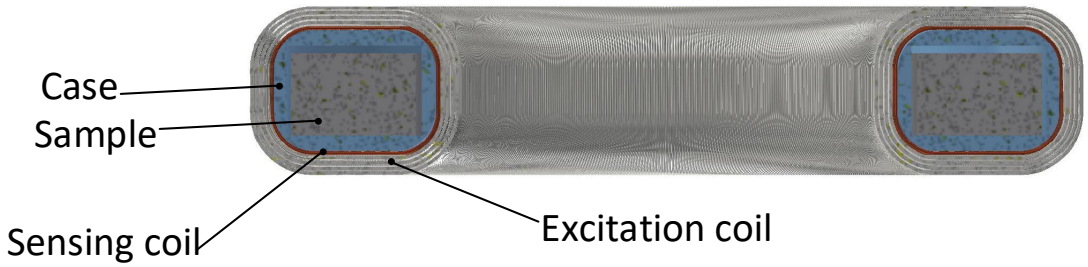

FIGURE 3.13: Sample cross-section view.

of 90 turns and 0.5 mm in diameter. The excitation coil is made of 4 layers, each one separated from the next by means of a layer of tape to prevent movement and mechanical disturbances. The superconducting cable used as excitation coil is a product of the Furukawa Electric Co., Ltd., which has the specifications shown in Fig.3.14. This product has been chosen due to its low cost (1 €/m), specifications regarding critical current and critical magnetic flux density and high value of insulation breakdown voltage (> 2000 V AC, Polyvinyl Formvar). The cross-sectional diameter of the strand is 0.5 mm without insulation and 0.55 mm with insulation in Polyvinyl Formvar. The strand has a minimum residual-resistivity ratio (RRR) lower than 100 and a matrix in oxygen-free copper with a superconductor-to-copper ratio equal to 2. The four layers of the excitation coil have respectively 566, 484, 459 and 426 turns.

3.4 Quench protection

A quench refers to the sudden loss of superconductivity when the coil temperature is raised. In the superconducting state, the resistance of the coils is zero, and hence no energy is required to maintain current flow. If the coil temperature

Specifications for NbTi Round Wire · F830/2.0 series

Furukawa Electric Co., Ltd.
Spec. No. SCH-1114D
November 14, 2014

Type		F830/2.0/50	F830/2.0/65	F830/2.0/75	F830/2.0/85	F830/2.0/100
Superconductor		Nb-47±1wt%Ti	Nb-47±1wt%Ti	Nb-47±1wt%Ti	Nb-47±1wt%Ti	Nb-47±1wt%Ti
Bare Wire Diameter	(mm)	0.50 ± 0.01	0.65 ± 0.01	0.75 ± 0.01	0.85 ± 0.01	1.00 ± 0.01
Filaments						
- Mean Diameter (nominal)	(μm)	10.0	13.0	15.0	17.0	20.0
- Number of Filaments (nominal)		830	830	830	830	830
- Twist Pitch	(mm)	12 ± 2	15 ± 2	18 ± 2	19 ± 2	20 ± 2
- Twist Direction *1)		S	S	S	S	S
Matrix		Oxygen Free Copper	Oxygen Free Copper	Oxygen Free Copper	Oxygen Free Copper	Oxygen Free Copper
Cu to Superconductor Ratio		2.0 ± 0.2	2.0 ± 0.2	2.0 ± 0.2	2.0 ± 0.2	2.0 ± 0.2
Insulation						
- Material		Polyvinyl Formvar	Polyvinyl Formvar	Polyvinyl Formvar	Polyvinyl Formvar	Polyvinyl Formvar
- Breakdown Voltage	(Vac)	> 2,000	> 2,000	> 2,000	> 2,000	> 2,000
- Insulated Diameter	(mm)	0.55 ± 0.02	0.70 ± 0.02	0.80 ± 0.02	0.90 ± 0.02	1.05 ± 0.02
Minimum Critical Currents at 4.2K and 10^{-13}Ωm						
- Ic at 5T	(A)	> 160	> 280	> 370	> 475	> 660
- Ic at 6T	(A)	> 130	> 220	> 290	> 370	> 520
- Ic at 7T	(A)	> 100	> 170	> 220	> 280	> 400
Minimum RRR		> 100	> 100	> 100	> 100	> 100
Minimum Piece Length	(m)	5,000	5,000	3,000	3,000	3,000
Number of Piece		≦ W/50	≦ W/50	≦ W/50	≦ W/50	≦ W/50
Total weight	(kg)	W (TBD)	W (TBD)	W (TBD)	W (TBD)	W (TBD)
Length (nominal)	(m)	TBD	TBD	TBD	TBD	TBD

[Notes]
*1) Twist Direction "S" means the left hand screw twist.

FIGURE 3.14: Specifications of the superconducting strand.

rises above the superconductivity threshold, the coil suddenly develops a higher resistance. A current passing through this higher coil resistance creates heat. This heat causes a sudden, boil-off of liquid helium. A quench can occur because the field inside the magnet is too large, the rate of change of field is too large (causing eddy currents and resultant heating in the copper support matrix), or a combination of the two. More rarely a defect in the magnet can cause a quench or the current density too high.
The quench protection analysis aims to assess if the intended currents for the magnet design are safe for operation. This means calculating the hotspot temperature of the magnet during a quench and assessing if the magnet is in need of any form of quench detection.
The protection studies consist of three cases, at the operating currents of 40 A, 80 A and 150 A, at a temperature of 4.2 K. The studies consist of several models with different tools. The first model calculates the magnetic flux density B in the magnet coil and the inductance of the coil in COMSOL. Further, a QLASA [116, 96] model was created using the magnetic flux density and inductance values from COMSOL. Lastly, the QLASA model was coupled with a PSpice circuit.

The COMSOL model is an axisymmetric 2D model of the cross-section of the toroidal coil. In the model, the cross-section of the iron sample and the Bluestone case around the sample have the same dimensions as the real torus and

case, whereas the shape of the coil is simplified. The new coil consists of a single conductor with the same current density as each winding in the original coil. The thickness of this simplified conductor scales proportional to the inverse of the radius of the torus, see Fig.3.15. This scaling compensates for the fact that the winding density reduces with the radius of the torus.

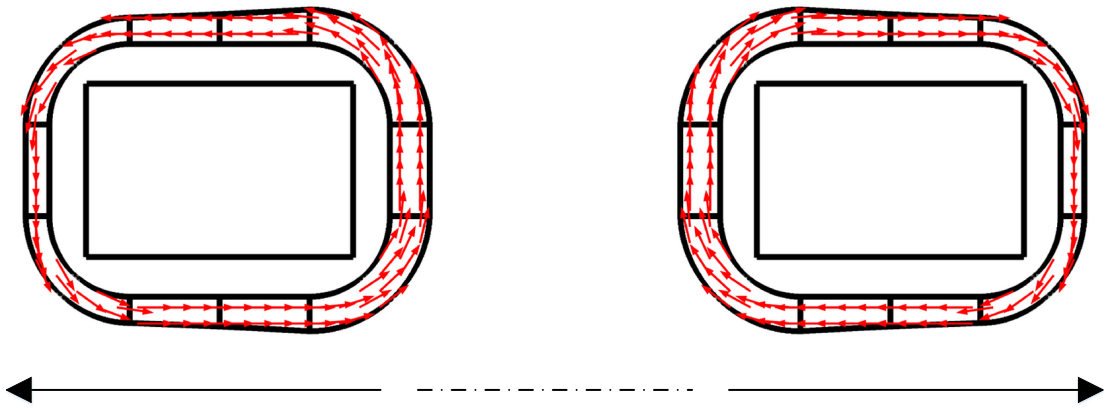

FIGURE 3.15: Current distribution used in the simulations.

From the COMSOL model, the magnetic flux density in two given points of the coil(P_1 and P_2) are extracted, see Fig.3.16. The points are located inside and outside of the coil, at the smallest radius of the torus. At these points, the max value of the magnetic flux density is found. To calculate the inductance, COMSOL uses the two equations for magnetic energy $U = \frac{1}{2}LI^2$ and $U = \frac{1}{2}\int_\Omega \boldsymbol{B} \cdot \boldsymbol{H} d\Omega$, which yield

$$L = \frac{1}{2I^2} \int_\Omega \boldsymbol{B} \cdot \boldsymbol{H} d\Omega. \tag{3.8}$$

The magnetization curve for the iron in COMSOL is based on the curve from the MB simulations in ROXIE. The values calculated by COMSOL are shown in Table 3.3.

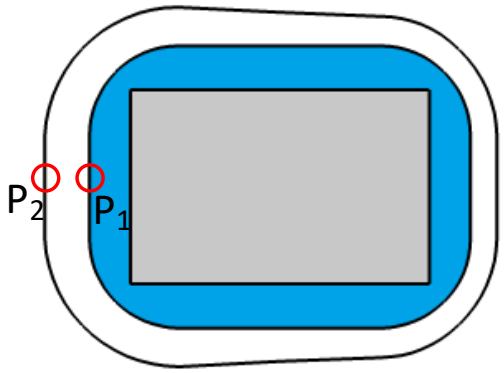

FIGURE 3.16: Cross-section of the toroidal coil with the two points, P_1 and P_2.

Current I	Inductance L	$B(P_1)$	$B(P_2)$
40 A	0.04592 H	0.0040 T	0.5733 T
80 A	0.02971 H	0.0080 T	1.1466 T
150 A	0.02213 H	0.0149 T	2.1500 T

TABLE 3.3: Values of the magnetic flux density and inductance for current value.

QLASA is an analytic 3D tool to calculate the quench behavior of superconducting solenoids. Some assumptions were made to use QLASA on a toroidal coil and the toroidal geometry was transformed into a solenoid.
The toroidal coil is transformed into a solenoid by assuming constant cross-section and volume of the coil. The cross-section winding area of the solenoid, in Fig.3.17 (left), is approximated by the area of the innermost cross-section of the windings in the r-theta-plane of the toroidal (right). The length of the solenoid is approximated to the innermost circumference of the torus with windings.

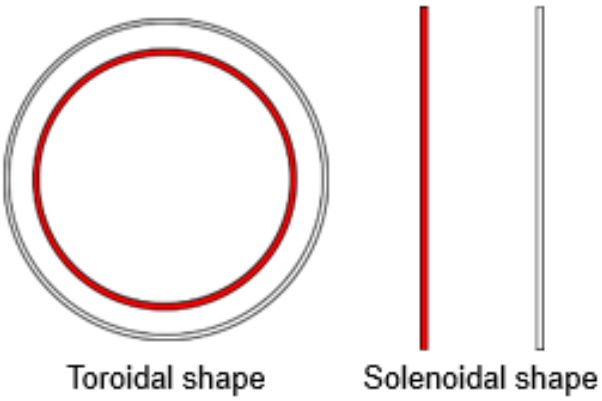

FIGURE 3.17: Cross-section area of torus in r-θ-plane and solenoid in r-z-plane. Red areas are kept constant.

The QLASA model assumes the magnetic field around the solenoid to be symmetric with respect to the center of the solenoid. This is not the case for the toroidal coil, where the field varies with the radius of the torus. To achieve conservative results in the simulations, the peak values of the magnetic flux density at the outside and inside of the solenoid is respectively set to P_1 and P_2. The magnetic flux density is assumed constant along the length of the solenoid.
The QLASA simulations are based on adiabatic conditions, which implies no heat transfer to the surrounding helium. Assuming adiabatic conditions for the toroidal coil is reasonable since the coil wires are isolated from the helium bath, and the heating of the coil due to a quench happens in a time interval on the scale of 100 ms.
PSpice is used to simulate a circuit with the same properties as in the experimental setup. The circuit setup has been simulated by adopting a power converter in parallel with the diode, represented using a switch in series with a resistance

R_D equal to 1 mΩ, and the toroidal coil, represented using an inductance in series with variable resistance. At nominal operation, the crowbar is open, and the power converter supplies a constant current through the coil, as shown in Fig.3.18. The crowbar is open and the current flows through the load, with $r(t)$ equals to zero. During a superconductor quench, the resistance $r(t)$ in the coil grows, and consequently the coil voltage increases. Once the voltage over the coil reaches a certain threshold, the power converter turns off, and the crowbar closes.

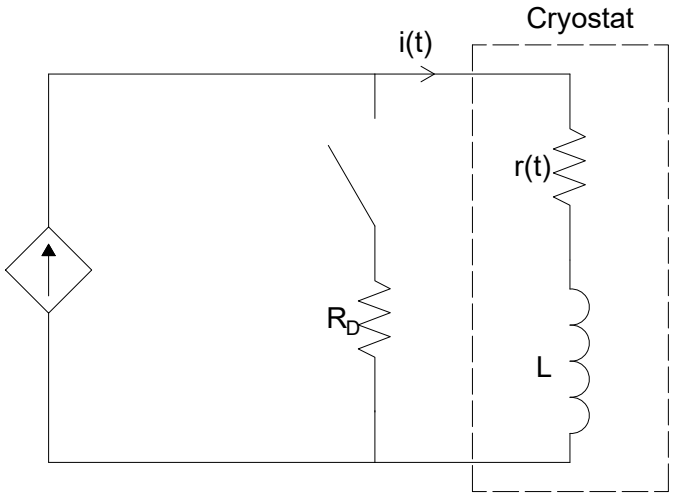

FIGURE 3.18: Electrical Circuit used for the quench protection simulations.

QLASA and PSpice are used together in the cooperative simulation framework STEAM-COSIM [28, 130, 91], where the resistance growth calculated by QLASA can be used in a custom circuit in PSpice. STEAM-COSIM is used because the internal circuit setup in QLASA is not sufficient to simulate the actual circuit setup of the experiment.
In the simulations, the crowbar resistance is set to 1 mΩ and the voltage threshold over the coil is set to 1 V. The results of all the operating currents for a current of 40, 80 and 150 A are shown in Fig. 3.19. From the results, the hotspot temperature rises to a maximum value of 30.4 K for 40 A, 46.5 K for 80 A and 69.7 K for 150 A, i.e., well below 100 K at which the increase in thermal expansion coefficient may result in increased stress. The results show that the toroidal coil is self-protected in all the study cases.
The threshold voltage of the power controller governs the limit of the ramp rate in the coil. The average max ramp rate is calculated from $(dI/dt)_{max} = V_t/L$, where V_t is the threshold voltage and L is the inductance reported in Table 3.3. With the threshold voltage set to 1 V, the average max ramp rate is 21.7 A/s for 40 A, 33.7 A/s for 80 A and 44.2 A/s for 150 A.

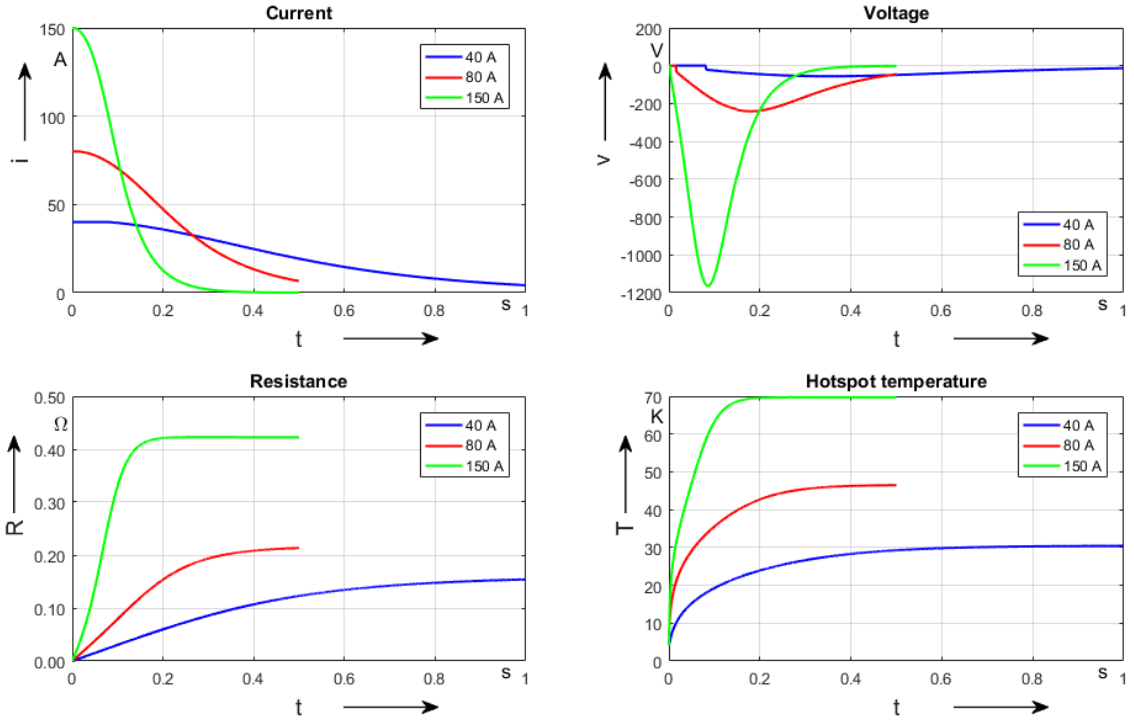

FIGURE 3.19: Current decay and hotspot temperature for three case studies.

3.5 Uncertainty assessment

In case of an initial magnetization curve obtained employing a point-by-point method, the IEC 60404-4 standard prescribes to adopt 2% of uncertainty on the values of the magnetic field and magnetic flux density, if current and voltage waveforms are acquired with an uncertainty lower than 1%. In this section, a more in deep the metrological performance of the proposed measurement system is presented. The used approach follows the standard Guide to the Uncertainty of the Measurement (GUM) [58]. In Fig.3.20, the architecture of the method with the measurement quantities and the main uncertainty sources is shown.

In Fig.3.21, the percentage uncertainty on the magnetic flux density, as function of the magnetic field, for a weakly (ITER Stainless steel), two soft (M140-50A and M800-100A) and a high-μ material (CRIOPHY) are shown.

The relative uncertainty always decreases as the current increases. The two steps in the soft magnetic materials' curves at 200 A/m and roughly 1500 A/m corresponds to a change in the gain of the ADC current channel. For magnetic fields lower than 1000 A/m, the values of the magnetic flux density of the M140-50A are slightly higher than the values of the M800-100A. Hence, also the uncertainty curve shows the same small discrepancy at low fields. In saturation both materials have the same behavior, and also the relative uncertainties are equal.

For a high-permeability material, such as CRYOPHY, the uncertainty goes from 10% at low magnetic fields to 0.8% at higher fields. The high uncertainty at low fields can be justified with the number of turns of the excitation coil of the split-coil permeameter (minimum 90, maximum 180). This does not allow to generate

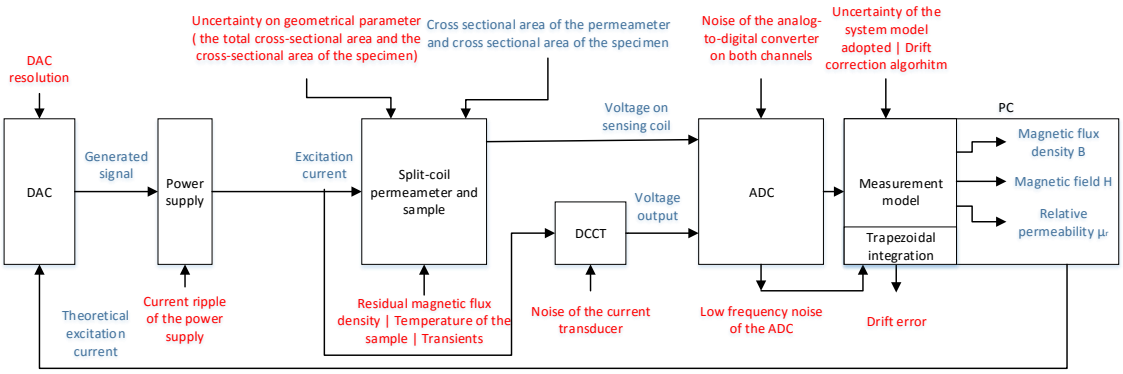

FIGURE 3.20: Architecture of the method with the measurement quantities (light blue) and the main uncertainty sources (red).

values of magnetic field small enough to be suitable for characterizing this kind of material. Another drawback of using the split-coil permeameter for such a high-μ_r steel is the difficulty in demagnetizing the material, with a high value of the residual flux density (about 0.2 T). This is due since the response of the material is very sensitive to external disturbances on the sensing coil's voltage. These are the reasons why the CRYOPHY for the magnetic shielding of the cryomodule of the crab cavity experiment at CERN has been tested using a customized set of 10-turns coils wound on the sample itself, details in chapter 6.
For a weakly magnetic material as the ITER stainless steel, the value of the uncertainty is always above 2%. This because, having the material a very low relative permeability ($\mu_r < 2$), the sensing coil' signal has a lower signal-to-noise ratio. A very low sensing coil' signal means having a small flux. Hence, in Eq. 3.4 the first addend becomes smaller and the contribution of the second addend becomes comparable with the first addend, increasing the uncertainty of the overall results. When testing stainless steel with the proposed method, the uncertainty at low fields is around 10%. The results of the magnetic characterization show that the material has a linear B-H relation. Hence, for reducing the overall uncertainty of the results, the approach proposed in chapter 4 has been employed for characterizing the stainless steel of the ITER's TF coils, details in chapter 6.
Fig.3.22 shows the relative expanded uncertainty on the magnetic flux densities of a soft magnetic material (M140-50A), when tested at the cryogenic temperature of 4 K. For the same class of material, the results at cryogenic temperature are affected by a higher uncertainty than at room temperature. An explanation of this could be the lower voltage signal induced in the sensing coil at these temperatures. A general recommendation for improving the measurement accuracy is to machine a sample with a thickness of, at least, 15 mm. This would also reduce the heating effect, having more volume. Another recommendation is to adopt a sample made of laminations. In order to reduce the eddy current effects, and consequently the duration of the transients, and consequently the overall time of measurement. Finally, the sampling frequency of the acquisitions should be kept

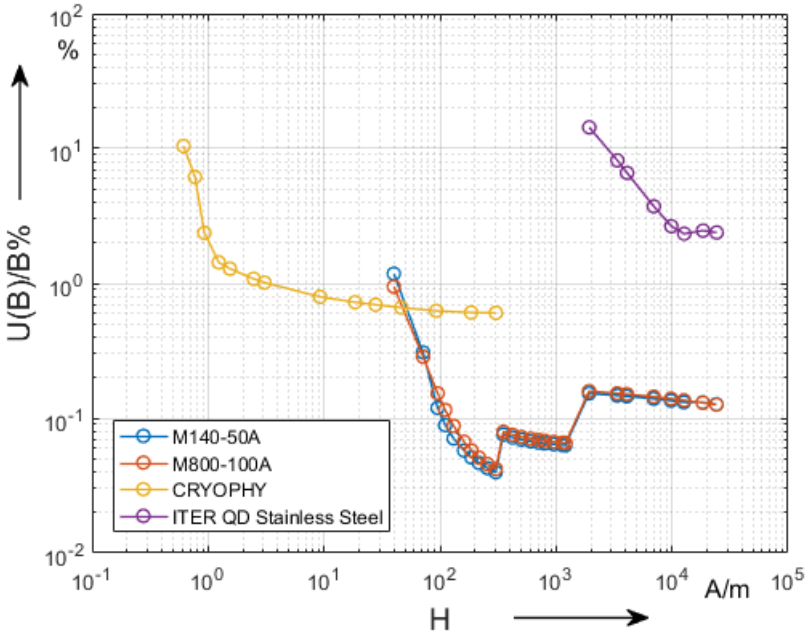

FIGURE 3.21: Expanded relative uncertainty of the magnetic flux density of several materials as function of the magnetic field. A coverage factor of 2 has been used.

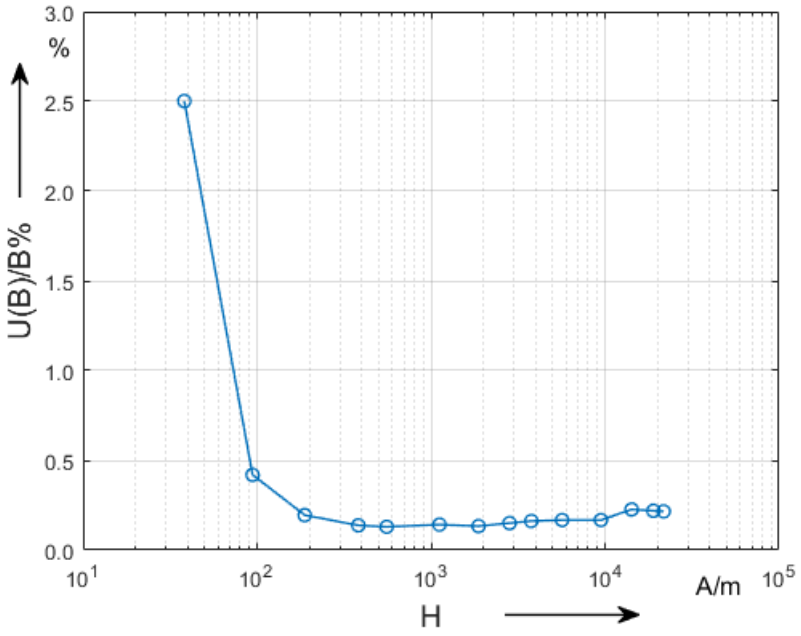

FIGURE 3.22: Relative expanded uncertainty, with a coverage factor of 2, on the cryogenic measurements of the magnetic flux densities of a soft magnetic material.

as higher as possible.

3.6 Conclusions

In this chapter, the problem of characterizing magnetic properties of the magnet's yokes at their operational temperature and saturation level has been addressed. The solution consists of a customized measurement system that employs superconducting coils and is based on a flux-metric method. The main problem of employing superconducting coils, an undesired quench, has been addressed successfully by specific quench protection simulations, which has lead to a self-protected system. An uncertainty model and a study of repeatability and reproducibility of the measurement procedure has been presented as well.

Chapter 4

Proposal for characterizing weakly magnetic materials

In this chapter, the design and validation of two methods for characterizing weakly magnetic materials, suitable to be used in the quality control of series production, are presented. An adapted-to-low-permeability-materials approach based on the previously introduced flux-metric method is proposed for characterizing material in the range of relative permeability among 1.1 and 6.0.
The results in therm of uncertainty are not satisfying when μ_r goes below 1.1. Hence, for materials with a relative magnetic permeability μ_r less than 1.05, a measurement system based on a novel magneto-metric method has been conceived and designed.

4.1 Proposed flux-metric based method

In this section, the adapted-to-low-permeability-materials approach based on the previously introduced flux-metric method is proposed for characterizing material in the range of relative permeability among 1.1 and 6.0. The method consists of applying excitation current curves with different ramp rates and measuring the respective relative permeabilities. A linear relationship between the relative permeability peak and the ramp-rates of the corresponding cycle is obtained. Consequently, by linearly fitting the relative permeability peaks values and extrapolating the ones corresponding to a null ramp rate, the relative permeability without the dynamic effect has been estimated.

4.1.1 Basic idea

The procedure is based on the assumption that eddy current effects in the sample can be neglected. When the permeameter is employed for weakly magnetic materials, this hypothesis is even more reasonable. For instance, considering the case study that will be presented in this work, the typical skin depth of stainless steels is about $600\ mm$ at the frequency corresponding to the fundamental period

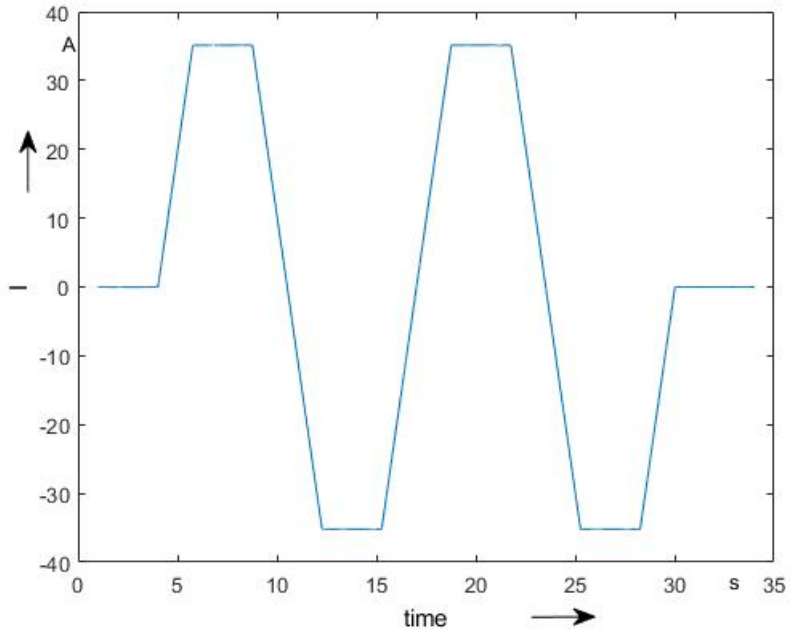

FIGURE 4.1: Example of the current driven through the excitation coil.

of the excitation, i.e. about $10\ s$. This assumption allows extrapolating the relative permeability curve straight from the initial magnetization curve.

To further cancel the influence of possible residual dynamic effects, the permeability should be measured in steady state conditions. At this aim, the excitation current has to exhibit three different cycles reaching the same maximum level on the plateau, but characterized by three different ramp-rates. As regards the maximum current level, it has to be high enough to bring the sample in saturation; hence it depends on the material under test. For each cycle, the corresponded B-H hysteresis curve is obtained according to the classical measurement method reported in Chapter 3 and the corresponded relative permeability curve can be evaluated. From the permeability curves, then, the parameter relative permeability peak (RPP) is straightforwardly estimated. In Fig. 4.2, as an example, three RPP values, obtained for three different ramp rate values, are shown. A linear relation between the RPP and the ramp-rates of the corresponding cycle can be detected. As a consequence, by linearly fitting the RPP values and extrapolating the RPP corresponding to a null ramp rate, the relative permeability without dynamic effect can be obtained.

4.1.2 Uncertainty source evaluation

In this section, the problems related to the use of the adapted-to-low-permeability flux-metric method for measuring the magnetic properties of weakly magnetic materials are faced.

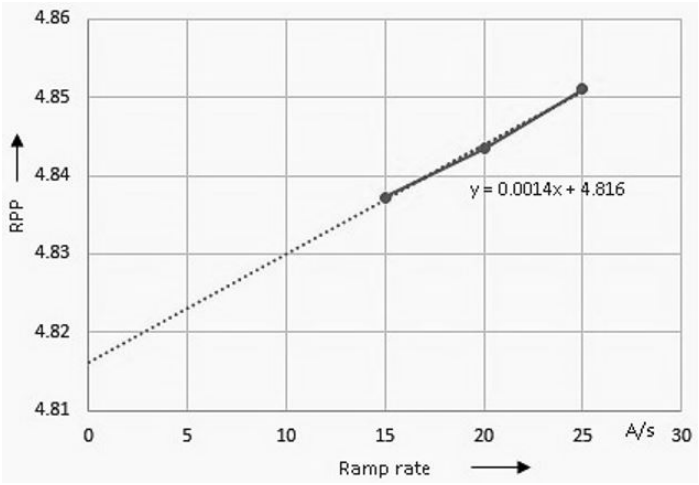

FIGURE 4.2: Relation between relative permeability estimation and ramp-rate.

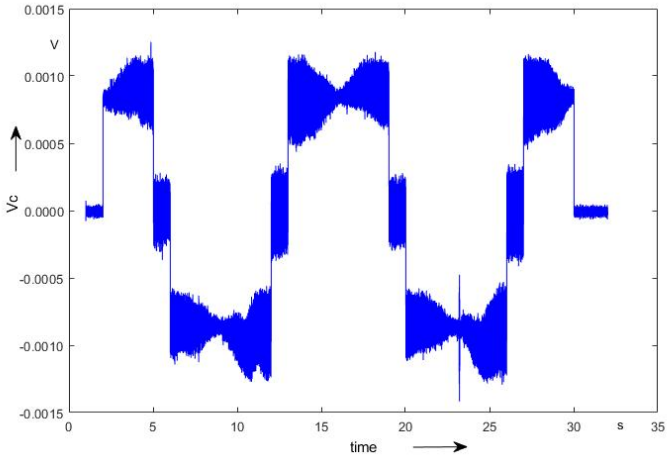

FIGURE 4.3: Example of measured voltage from the sensing coil.

Signal-to-noise ratio

The weakly magnetic materials are characterized by much lower induction values if compared with high–permeability materials. As a consequence, the electromotive force (*emf*) induced on the sensing coil of the transducer exhibits an amplitude of a few mV. An example of the signal acquired at the sensing coil is shown in Fig. 4.3. The signal is characterized by an unsatisfying signal-to-noise ratio (SNR), which could affect the overall accuracy of the permeability measurement. In order to enhance the performance, an analog filtering stage is required for removing the noise affecting the *emf* signal before its digitization.

Radial dependence of $\boldsymbol{\mu}_r(\mathbf{H})$

It is not taken into account that $H(r)$, and hence $\mu_r(H(r))$, depend upon the radial position of each tape turn. The approximation made by lumping the roll at

r_0 is equivalent to making an average across the peak of the $\mu_r(H)$ curve, leading thus to an underestimation of the peak permeability. The corresponding uncertainty depends upon the shape of the $\mu_r(H)$ curve and is often up to 2% for high-permeability steel samples.

Co-wounded tape sample

In this application, the samples are made of co-wounded tape. This leads to some considerations negligible or absent in case of bulk samples:

1. The ring shape is irregular. Hence the cross-sectional area is derived from sample weight and density, instead of from geometry. This could increase uncertainty.

2. The tape is very thin compared to its length. Thus the magnetization vector is expected to lie in the plane of the tape, i.e. tangent to the roll turns. This means that the in-plane component of the permeability along the tape is measured essentially, by ignoring the effects of a possible anisotropy, e.g. in the radial direction across the tape thickness.

3. The tape has a spiral shape. Therefore an angle between the tape and the azimuthal H field vector arises. This angle, decreasing radially and averaging to roughly 0.2 mrad, causes a certain amount of flux leakage which is exacerbated by the very low permeability of the material. The small air gap between the turns represents an additional reluctance in the magnetic circuit, which is not taken into account, thus leading to a slight overestimation of the material permeability.

4. Additional flux leakage occurs at both the ends of the rolled tape. Some of this leakage escapes the measuring coil, while the remainder can be represented as an additional reluctance in series with the magnetic circuit. As the rolls have in general more than 200 turns, the impact on the measured permeability can be expected to be of the order of the percent. However, a more detailed study would be necessary to predict whether the net effect leads to over- or underestimation of the permeability.

Drift correction

Over and above the approximations as mentioned above, the largest uncertainty sources are the meager signal-to-noise ratio and the relatively high coil voltage offset, leading to integrator drift. As an example, the sensing coil voltage (Fig. 4.3), the uncorrected integrated flux (Fig. 4.4), the correct integrated flux (Fig. 4.5), and the estimated voltage offset (Fig. 4.6) are reported for a standard co-wounded tape of stainless steel. The signal level is of the order of 1 mV, while the peak-to-peak noise is roughly 0.5 mV. Integration gets rid of most of the high-frequency noise, but as seen in Fig. 4.4, the measured flux is affected by a noticeable drift over the 33 s measurement duration, corresponding to a peak-to-peak offset of roughly 5 μV. The offset is not constant during the measurement

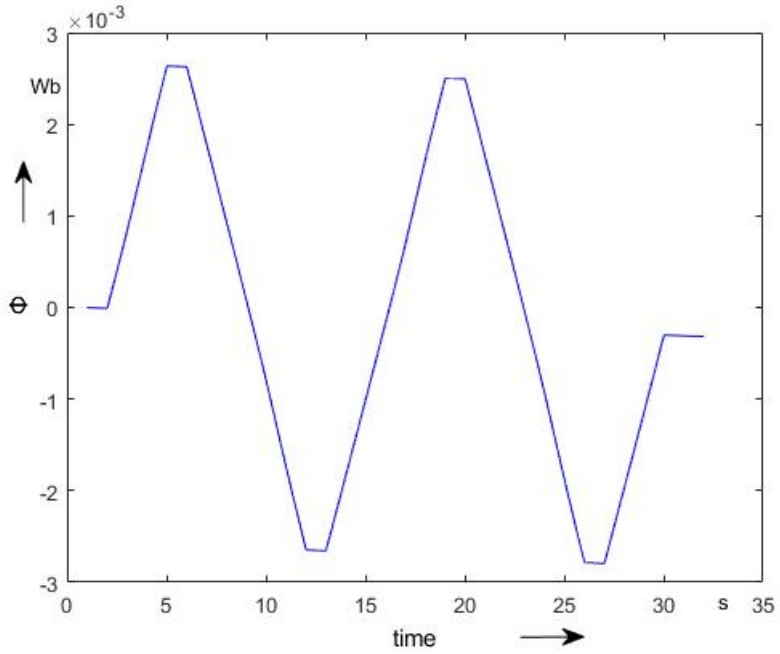

FIGURE 4.4: Uncorrected flux estimated from the sensing coil voltage.

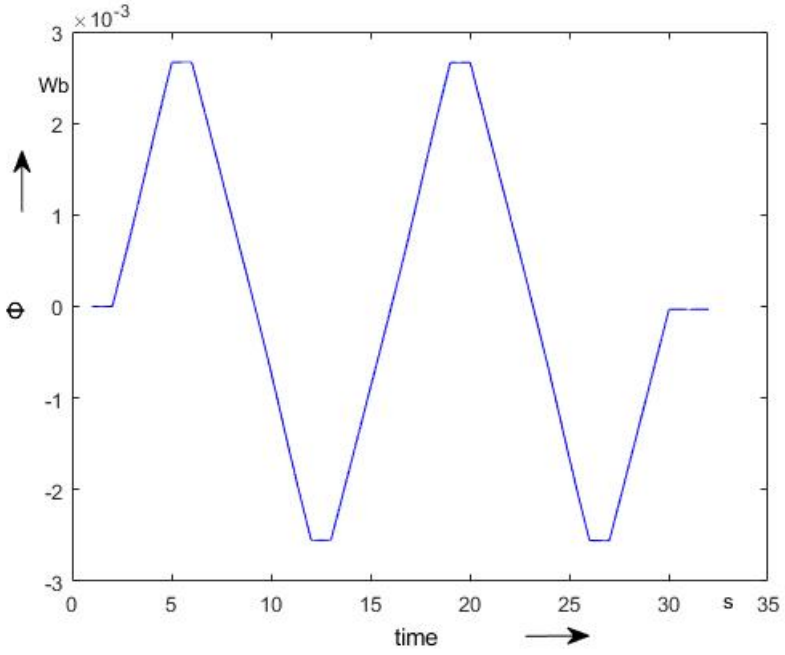

FIGURE 4.5: Flux estimated from the sensing coil voltage, drift corrected by means of the voltage offset estimation.

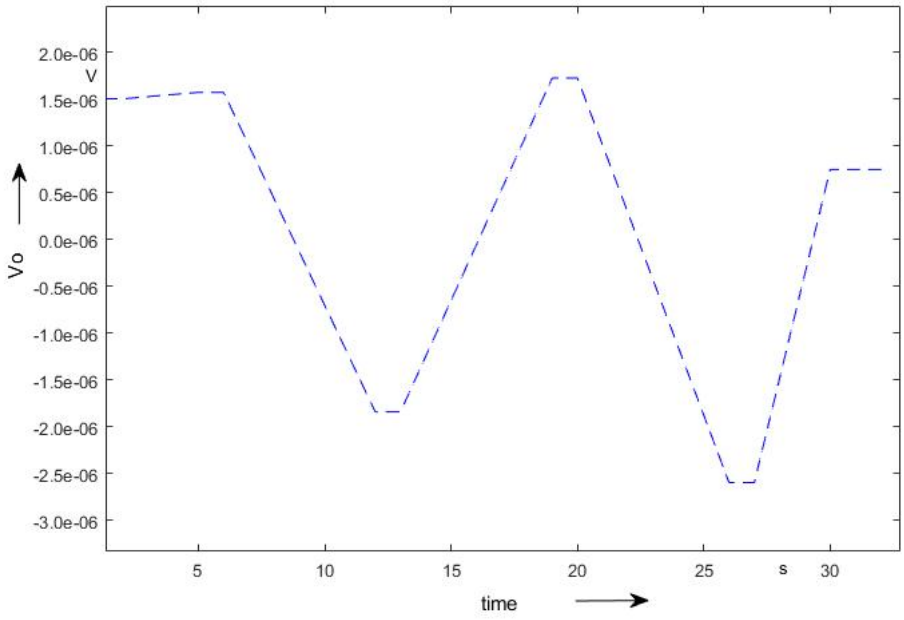

FIGURE 4.6: Measured voltage offset estimation.

and its evolution was estimated, as shown in Fig. 4.6, by making the following physics-grounded assumptions:

1. the measured flux does not change between the start and the end of a current plateau. This assumption is consistent with negligible eddy current effects.

2. the flux swing between current plateaux at maximum and minimum current is constant and equal to the average measured value. The symmetry of extremal magnetization states is justified by the rolls being prepared in either a demagnetized state or pre-cycled until stability is achieved before the measurement.

According to these assumptions, fluctuations of the offset of the order of $\pm 2.5\ \mu$V are estimated during the measurement. This result is consistent with similar fixed-coil measurements in other contexts. Among the possible causes of such time-changing offset, the relatively large thermal gradients developed in the apparatus during the test, as well as low-frequency noise due to aliasing, may be included.

4.2 Proposed magneto-metric based method

The proposed flux-metric method is not suitable to test materials with a μ_r lower than 1.1. Hence, to face the CERN requests of testing that materials, such as INERMET® IT180 for magnet radiation protection and the stainless steel for the new superconducting magnet collars, show a relative magnetic permeability peak lower than 1.005, a novel magneto-metric method has been conceived and designed.

4.2.1 Basic idea

The method is based on an inverse analysis approach coupled with a finite-element model. A material with unknown permeability is inserted into the air gap of a dipole magnet and the consequent perturbations of the dipole background flux density are measured and acquired in FFMM utilizing a Metrolab NMR sensor [101]. A positioning stage, controlled by an FFMM application, allows the sensor to move around the sample and to keep track of these positions. The relative magnetic permeability is then identified through grey-box inverse modelling, based on a finite-element approach. The 2D finite element model is realized in FEMM [100], while the inverse problem is solved in Matlab using a Levenberg-Marquardt algorithm. The schematic diagram of the measurement principle is shown in Fig. 4.7.

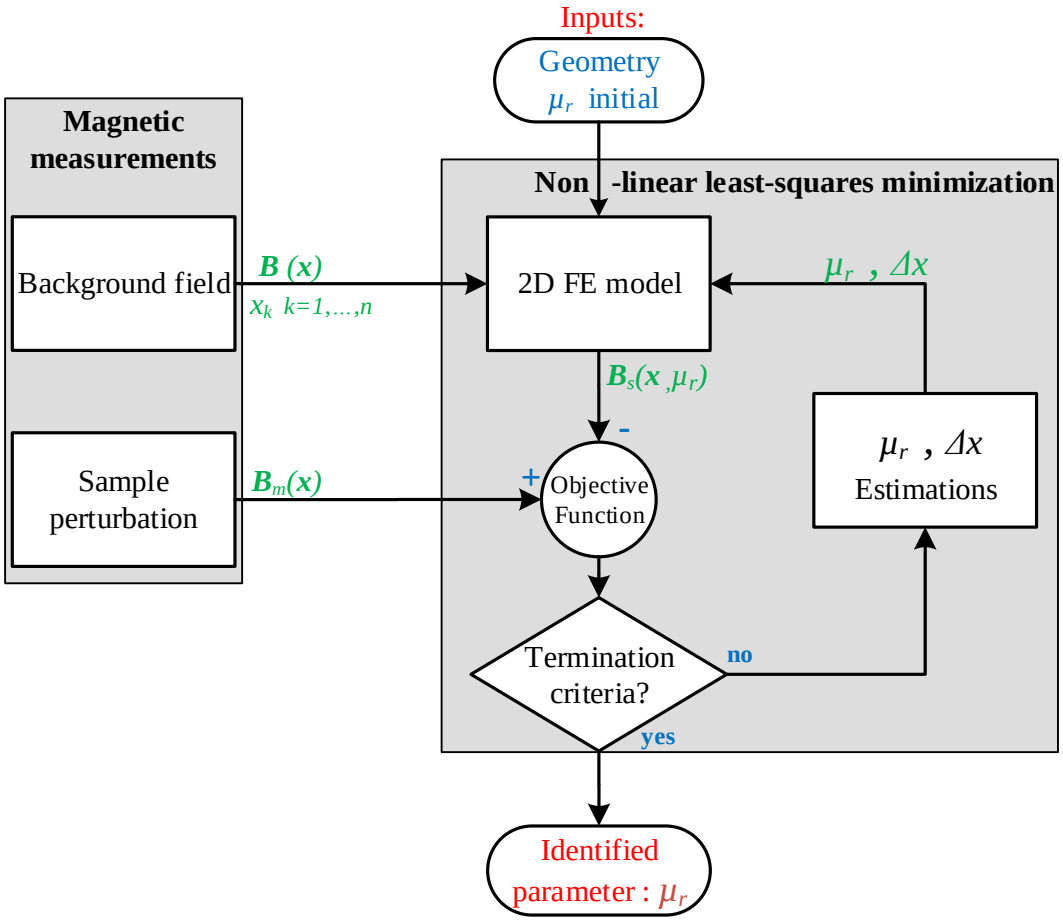

FIGURE 4.7: Flow chart of the proposed method.

4.2.2 Magnetic measurements

An essential part of the proposed method is to detect the perturbation of the background field due to the presence of the sample under test in the dipole magnet

utilizing local magnetic measurements.

Sample-induced perturbation measurements

A cylindrical sample is placed in the uniform field region of a reference dipole and the magnetic flux densities, $B_m(x_k)$, at different distances from the sample are measured with the NMR sensor. The coordinates, x_k with $k = 1, ..., K$ are measured and recorded. In this case, the problem is axisymmetric and the x axis could in principle coincide with any radius. Both the sample and the sensor are positioned symmetrically with respect to the midplane of the magnet gap.

Background field measurements

The same measurements are performed in the absence of the sample, under the same magnet excitation conditions.

4.2.3 Non linear least-squares minimization

The problem of the model response of physical experiments is called a forward problem, while the inverse problem theory concerns the problem of making inferences about a physical system starting from noisy measurements. An inverse problem is the process of calculating, from a set of observations, the causal factors that produced them; it is called an inverse problem because it starts with the results and then calculates the causes.
In general, inverse problems are essentially defined as the identification problem of unknown parameters from indirect measurements. The values of the unknown model parameters are recovered by iteratively minimizing the residual between the computer forward model responses and the physical measurements.
In this application, the unknown parameter is the relative permeability of the sample under test; the physical measurements are the values of the flux density $B_m(\mathbf{x})$ measured by the NMR Teslameter; and the computer forward model responses are the flux density $B_s(\mathbf{x}, \mu_r)$ provided by a 2D FE model of the open circuit measurement system.

Finite Element Modeling

The numerical model of the open circuit measurement system is constructed using a 2-D finite element method in FEMM, using Lua as scripting language [113]. The following assumptions have been made: i) the geometry is locally 2D; ii) the permeability in the sample is uniform and iii) inserting the sample inside the magnet does not affect appreciably its total reluctance (or, in other words, the boundary conditions for the FE model correspond to a uniform field with and without the sample).

Objective Function

We have considered an objective function OF representing the quadratic error between the measured and simulated quantities:

$$[\mu_r^*, \Delta x^*] = \arg \min_{\mu_r, \Delta x} OF(\mu_r, \Delta x, \mathbf{x}) \tag{4.1}$$

where μ_r^* is the estimated relative magnetic permeability of the material and Δx the estimation of the distance sample-sensor offset. The first formulation ($C1$) is simply the quadratic sum of the relative differences between measured and simulated field. To improve accuracy a least squares approach has also been applied to the model, making the assumption that all variables are contaminated by noise, see Fig. 4.8. The main sources of uncertainty are the conformity to the model assumptions ϵ_g; the flux density measurements ϵ_B and the position measurements, characterized by two contribution, a systematic $\epsilon_{\Delta x}$ and an random ϵ_x.

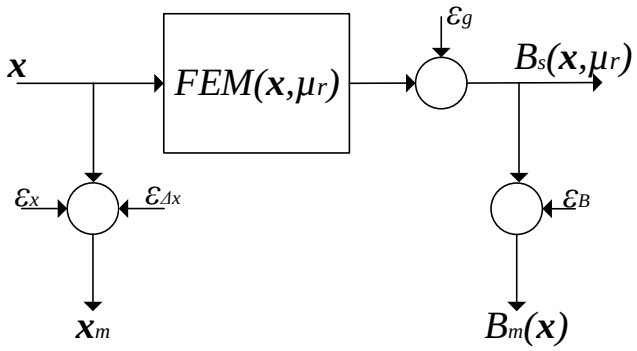

FIGURE 4.8: Diagram of the errors-in-variable approach

If the reasonable assumptions ($C2$) $\epsilon_g >> \epsilon_B$ and $\epsilon_{\Delta x} >> \epsilon_x$ are made, the objective function, can be written as follows:

$$OF(\mu_r, \Delta x, \mathbf{x}) = \sum_{k=1}^{K} \Big(\frac{B_s(x_k + \Delta x, \mu_r) - B_m(x_k)}{B_m(x_k)} \Big)^2. \tag{4.2}$$

The proposed method is general and could be used with different sample geometries (cube, bar, sphere) provided that appropriate 2D or 3D FE modeling is used. The main drawback is that it is not suitable for measurements at cryogenic temperature.

4.3 Conclusions

In this chapter, an approach based on a standard flux-metric method has been proposed for the characterization of weakly magnetic materials. The drawbacks related to the lack of accuracy for characterizing weakly magnetic materials due to its original conception for high permeability materials are overcome. This

work can be considered as a proof of principle: the feasibility was proved and the principal uncertainty sources were pointed out and analyzed. The overall uncertainty is estimated to be less than a few percents, in repeated measurements under different drift correction assumptions.
The results in terms of uncertainty are not satisfying when μ_r goes below 1.1. Hence, for weakly magnetic materials with a relative magnetic permeability μ_r less than 1.05, a measurement system based on a novel magneto-metric method has been developed and validated. The proposed method identifies the relative magnetic permeability of weakly magnetic materials immersed in a uniform, steady magnetic field. The method is general and could be used with different sample geometries (cube, bar, sphere, etc.) provided that appropriate 2D or 3D FE modeling is used.

Chapter 5

Proposal for monitoring solenoids magnetic axis misalignment

In this Chapter, a novel Hall transducers-based method is proposed for the online monitoring of the single-coil solenoids' magnetic axis. The method relying on measurements of the magnetic flux density at a few points and a simple Taylor expansion as local field model. In particular, the mathematical description of the method, the involved geometrical quantities and a formulation for four transducers per side are presented. However, in the presence of overlapping magnetic fields generated by several coils, the definitions of the magnetic axis and its misalignment, as well as the field model, are significantly more complicated. Hence, a method for monitoring the coils alignment in multi-coil magnets during operations is proposed as well.

5.1 Proposed method for a single solenoid

5.1.1 Basic idea

The proposed method aims at measuring the misalignment of the magnetic axis of a solenoid by using the difference between measurements of magnetic flux density in the actual and aligned cases. The method is summed up in Fig. 5.1. The magnetic flux density is measured by two sets of Hall transducers, placed on two planes orthogonal to the nominal axis at the extremities of the solenoid.

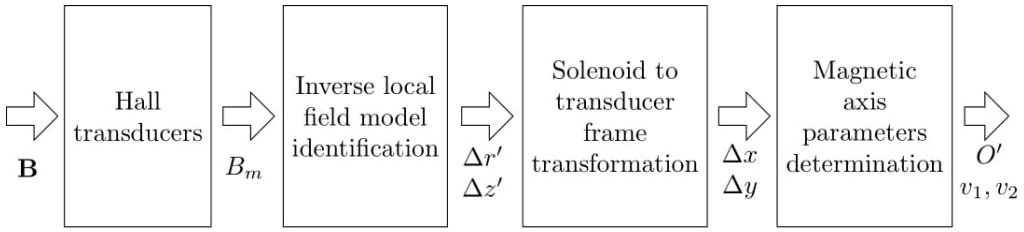

FIGURE 5.1: Main steps of the measurement method.

The measured values $B_m(H_{hk})$ at each position H_{hk} of the transducers are exploited to identify an inverse local field model, defined by linearizing the magnetic flux density around the positions where the transducers would move, due to the axis misalignment. The model allows to compute the displacements $\Delta z'$ and $\Delta r'$ of the transducer coordinates in the solenoid frame from the combination of the magnetic flux densities measured by the transducers. The displacements $\Delta z'$ and $\Delta r'$ are then transformed to the transducer frame and related to the Cartesian displacements $\Delta x, \Delta y$ of the magnetic axis interception with the transducers planes. Finally, these displacements are used to get the parametric equation of the magnetic axis.

5.1.2 Mathematical formulation

The proposed method assumes that:

- From the solenoid point of view, the magnetic flux density preserves its axisymmetry even when the coil is misaligned with respect to the desired position.
- The displacements of the interceptions of the magnetic axis with the planes of the transducers are small with respect to the radial position of the transducers. This assumption will be better clarified within the discussion.
- The Hall transducers are not subject to movements.
- There is no longitudinal shift for the solenoid.

For an axially-symmetric magnet, the magnetic flux density **B** expressed in the cylindrical coordinate system (r, φ, z) is independent from the angle φ. This means that the components of the field, namely B_r, B_z, and B_φ, are all independent of φ. Furthermore, for a solenoid, it is also $B_\varphi = 0$, because **B** is obtained as the curl of a vector potential **A** = $A_\varphi \hat{\varphi}$, which has only a component along $\hat{\varphi}$. Due to the axisymmetry, considering a circle with radius R_0 centered on the solenoid axis and contained in a plane orthogonal to this same axis, the two components of **B** will have a constant magnitude for all the points of the circle. This implies that also the field module B is constant on such a circle.
When the solenoid is in its nominal position (*aligned solenoid*, Fig. 5.2a), a Cartesian reference system with the origin at the center of the solenoid (O), and the z axis along the solenoid magnetic axis can be employed. Let us assume that eight Hall transducers are placed at the coordinates $(-R_0, 0)$, $(+R_0, 0)$, $(0, -R_0)$, $(0, +R_0)$ of the planes π_1 and π_2. Such planes are orthogonal to the z axis, and at positions $z = \pm d/2$, with d the distance between them. The solenoid magnetic axis passes through the points O_1 and O_2, representing the intersection of the planes π_1 and π_2 with the z axis. Meanwhile, the Hall transducers will be subjected to magnetic flux densities with the same amplitude, but with a different orientation, because they are placed at the same distance from the magnetic axis.
When the solenoid is out from its nominal position (*misaligned solenoid*, Fig. 5.2b), the magnetic flux densities **B** measured by the transducers are different not only

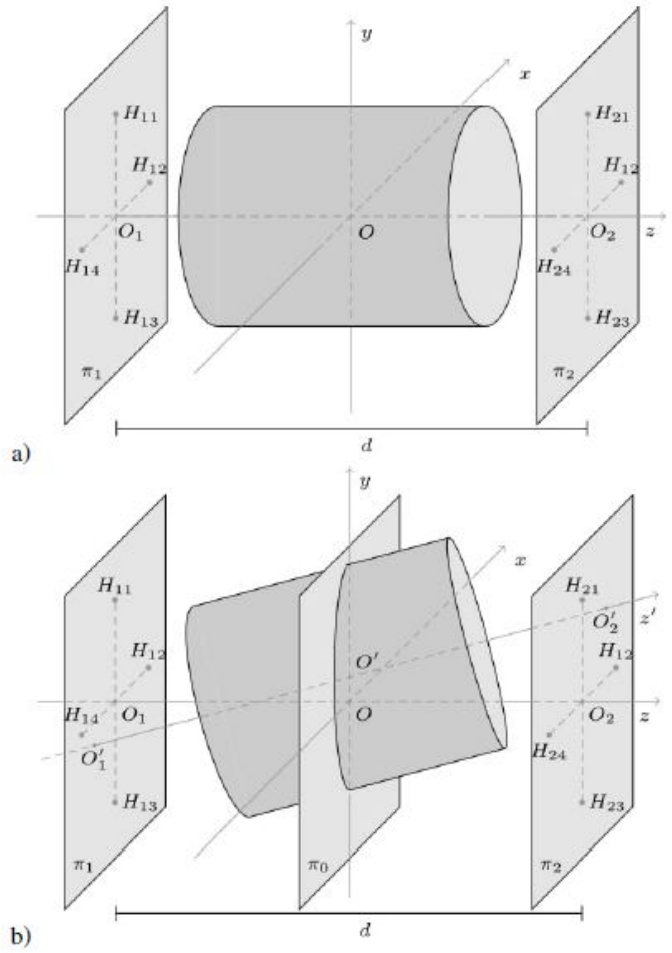

FIGURE 5.2: (a) Aligned solenoid: the magnetic axis matches with the z axis of the transducers reference system (reference axis). (b) Misaligned solenoid: the magnetic axis (z') differs from the reference axis (z), but it can be identified through O_1' and O_2'.

in the orientation but also in the magnitude, owing to the lack of symmetry (the transducers are assumed as not subject to movements). The above-mentioned solenoid reference system is defined as a coordinate system coinciding with the transducers reference when the solenoid is aligned.
In the solenoid reference (Fig. 5.2b), the coordinates are pointed out with an apostrophe ($'$), the origin is the center of the misaligned solenoid (O'), and the magnetic axis corresponds to the z' axis. The magnetic axis is uniquely determined by the coordinates of the solenoid center $O' \equiv (x_{O'}, y_{O'}, z_{O'})$, and by its slope parameters v_1, v_2, v_3:

$$\begin{cases} x = x_{O'} + v_1 t \\ y = y_{O'} + v_2 t \\ z = z_{O'} + v_3 t \end{cases} \tag{5.1}$$

Indicating with O'_1 and O'_2 the intersections of the magnetic axis with the planes π_1 and π_2, respectively, the slope parameters are obtained as:

$$\begin{aligned} v_1 &= x_{O'_2} - x_{O'_1} \\ v_2 &= y_{O'_2} - y_{O'_1} \\ v_3 &= z_{O'_2} - z_{O'_1} \end{aligned} \tag{5.2}$$

Then, according to the assumption of lack of longitudinal shift, the solenoid center is constrained to the plane $\pi_o : z = 0$ (Fig. 5.2b). Therefore, only radial displacements and tilt are considered; thus, the solenoid does not move along the z-axis. In this case, eqs. (5.1) and (5.2) are simplified as:

$$\begin{cases} x = x_{O'} + v_1 t \\ y = y_{O'} + v_2 t \\ z = d \cdot t \end{cases} \qquad \begin{aligned} v_1 &= x_{O'_2} - x_{O'_1} \\ v_2 &= y_{O'_2} - y_{O'_1} \end{aligned} \tag{5.3}$$

Local field model

According to the above assumption of small solenoid axis misalignment, the distance between $O_1 \equiv (0, 0, -d/2)$ and O'_1 and the distance between $O_2 \equiv (0, 0, d/2)$ and O'_2 are small with respect to R_0:

$$\begin{aligned} |O'_1 - O_1| &= \sqrt{x^2_{O'_1} + y^2_{O'_1}} \ll R_0 \\ |O'_2 - O_2| &= \sqrt{x^2_{O'_2} + y^2_{O'_2}} \ll R_0 \end{aligned} \tag{5.4}$$

Under this assumption, the field flux density is approximated with its first-order Taylor expansion around the position H'_{hk}, corresponding to the point where the transducer would move, owing to the misalignment. Then, using such an expansion, the magnetic flux density is assessed in H_{hk} (the position where the transducer lies). Here the subscript "h" identifies the plane where the transducer is located ($h = 1$ for π_1, $h = 2$ for π_2), while "k" identifies the exact transducer of the plane.
The geometry suggests to adopt cylindrical coordinates, and, in the solenoid reference system, the magnetic flux density only depends on the radial (r') and axial (z') coordinates, but not upon the angle (φ'), owing to the axisymmetry. As an example, the case of one of the transducers is highlighted in Fig. 5.3. The transducer lies on the H_{11} position, moving to H'_{11} owing to the misalignment. In this case, the expansion will be around the point H'_{11}, having coordinates $r' = R_0$, $z' = -d/2$ in the solenoid reference system.
In the case of a generic transducer, located at H_{hk}, the magnetic flux density is expanded as:

$$\mathbf{B}(r'_{hk}, z'_{hk}) \approx \mathbf{B}(R_0, z_h) + \left.\frac{\partial \mathbf{B}}{\partial r}\right|_{R_0, z_h} (r'_{hk} - R_0) + \left.\frac{\partial \mathbf{B}}{\partial z}\right|_{R_0, z_h} (z'_{hk} - z_h), \tag{5.5}$$

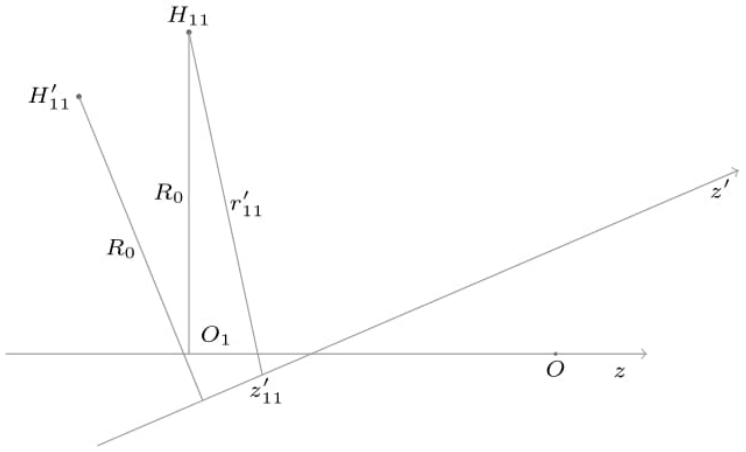

FIGURE 5.3: The position of the transducer H_{11} in both the transducer and the solenoid reference systems. The magnetic flux density is expanded in Taylor series around the position H'_{11}, corresponding to the point where H_{11} would move due to the misalignment.

where, $z_h = \pm d/2$, depending on the side of the solenoid where the transducer is placed. The first member of the equation is the quantity to be measured. In particular, uni-axial Hall transducers can be adopted, positioned along either the radial or the longitudinal direction of the transducer reference system. 1D Hall transducers placed radially are first considered.
A radial transducer measures only the radial component of $\mathbf{B}$ when the solenoid is aligned. Instead, when the solenoid is misaligned, also a contribution from the axial component of the field will appear. The measured value is then composed by the superposition of the projections of $\mathbf{B}_r$ and $\mathbf{B}_z$ onto the radial direction of the transducer reference system. It will then depend on the magnitudes B_r, B_z, and on the angles α and β, between the vectors $\mathbf{B}_r$ and $\mathbf{B}_z$ and the radial direction of the transducer reference system, respectively (Fig. 5.4), again for a single transducer. The measured value is then expressed by:

$$B_m = B_{mr} + B_{mz} = B_r \cos\alpha + B_z \sin\beta \tag{5.6}$$

where the projections assume negative values when directed towards the z-axis and vice versa. As an example, in the case of Fig. 5.4, B_{mz} has a positive value, while B_{mr} a negative value.
Under the assumption of small misalignment, eq. (5.6) can be simplified by assuming $\cos\alpha \approx 1$. Then, the sign of B_{mr} and B_r coincide. Instead, the sign of B_{mz} coincides with the sign of $\sin\beta$ because B_z is always positive. Here, B_r and B_z can be expressed by Taylor expansion, as shown in (5.5). Such an expansion depends on the coordinates (r'_{hk}, z'_{hk}) of the transducer positions in the solenoid reference system. The derivation of the geometrical quantities as well as of $\sin\beta$ for the different transducers is reported in the next subsection.

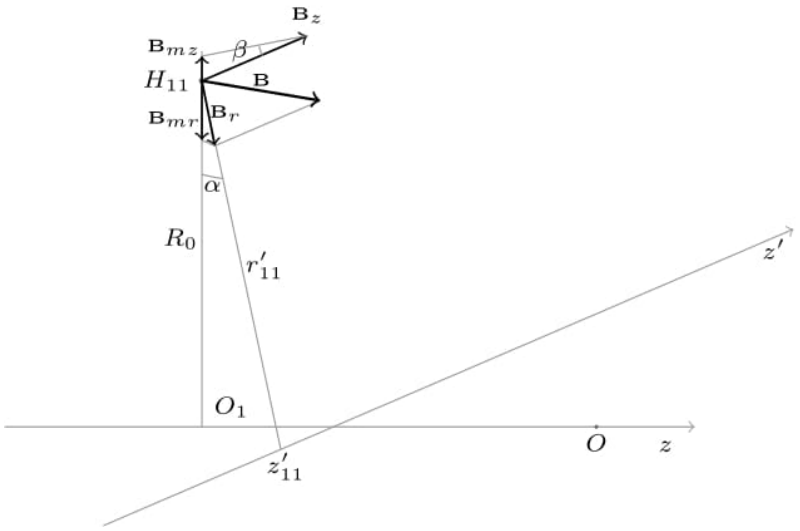

FIGURE 5.4: $\mathbf{B}_r$ and $\mathbf{B}_z$ orientation with respect to the radial direction on which the considered transducer is placed.

Geometrical quantities

The coordinates (r'_{hk}, z'_{hk}) of H_{hk} in the solenoid reference system (Fig. 5.5) can be expressed in terms of the points H_{hk}, I_{hk}, and O'_1 (or O'_2), in the transducers reference. H_{hk} is the point where a transducer is located, I_{hk} its projection on the magnetic axis and O'_1 the intersection between the magnetic axis and the plane π_1 considered in the figure.

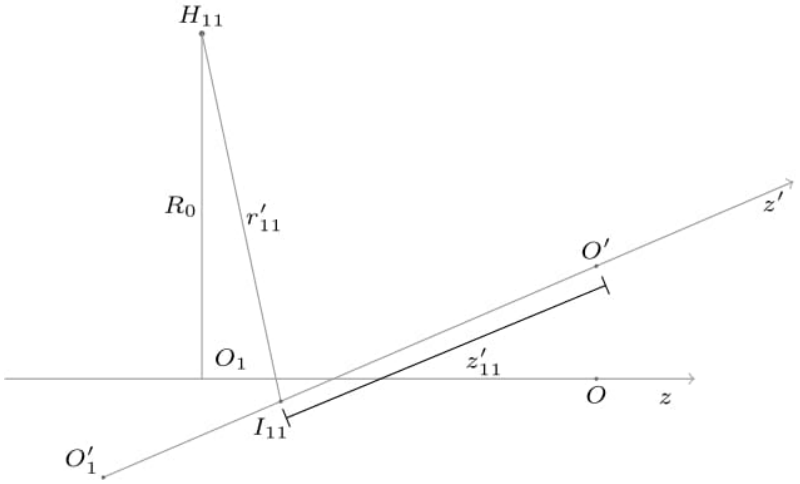

FIGURE 5.5: Coordinates (r'_{11}, z'_{11}) of the transducer position in the solenoid reference system.

r'_{hk} is the distance of the transducer position from the solenoid axis, namely the distance between H_{hk} and $I_{hk} \equiv (x_{I_{hk}}, y_{I_{hk}}, z_{I_{hk}})$. For example, considering $H_{11} \equiv$

$(0, +R_0, -d/2)$, eq. (5.7) holds under the hypothesis of small axis misalignment:

$$\begin{aligned} r'_{11} =& \sqrt{(x_{I_{11}})^2 + (R_0 - y_{I_{11}})^2 + \left(-\frac{d}{2} - z_{I_{11}}\right)^2} = R_0 \sqrt{\left(\frac{x_{I_{11}}}{R_0}\right)^2 + \left(\frac{R_0 - y_{I_{11}}}{R_0}\right)^2} + \\ &+ R_0 \sqrt{\left(\frac{-d/2 - z_{I_{11}}}{R_0}\right)^2} \approx R_0 \sqrt{\left(\frac{R_0 - y_{I_{11}}}{R_0}\right)^2} = R_0 - y_{I_{11}} \end{aligned} \tag{5.7}$$

Analogously, in the case of $H_{13} \equiv (0, -R_0, -d/2)$:

$$r_{13}{}' \approx R_0 \sqrt{\left(\frac{-R_0 - y_{I_{13}}}{R_0}\right)^2} = R_0 + y_{I_{13}} \tag{5.8}$$

The points I_{hk} can be described with the parametrization of the magnetic axis introduced in eq. (5.3). The equation of the z' axis must be combined with the equation describing a plane orthogonal to z' and passing through the transducer $H_{hk} \equiv (x_{H_{hk}}, y_{H_{hk}}, z_{H_{hk}})$, namely the expression (5.9).

$$v_1(x - x_{H_{hk}}) + v_2(y - y_{H_{hk}}) + d(z - z_{H_{hk}}) = 0 \tag{5.9}$$

It results that I_{hk} has the following parametric expression:

$$\begin{cases} x_{I_{hk}} = x_{O'} + t_{I_{hk}} v_1 \\ y_{I_{hk}} = y_{O'} + t_{I_{hk}} v_2 \\ z_{I_{hk}} = t_{I_{hk}} d \\ t_{I_{hk}} = \dfrac{v_1(x_{H_{hk}} - x_{O'}) + v_2(y_{H_{hk}} - y_{O'}) + d z_{H_{hk}}}{v_1^2 + v_2^2 + d^2} = \\ \qquad \approx \dfrac{v_1(x_{H_{hk}} - x_{O'}) + v_2(y_{H_{hk}} - y_{O'}) + d z_{H_{hk}}}{d^2} \end{cases} \tag{5.10}$$

z'_{hk} is instead the distance of I_{hk} from the solenoid center. Actually, in the Taylor expansion, the term $z'_{hk} - z_h$ is needed, and this can be obtained from the third equation of (5.10), by considering that for z_1 and z_2, is $t = -1/2$ and $t = 1/2$, respectively. Therefore, the following equations apply:

$$\begin{aligned} z'_{1k} - z_1 &= \left(t_{I_{1k}} + \frac{1}{2}\right) d \\ z'_{2k} - z_2 &= \left(t_{I_{2k}} - \frac{1}{2}\right) d \end{aligned} \tag{5.11}$$

In conclusion, the expressions of B_r and B_z can be written with the Taylor expansion thanks to the previous geometrical considerations. As an example, for the

transducers in positions H_{11} and H_{13} it results that:

$$\begin{aligned} B_r(H_{11}) &\approx B_r\left(R_0, -\frac{d}{2}\right) - \left.\frac{\partial B_r}{\partial r}\right|_{R_0,-\frac{d}{2}} (y_{O'} + t_{I_{11}} v_2) + \left.\frac{\partial B_r}{\partial z}\right|_{R_0,-\frac{d}{2}} \left(t_{I_{11}} + \frac{1}{2}\right) d \\ B_r(H_{13}) &\approx B_r\left(R_0, -\frac{d}{2}\right) + \left.\frac{\partial B_r}{\partial r}\right|_{R_0,-\frac{d}{2}} (y_{O'} + t_{I_{13}} v_2) + \left.\frac{\partial B_r}{\partial z}\right|_{R_0,-\frac{d}{2}} \left(t_{I_{13}} + \frac{1}{2}\right) d \end{aligned} \tag{5.12}$$

where:

$$\begin{aligned} t_{I_{11}} &= \frac{v_1(-x_{O'}) + v_2(+R_0 - y_{O'}) + d(-d/2)}{d^2} \approx \frac{v_2(+R_0 - y_{O'})}{d^2} - \frac{1}{2} \\ t_{I_{13}} &= \frac{v_1(-x_{O'}) + v_2(-R_0 - y_{O'}) + d(-d/2)}{d^2} \approx \frac{v_2(-R_0 - y_{O'})}{d^2} - \frac{1}{2} \end{aligned} \tag{5.13}$$

The last term to be determined is $\sin\beta$. For transducers lying on a straight line parallel to the y-axis, such as H_{11} and H_{13}, β is the elevation angle of the z'-axis from the xz plane:

$$\begin{aligned} \sin\beta_{11} &= \frac{y_{O'_2} - y_{O'_1}}{z_{O'_2} - z_{O'_1}} \approx +\frac{v_2}{d} \\ \sin\beta_{13} &= -\sin\beta_{11} \approx -\frac{v_2}{d} \end{aligned} \tag{5.14}$$

Similarly, for transducers lying on a straight line parallel to x-axis, such as H_{12} and H_{14}, β_{12} is the azimuth angle z'-axis from the yz plane, and $\beta_{14} = -\beta_{12}$. In the latter case, the following equations apply:

$$\begin{aligned} \sin\beta_{12} &= \frac{x_{O'_2} - x_{O'_1}}{z_{O'_2} - z_{O'_1}} \approx +\frac{v_1}{d} \\ \sin\beta_{14} &= -\sin\beta_{12} \approx -\frac{v_1}{d} \end{aligned} \tag{5.15}$$

Four transducers per side

Let's consider the case of four uniaxial Hall transducers per solenoid side, placed in the following points:

$$\begin{array}{ll} H_{11} \equiv (0, +R_0, -d/2) & H_{21} \equiv (0, +R_0, +d/2) \\ H_{12} \equiv (+R_0, 0, -d/2) & H_{22} \equiv (+R_0, 0, +d/2) \\ H_{13} \equiv (0, -R_0, -d/2) & H_{23} \equiv (0, -R_0, +d/2) \\ H_{14} \equiv (-R_0, 0, -d/2) & H_{24} \equiv (-R_0, 0, +d/2) \end{array}$$

In such positions, some symmetries of the magnetic field can be exploited. In the aligned case, indeed, both the radial and the axial components of the magnetic flux density have the same magnitude in the eight considered positions. In

particular, the following relations apply:

$$\begin{aligned}
&B_r(H_{2k}) = -B_r(H_{1k}) = B_{r0} \qquad B_z(H_{2k}) = +B_z(H_{1k}) = B_{z0} \\
&\tfrac{\partial B_r}{\partial r}\big|_{R_0,+\frac{d}{2}} = -\tfrac{\partial B_r}{\partial r}\big|_{R_0,-\frac{d}{2}} = \tfrac{\partial B_r}{\partial r}\big|_0 \quad \tfrac{\partial B_z}{\partial r}\big|_{R_0,+\frac{d}{2}} = +\tfrac{\partial B_z}{\partial r}\big|_{R_0,-\frac{d}{2}} = \tfrac{\partial B_z}{\partial r}\big|_0 \\
&\tfrac{\partial B_r}{\partial z}\big|_{R_0,+\frac{d}{2}} = +\tfrac{\partial B_r}{\partial z}\big|_{R_0,-\frac{d}{2}} = \tfrac{\partial B_r}{\partial z}\big|_0 \quad \tfrac{\partial B_z}{\partial z}\big|_{R_0,+\frac{d}{2}} = -\tfrac{\partial B_z}{\partial z}\big|_{R_0,-\frac{d}{2}} = \tfrac{\partial B_z}{\partial z}\big|_0
\end{aligned} \tag{5.16}$$

The magnetic axis misalignment is sensed by taking into account the difference in the measurements of transducers lying on the same plane and on the same axis (x or y). As an example, the equation obtained by subtracting the values measured by the couple (H_{13}, H_{11}) is shown. Similar equations are then valid for the couples (H_{14}, H_{12}), (H_{23}, H_{21}), and (H_{24}, H_{22}).

$$\begin{aligned}
B_m(H_{13}) - B_m(H_{11}) \approx [B_r(H_{13}) - B_r(H_{11})] - \frac{v_2}{d}\left[B_z(H_{13}) + B_z(H_{11})\right] = \\
= -\left.\frac{\partial B_r}{\partial r}\right|_0 \left[2y_{O'} + (t_{I_{13}} + t_{I_{11}})\, v_2\right] + \left.\frac{\partial B_r}{\partial z}\right|_0 (t_{I_{13}} - t_{I_{11}})d + \\
- \frac{v_2}{d}\left[2B_{z0} + \left.\frac{\partial B_z}{\partial r}\right|_0 (t_{I_{13}} - t_{I_{11}})v_2 - \left.\frac{\partial B_z}{\partial z}\right|_0 (t_{I_{13}} + t_{I_{11}} + 1)d\right]
\end{aligned} \tag{5.17}$$

Substituting (5.13) in (5.17) and neglecting the quadratic terms of v_2:

$$\begin{aligned}
B_m(H_{13}) - B_m(H_{11}) \approx -\left.\frac{\partial B_r}{\partial r}\right|_0 \left[2y_{O'}\left(1 - \frac{v_2^2}{d^2}\right) - v_2\right] - 2\left.\frac{\partial B_r}{\partial z}\right|_0 \frac{v_2}{d} R_0 + \\
- \frac{v_2}{d}\left[2B_{z0} - 2\left.\frac{\partial B_z}{\partial r}\right|_0 \frac{v_2^2}{d^2} R_0 - 2\left.\frac{\partial B_z}{\partial z}\right|_0 \frac{v_2}{d} y_{O'}\right] \approx \\
\approx -2\left.\frac{\partial B_r}{\partial r}\right|_0 \left(y_{O'} - \frac{v_2}{2}\right) - 2\frac{R_0}{d}\left.\frac{\partial B_r}{\partial z}\right|_0 v_2 - 2\frac{v_2}{d} B_{z0}
\end{aligned} \tag{5.18}$$

Repeating the same reasoning for the other transducers couples, the following system of equations is obtained:

$$\begin{aligned}
B_m(H_{13}) - B_m(H_{11}) &= -2\left.\frac{\partial B_r}{\partial r}\right|_0 \left(y_{O'} - \frac{v_2}{2}\right) - 2\frac{R_0}{d}\left.\frac{\partial B_r}{\partial z}\right|_0 v_2 - 2\frac{v_2}{d} B_{z0} \\
B_m(H_{14}) - B_m(H_{12}) &= -2\left.\frac{\partial B_r}{\partial r}\right|_0 \left(x_{O'} - \frac{v_1}{2}\right) - 2\frac{R_0}{d}\left.\frac{\partial B_r}{\partial z}\right|_0 v_1 - 2\frac{v_1}{d} B_{z0} \\
B_m(H_{23}) - B_m(H_{21}) &= +2\left.\frac{\partial B_r}{\partial r}\right|_0 \left(y_{O'} + \frac{v_2}{2}\right) - 2\frac{R_0}{d}\left.\frac{\partial B_r}{\partial z}\right|_0 v_2 - 2\frac{v_2}{d} B_{z0} \\
B_m(H_{24}) - B_m(H_{22}) &= +2\left.\frac{\partial B_r}{\partial r}\right|_0 \left(x_{O'} + \frac{v_1}{2}\right) - 2\frac{R_0}{d}\left.\frac{\partial B_r}{\partial z}\right|_0 v_1 - 2\frac{v_1}{d} B_{z0}
\end{aligned} \tag{5.19}$$

This linear system can be easily solved to obtain $x_{O'}$, $y_{O'}$, v_1, and v_2:

$$\begin{aligned}
x_{o'} &= \frac{[B_m(H_{24}) - B_m(H_{22})] - [B_m(H_{14}) - B_m(H_{12})]}{4\ \frac{\partial B_r}{\partial r}\Big|_0} \\
y_{o'} &= \frac{[B_m(H_{23}) - B_m(H_{21})] - [B_m(H_{13}) - B_m(H_{11})]}{4\ \frac{\partial B_r}{\partial r}\Big|_0} \\
v_1 &= \frac{[B_m(H_{24}) - B_m(H_{22})] + [B_m(H_{14}) - B_m(H_{12})]}{2\left(\frac{\partial B_r}{\partial r}\Big|_0 - 2\frac{R_0}{d}\ \frac{\partial B_r}{\partial z}\Big|_0 - 2\frac{B_{z0}}{d}\right)} \\
v_2 &= \frac{[B_m(H_{23}) - B_m(H_{21})] + [B_m(H_{13}) - B_m(H_{11})]}{2\left(\frac{\partial B_r}{\partial r}\Big|_0 - 2\frac{R_0}{d}\ \frac{\partial B_r}{\partial z}\Big|_0 - 2\frac{B_{z0}}{d}\right)}
\end{aligned} \tag{5.20}$$

Similar considerations can be done for transducers placed along the axial direction, leading to a slightly different set of equations:

$$\begin{aligned}
B_m(H_{13}) - B_m(H_{11}) &= 2\ \frac{\partial B_z}{\partial r}\bigg|_0 \left(y_{O'} - \frac{v_2}{2}\right) + 2\frac{R_0}{d}\ \frac{\partial B_z}{\partial z}\bigg|_0 v_2 + 2\frac{B_{r0}}{d}v_2 \\
B_m(H_{14}) - B_m(H_{12}) &= 2\ \frac{\partial B_z}{\partial r}\bigg|_0 \left(x_{O'} - \frac{v_1}{2}\right) + 2\frac{R_0}{d}\ \frac{\partial B_z}{\partial z}\bigg|_0 v_1 + 2\frac{B_{r0}}{d}v_1 \\
B_m(H_{23}) - B_m(H_{21}) &= 2\ \frac{\partial B_z}{\partial r}\bigg|_0 \left(y_{O'} + \frac{v_2}{2}\right) - 2\frac{R_0}{d}\ \frac{\partial B_z}{\partial z}\bigg|_0 v_2 - 2\frac{B_{r0}}{d}v_2 \\
B_m(H_{24}) - B_m(H_{22}) &= 2\ \frac{\partial B_z}{\partial r}\bigg|_0 \left(x_{O'} + \frac{v_1}{2}\right) - 2\frac{R_0}{d}\ \frac{\partial B_z}{\partial z}\bigg|_0 v_1 - 2\frac{B_{r0}}{d}v_1
\end{aligned} \tag{5.21}$$

Thus, it can be easily derived that:

$$\begin{aligned}
x_{O'} &= \frac{[B_m(H_{24}) - B_m(H_{22})] + [B_m(H_{14}) - B_m(H_{12})]}{4\ \frac{\partial B_z}{\partial r}\Big|_0} \\
y_{O'} &= \frac{[B_m(H_{23}) - B_m(H_{21})] + [B_m(H_{13}) - B_m(H_{11})]}{4\ \frac{\partial B_z}{\partial r}\Big|_0} \\
v_1 &= \frac{[B_m(H_{14}) - B_m(H_{12})] - [B_m(H_{24}) - B_m(H_{22})]}{2\left(2\frac{R_0}{d}\ \frac{\partial B_z}{\partial z}\Big|_0 - \frac{\partial B_z}{\partial r}\Big|_0 - 2\frac{B_{r0}}{d}\right)} \\
v_2 &= \frac{[B_m(H_{13}) - B_m(H_{11})] - [B_m(H_{23}) - B_m(H_{21})]}{2\left(2\frac{R_0}{d}\ \frac{\partial B_z}{\partial z}\Big|_0 - \frac{\partial B_z}{\partial r}\Big|_0 - 2\frac{B_{r0}}{d}\right)}
\end{aligned} \tag{5.22}$$

A further realization of the method can be obtained by only three transducers per solenoid side in order to minimize the system complexity. However, a more complex analytical model, and higher uncertainty, both deriving from the lack of symmetry introduced removing one of the transducers per side, are involved.

5.2 Proposed method for multi-coils solenoids

In the presence of overlapping magnetic fields generated by several coils, the definitions of the magnetic axis and its misalignment, as well as the field model, are

significantly more complicated. In this Section, a method is proposed, allowing to monitor the coils alignment in multi-coil magnets, during the machine operation.

5.2.1 Basic idea

For a focusing magnet, the magnetic axis can be defined as *the path where the integral over the transversal field component is minimum* [117]. For a single cylindrical coil, assuming that the magnetic field is axially symmetric, the magnetic axis is a straight line and coincides with the symmetry axis of the magnetic field. In particular, on the magnetic axis of the coil, the transversal field component (B_r) is null [42], and the particles moving precisely along this axis are not deflected. In practice, particles must be close to the magnetic axis to be significantly focused [84].
For an actual multi-coil magnet, the same definition of the magnetic axis is no longer trivial, and the equation of the magnetic axis in a proper reference frame cannot be found by applying the method proposed in the previous section. Even by assuming the magnetic field of each coil as axially symmetric, the actual misalignments of such fields make the overall magnetic field not axially symmetric. Therefore, in this case, the magnetic axis can be approximated with a polygonal chain, composed by as many segments as the number of the coils, where each segment is part of the magnetic axis of the corresponding coil.
Thus, by monitoring the magnetic axis, we mean deriving the polygonal chain and thus approximating the overall magnetic axis in a given reference frame. To this aim, the method for a single coil previously proposed is to be extended by relying on the axisymmetry of each coil. The basic idea is that the field measured through Hall transducers traces back to the misalignment thanks to a local field model. In particular, the model links some measurements suitably located out from the solenoid air gaps to some geometrical quantities identifying the orientation of the magnetic axis.

5.2.2 Mathematical formulation

In this section, an actual multi-coil magnet, where the magnetic fields of the different coils are misaligned, is considered. Assuming that the magnetic field of each coil is axially-symmetric, a piecewise axial symmetry can be assumed for the magnet as a whole. Thus, the overall magnetic axis can be represented by a polygonal chain composed of the axes of each coil. In particular, excepting for the first and last coils, a segment of the axis is considered, composed by (i) half of the distance from the left adjacent coil, and half the distance from the right adjacent coil. For the first and last coils, instead, only a half line is considered, because they have only one adjacent coil. Fig. 5.6 depicts the example of a multi-coil magnet with 4 coils, by highlighting the polygonal chain composed of the individual magnetic axes of the coils.
Such a magnetic axis can be determined by measuring the misalignment of the field of each coil, similarly to a single-coil solenoid. The assumptions underlying

the method are extensively treated in the previous section and are only summarized in the following. Regarding the field **B**, in a cylindrical coordinate system (r, φ, z), the component B_φ is assumed as null. For the generic i-th coil, a reference axis z_i is considered with the origin at the aligned coil center. Two parallel planes π_h and π_{h+1} (Fig. 5.7), with mutual distance d, are chosen at $z_i = -d/2$ and $z_i = +d/2$.
Hall transducers, assumed as punctiform, are placed in these planes, at the same radial distance R_0 from the reference axis z_i. Owing to the field symmetries, all the transducers will measure the same field magnitude, when the magnetic axis is aligned with the reference axis and different magnitudes when the magnetic axis is misaligned. The transducer locations are called H_{hk}, where h identifies the plane, and k the transducer within the plane. They define a Cartesian coordinate system $x_i y_i z_i$ (*transducers reference*), where the $x_i y_i$ plane is orthogonal to the z_i axis. The transducers reference of each coil differs from another just for a longitudinal shift. The axis misalignment can be derived if:

- the displacements of the interceptions of the magnetic axis with the planes of the transducers are small with respect to the radial position (R_0) of the transducers (*small misalignment*);
- the Hall transducers are not subject to movements, namely they are fiducial markers for the axis measurement (*fixed transducers*);
- the magnet can be subject to transverse shifts, as well as rotations, but not to longitudinal shift (*longitudinally fixed magnet*).

Extending the reasoning to multiple coils, a set of Hall transducers at both sides of each coil is placed. Differently from the single-coil case, however, the field measured by the transducers depends also on the magnetic flux density irradiated by the other coils. The method proposed here assumes that the overall magnetic field can be modeled as the superposition of the fields of each coil. Fig. 5.7 shows the general case of one of the coils lying in the middle of the solenoid, with adjacent transducers planes placed as briefly recalled above.
The parametric expression of the segment of the magnetic axis corresponding to

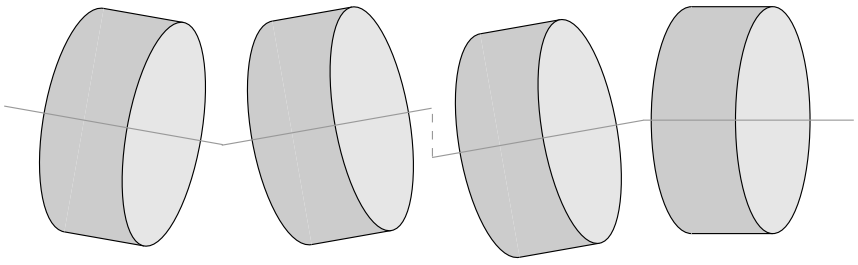

FIGURE 5.6: Polygonal chain built from the magnetic axes of coils that can move independently, but assumed as axially symmetric.

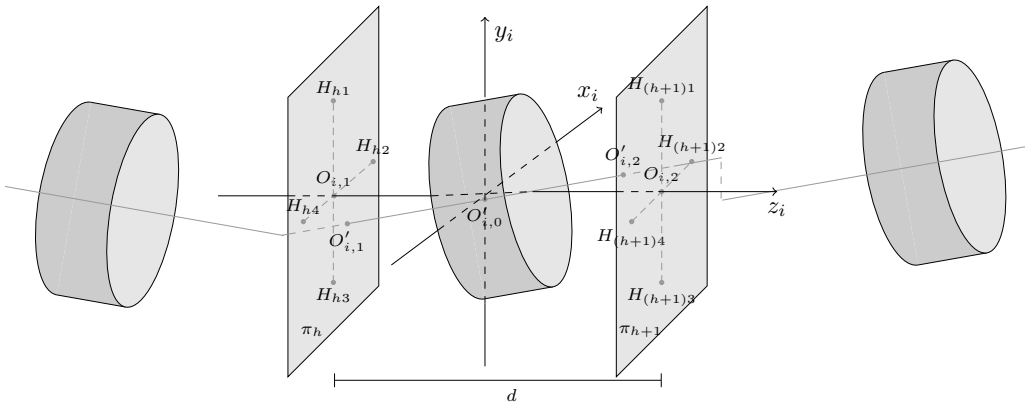

FIGURE 5.7: Hall transducers placed at the planes h and h+1 adjacent to the coil i.

the i-th coil is

$$\begin{cases} x_i = x_{O'_{0,i}} + tv_{x,i} \\ y_i = y_{O'_{0,i}} + tv_{y,i} \\ z_i = td \end{cases} \tag{5.23}$$

where $O'_{0,i} = \left(x_{O'_{0,i}}, y_{O'_{0,i}}, 0\right)$ is the center of the misaligned coil i, while $v_{x,i}$ and $v_{y,i}$ are the slope parameters associated to the axis. The expression of the field measured by a transducer H_{hk} is obtained by overlapping the fields irradiated by all the N coils. If uniaxial Hall transducers are placed radially, the measured values are a combination of the radial and axial magnetic field components projections on the radial direction. When the coils misalignment is small, it results that

$$B_m(H_{hk}) \approx \sum_{i=1}^{N} [B_{r,i}(H_{hk}) + \sin\beta_{hk,i} B_{z,i}(H_{hk})]. \tag{5.24}$$

In a generic plane h, considering the couples of transducers H_{h3}-H_{h1} and H_{h4}-H_{h2}, respectively at $x = 0$ and $y = 0$, the expressions of interest are

$$\begin{aligned} B_m(H_{h3}) - B_m(H_{h1}) &= \sum_{i=1}^{N} \left\{ [B_{r,i}(H_{h3}) - B_{r,i}(H_{h1})] - \frac{v_{y,i}}{d} [B_{z,i}(H_{h3}) + B_{z,i}(H_{h1})] \right\} \\ B_m(H_{h4}) - B_m(H_{h2}) &= \sum_{i=1}^{N} \left\{ [B_{r,i}(H_{h4}) - B_{r,i}(H_{h2})] - \frac{v_{x,i}}{d} [B_{z,i}(H_{h4}) + B_{z,i}(H_{h2})] \right\} \end{aligned} \tag{5.25}$$

where the ratios between a slope parameter and d are a first-order approximation of $sin\beta_{hk,i}$. The discussion can be conducted exclusively for the couple H_{h3}-H_{h1}, because for H_{h4}-H_{h2} it is enough to exchange the role of y_i with x_i. Reasoning on the method generalization, one discovers that the expressions are to distinguish for odd and even h: in fact, an odd value for h means that a plane on the left of the considered coil is taken into account, while for even values of h the plane is on the right.

The radial and longitudinal field components in eq. (5.25) are modeled with a Taylor expansion. In particular, the method employs a first order local field model for the radial field components, as shown in eq. (5.26):

$$B_{r,i}(r'_{hk}, z'_{hk}) \approx B_{r,i}(R_0, z_h) + \left.\frac{\partial B_{r,i}}{\partial r}\right|_{R_0,z_h} (r'_{hk} - R_0) + \left.\frac{\partial B_{r,i}}{\partial z}\right|_{R_0,z_h} (z'_{hk} - z_h) \quad (5.26)$$

It can be demonstrated that the only term of the $B_{z,i}$ expansion that does not lead to a second-order term for $v_{y,i}$ in expression (5.25) is the field value at the initial point of the expansion, namely $B_z(R_0, z_h)$. For each coil, the starting point for the Taylor expansion is considered in the respective transducer reference. The equations of interest are

for odd h:

$$\begin{aligned} B_m(H_{h3}) - B_m(H_{h1}) = \sum_{i=1}^{N} \Bigg\{ & 2 \left.\frac{\partial B_r}{\partial r}\right|_{-\frac{d}{2}+\left(\frac{h+1}{2}-i\right)D} y_{O'_{0,i}} + \\ & + \Bigg[\left.\frac{\partial B_r}{\partial r}\right|_{-\frac{d}{2}+\left(\frac{h+1}{2}-i\right)D} \left(-1 + (h+1-2i)\frac{D}{d}\right) + \\ & - 2\frac{R_0}{d} \left.\frac{\partial B_r}{\partial z}\right|_{-\frac{d}{2}+\left(\frac{h+1}{2}-i\right)D} - 2\frac{B_z|_{-\frac{d}{2}+\left(\frac{h+1}{2}-i\right)D}}{d} \Bigg] v_{y,i} \Bigg\} \end{aligned} \quad (5.27)$$

for even h:

$$\begin{aligned} B_m(H_{h3}) - B_m(H_{h1}) = \sum_{i=1}^{N} \Bigg\{ & 2 \left.\frac{\partial B_r}{\partial r}\right|_{+\frac{d}{2}+\left(\frac{h}{2}-i\right)D} y_{O'_{0,i}} + \\ & + \Bigg[\left.\frac{\partial B_r}{\partial r}\right|_{+\frac{d}{2}+\left(\frac{h}{2}-i\right)D} \left(+1 + (h-2i)\frac{D}{d}\right) + \\ & - 2\frac{R_0}{d} \left.\frac{\partial B_r}{\partial z}\right|_{+\frac{d}{2}+\left(\frac{h}{2}-i\right)D} - 2\frac{B_z|_{+\frac{d}{2}+\left(\frac{h}{2}-i\right)D}}{d} \Bigg] v_{y,i} \Bigg\} \end{aligned} \quad (5.28)$$

where D is the distance between two adjacent coils centers when the coils are aligned. By writing the equations (5.27) and (5.28) for $h = 1, 2, ..., N$, and the corresponding ones for the couples of transducers (H_{h4}, H_{h2}), a linear system of 4N equations in the 4N unknowns $x_{0,i}$, $y_{0,i}$, $v_{x,i}$, and $v_{y,i}$ $(i = 1, 2, ..., N)$ is obtained. The expression for the desired quantities is too cumbersome to write explicitly, while it is easier to be solved numerically.

5.3 Conclusions

In this chapter, a novel method for monitoring in real time the magnetic axis misalignment in single-coil magnets has been presented. The method requires only a few measurements of the magnetic field at fixed positions inside the magnet aperture, and thus overcomes the main drawback of sturdy moving mechanics of other Hall sensor-based methods. Conversely to state-of-the-art axis determination, the proposed method can be applied also during magnet operations, when the axis region and almost the whole remaining magnet aperture are not accessible. Moreover, only a few measurements of the magnetic field at fixed positions inside the magnet aperture are required: thus a slow process such as the mapping of the whole aperture of a magnet employing moving stages is not necessary.
Furthermore, a method for monitoring the coils alignment in multi-coil magnets has been proposed. This proposal extends the previous method for measuring the magnetic axis of a single-coil solenoid during its operation. In both the cases, it was shown that a set of Hall transducers and a simple first-order Taylor expansion as a local field model are sufficient. In particular, for the multi-coil case, the magnetic field as a whole has been assumed as the superposition of the fields irradiated by the single coils. Simulations employing a proper field model were described to place transducers to minimize the measurement uncertainty.

Chapter 6

Validation of the proposed method for soft magnetic materials

In this chapter, the enhanced flux-metric method described in Chapter 3 has been employed for characterizing two materials, namely, ARMCO for magnet yokes and CRIOPHY for magnetic shields. In particular, the magnetic characterization of ARMCO® Pure Iron for the magnetic yokes of the new HL-LHC superconducting dipoles and quadrupoles, is illustrated. The magnetic properties at room and cryogenic temperatures are shown, empathizing different aspects concerning the operational conditions. Moreover, a comprehensive magnetic characterization of the high-μ_r alloy, CRYOPHY, to be used for shielding cryogenic applications, is presented. In particular, the effects of the temperature and the mechanical strain on the magnetic properties are investigated. The attenuation test inside the magnetic shields is, also, reported for the Crab cavity cryomodule magnetic shield prototype at CERN. Finally, the importance of magnetic material measurements in the framework of the design of magnets for particle accelerator is discussed.

6.1 Case study I: Characterization of a material for magnet yoke

The construction of the superconducting magnets for the High-Luminosity upgrade of the LHC accelerator at CERN has resulted in demands for 1800 tonnes of ferromagnetic laminations for the magnet iron yokes. In this section, the magnetic properties of the selected steel, ARMCO® Pure Iron, have been measured, within annealing treatment sequences from 750 °C to 850 °C, at operation temperatures of 4 K to 300 K. The dependency on the operation temperature was shown by testing the material at the cryogenic temperature of roughly 4 K, 77 K and at room temperature. Tests performed before and after the application of a mechanical stress have also been studied to validate the production process. The behavior of the material for much higher magnetic fields (8.6 to 11 T according to the field distribution in HL-LHC magnets) has been studied. Finally, the affect of the B-H curve variations on the performance of the magnets has been studied with numerical field simulations.

6.1.1 Material and test specimen

For the production of the iron yoke laminations, the ARMCO® Pure Iron is the steel grade that better corresponds to the CERN requirements as defined in the technical specification IT4009 [132]. ARMCO® Pure Iron is low carbon steel that undergoes purification during melting by using special refining techniques. After solidification, it has a particularly homogeneous composition with regard to the impurity distribution. In the grade 4 version, ARMCO® Pure Iron presents a maximum carbon content lower than 0.003% and very low values of oxygen, sulfur, nitrogen and cobalt. Due to the low carbon content, the microstructure consists of 100% ferrite. Although, with existing technology, the carbon content has never exceeded 0.0023% with an average value of 0.0013% in the last years production.

The ARMCO® Pure Iron has a minimum Fe content of 99.85 weight%, hot rolled at 800 °C, cooled in air (not water cooled in line), with pickling and oiling of the metal sheets for rust protection. It is a non-ageing type, delivered in sheets, which are 4000 mm long and 750 mm wide. They are conditioned in 4-ton packs for the transport and storage. The sheets thickness is 5.8 mm, which is a standard value for the yoke laminations used for the construction of the LHC Main Bending and Quadrupole Magnets. Due to its microstructure, the ARMCO® Pure Iron has only marginal mechanical properties. Although it was selected to match with the magnetic specification, the grade presents adequate mechanical characteristics (not too brittle at low temperature). For the steel sheets, CERN accepts material with a grain size ASTM lower than 6, corresponding to an ultimate tensile strength around 300 MPa and a yield strength around 180 MPa.

Test samples have been machined out of the coils during the sheet cutting process. In order not to alter the magnetic properties of the steel, these samples have been cut at very low speed. A water jet cutting method, with abrasive powder, combined with a slow machining to obtain the required tolerances has been employed. Punching of the rings is not permitted. The samples were obtained as rings. The results presented here refer to the two groups of samples listed in Tab. 6.1. The former consists of 5 samples annealed as summarized in Tab. 6.1 and tested to investigate the role of annealing and cryogenic temperatures. The latter consists of three samples with the same annealing tested before and after the application of a cold work to investigate its role on the magnetic properties. AK steel provides the heat treatment guidelines for the annealing. In detail, the annealing parameters are: heating rate of 2-4 °C/min, a hold temperature of 820 °C for 60 min, with an additional 15 minutes for each 0.5 cm thickness over 2.5 cm and a cooling rate of 2-4 °C/min until the parts are below 550-600 °C. The samples were tested under quasi-static conditions. The normal magnetization curve, the hysteresis loop, and the relative magnetic permeability curve have been measured utilizing the proposed flux-metric based measurement system for soft magnetic materials.

TABLE 6.1: Summary of the thermal treatment on the samples

Group #	Reference	Weight [g]	Annealing time [°C]	Annealing time [h]
1	A	812	Not Annealed	0
1	B	815	750	1
1	C	816	750	5
1	D	816	850	1
1	E	816	850	5
2	A25112-4	256	750	1
2	A25112-3	257	750	1
2	A25114-4	256	750	1

6.1.2 Experimental results

Effects of the annealing on magnetic properties

The first five samples of ARMCO pure iron summarized in Tab. 6.1 have been magnetically tested at CERN to asses their magnetic properties. The tests aimed at obtaining the B-H curve for all the samples, to check (i) the magnetic properties of the material for different heating annealing, and (ii) that the magnetic properties of the material are suitable for the LHC magnet construction requirements (IT4009 specification). All the samples were tested at room temperature.

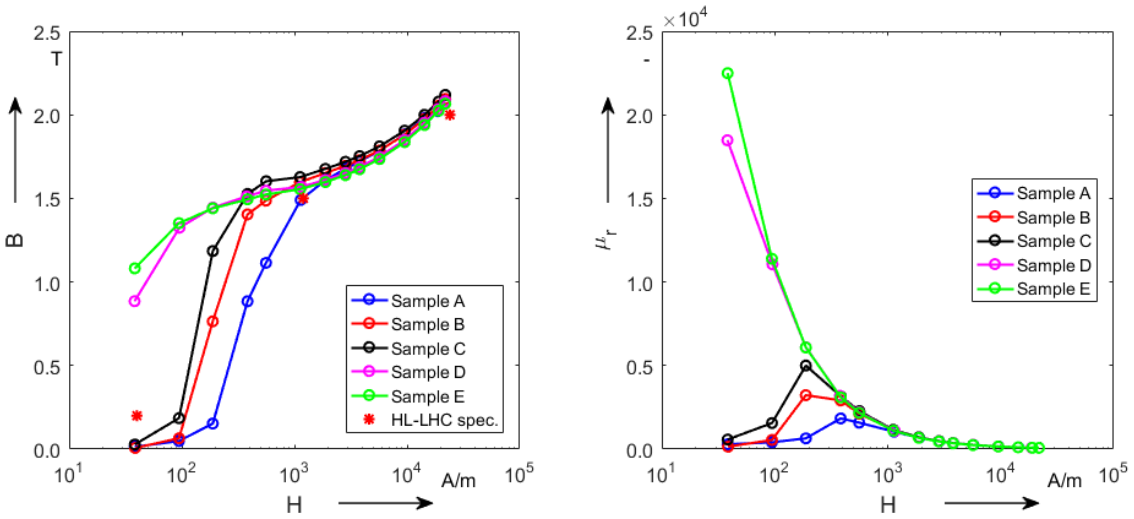

FIGURE 6.1: B-H (left) and relative permeability (right) curves for the five ring samples and the LHC specifications.

The results shown in Fig. 6.1 are from two different sets of measurements: the former for magnetic fields from 40 to 700 A/m, the latter from 700 to 22000 A/m. This is to optimize the accuracy of the obtained B-H curves, since at low fields a lower ramp rate is required. In Table 6.2, the values of the measured flux density B on the samples, at a given value of the magnetic field H, are compared with

TABLE 6.2

Summary of test results of the samples

Sample	A	B	C	D	E	LHC
H [A/m]	B [T]	B [T]	B [T]	B [T]	B [T]	B [T]
40	0.01	0.01	0.03	0.89	1.08	0.20
1200	1.49	1.59	1.63	1.56	1.56	1.50
24000	2.02	2.06	2.08	2.03	2.02	2.00

LHC specifications. The initial specifications are matched by all the samples for magnetic fields higher than 1200 A/m. However, at 40 A/m only samples D and E have shown a corresponding flux density value higher than the CERN threshold of 0.2 T. This is clearly a consequence of the annealing treatment at 850 °C, as increasing the annealing temperature means relaxing the residual stress. Fig 6.1 indicates the large increase of maximum permeability after the final treatment at 850 °C for 5 hours. Permeability is very sensitive to residual stresses, because these impose constraints on the degrees of freedom of the domain structure, thereby engendering the rise of demagnetization fields at the grain boundaries [85]. The reasoning behind the application of an annealing process is to increase both the magnetic and the mechanical properties. Annealing influences the domain's movement, which depends on the grain size, the micro-structure and the impurity's distribution. Furthermore, the more stressful the treatment is (high temperatures, long times of persistences at high temperatures, etc.), the higher is the influence on the magnetic properties, specially at low fields. It is noted that these differences at low fields disappear around the knee of the curve, where the magnetization rotations enter into play. Hence, in this region the effects of the annealing treatment are meaningless because the effect of the saturation's magnetization predominant. Here, the magnetization process proceeds by rotations and the crystallographic texture remains the sole important structural property [51].

Effects of the operation temperature on magnetic properties

Since sample E has shown the highest magnetization properties, it has also been tested at cryogenic temperatures, being the right candidate to replace MAGNETIL BL^{TM}. The aim of this test is to assess the operation performance of the material. Fig. 6.2 shows the influence of the operation temperature on the initial magnetization and permeability curves. Specifically, the figure displays three initial magnetization curves at 300 K, 77 K and 4.2 K. A significant decrease of the material magnetic softening is observed when the temperature drops from 300 K to 77 K. A less significant but still appreciable decrease is observed from 77 K to 4.2 K. Cooling to cryogenic temperatures results in harder magnetic properties. This can be explained with a model of domain wall motion inhibited by inclusions. As for the annealing, it is noted that the differences observed at low fields disappear around the knee of the B-H curve. This means that at operation temperature

the material shows a lower value of maximum relative permeability, but does not change the saturation.

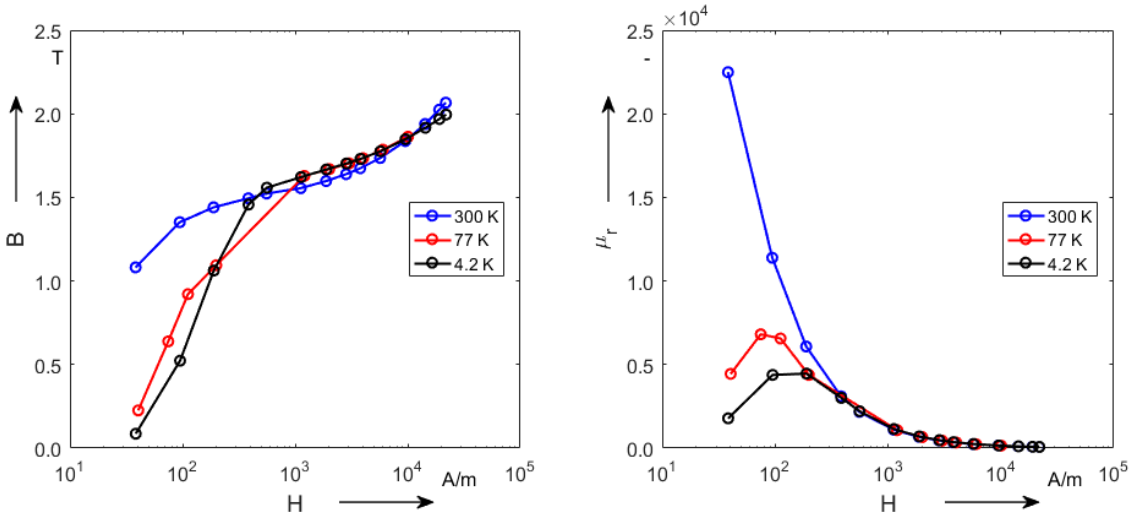

FIGURE 6.2: Initial magnetization curves and relative magnetic permeability of sample E at 300 K, 77 K and 4.2 K

Ageing effects on the magnetic properties

After roughly three years from the first tests, a second campaign of measurements was performed on the same samples (except sample D) to verify their stability and the effects of ageing. Fig. 6.3 and Fig. 6.4 show the results of these new tests.

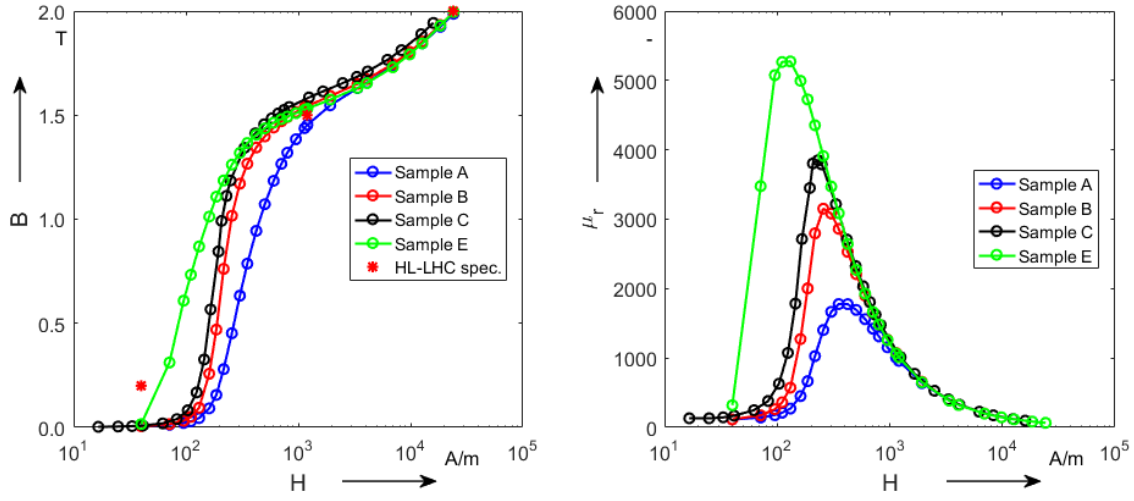

FIGURE 6.3: Results of the recent campaign measurements.

Surprisingly, sample E shows a severe degradation of its magnetic softening, specially at low fields, its magnetic permeability peak going from higher than 22000 to less than 6000, while all the other samples show more or less the same magnetic properties shown in the previous study. This behavior cannot be explained

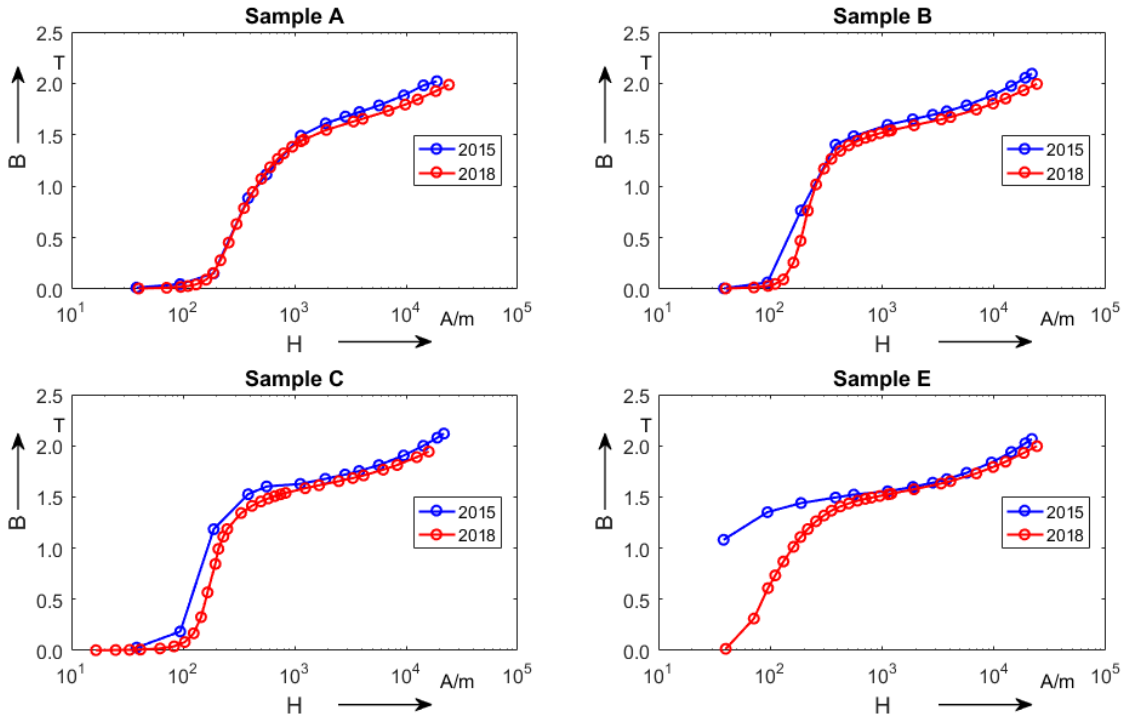

FIGURE 6.4: Difference between the two different campaigns of measurements

by the ageing of the material. Showing better magnetic properties than the others, sample E was selected for further tests at cryogenic temperatures, hence sample E is the only sample that was dipped in a cryogenic thermal bath after the initial tests. The strong degradation shown by sample E in Fig. 6.4 is due to the fact that the material was cooled down to 4.2 K in a fast way and, after the measurements, brought back to room temperature fast as well. These fast changes in temperature may have generated some internal strains which is the cause of sample E magnetic properties degradation. At cryogenic temperatures this effect should exist as well, although, the low temperature effects are predominant respect to the effect of the strain. In the saturation regions the effect is negligible because the behavior of the material in this region is dominated by the magnetization saturation.

Effects of cold work on the magnetic properties

A third campaign of measurement was performed on the second batch of samples, whose description is reported in Table 6.1. These samples are compatible with the annealing shown by sample B in Fig. 6.1. The goal of this third campaign was to verify if the mechanical stress that the material suffers during the production phases could significantly change the material's magnetic properties. For this purpose, the three samples were tested magnetically as delivered from the factory and after the application of a mechanical stress. This consisted of bending the samples along the diameter. In particular, the samples A25112-3 and A25114-4 were bent 6 mm while the sample A25112-4 was bent 4 mm. These tests

correspond to the worse case scenario, because even the inner bending radius of a standard coil does not result in such a bending for the material. The magnetic properties of the material before and after the application of the mechanical stress are highlighted in Fig. 6.5.

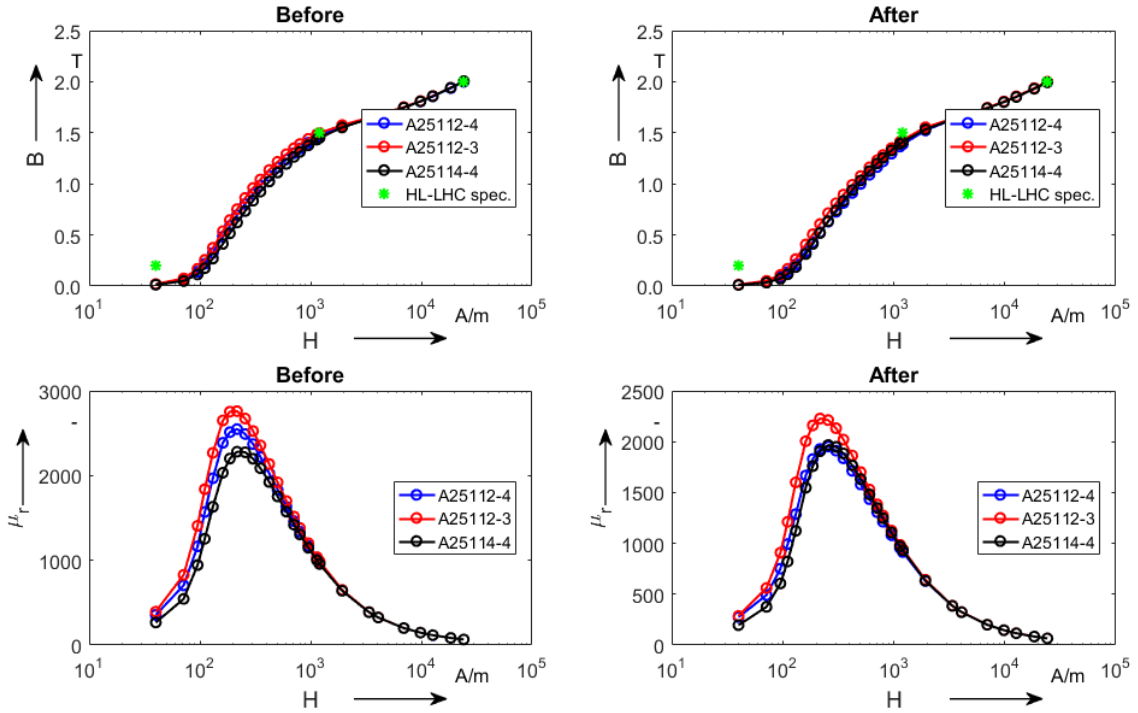

FIGURE 6.5: Measurements performed before and after the application of a mechanical stress to the three samples of the second group of samples

In Fig. 6.6 the comparison before and after the stress for each samples is shown. After the bending, the magnetic properties are degraded, but in a reproducible way. As shown in the diagram of Fig. 6.6, the degradations follow the same trend with the maximum value of degradation at low fields. This means that the mechanical stress affects the initial rather than the peak permeability. Moreover, the results confirm the same conclusions reached for the annealing process. The magnetic properties of ARMCO could be optimized by means of an annealing process, which increases the grain size and optimizes the impurity diffusion within the micro-structure. The problem is that the effects of this optimization are easily lost because the material is a pure iron: a little perturbation is enough to modify and lose the effect of the treatment and the more the material is optimized, the higher will be the degradation of its magnetization. This is confirmed by the results in Fig. 6.5 and Fig. 6.6: the higher is the permeability peak (samples A25112-3 and A25112-4) and the higher is the degradation of the magnetic properties.
In conclusion, it was shown that annealing treatment improves the magnetic performance of the material, if the material is kept at room temperature. However, this improvement disappears after cooling down the material to the operation conditions of 4 K. Moreover, the magnetic performance the material shown at

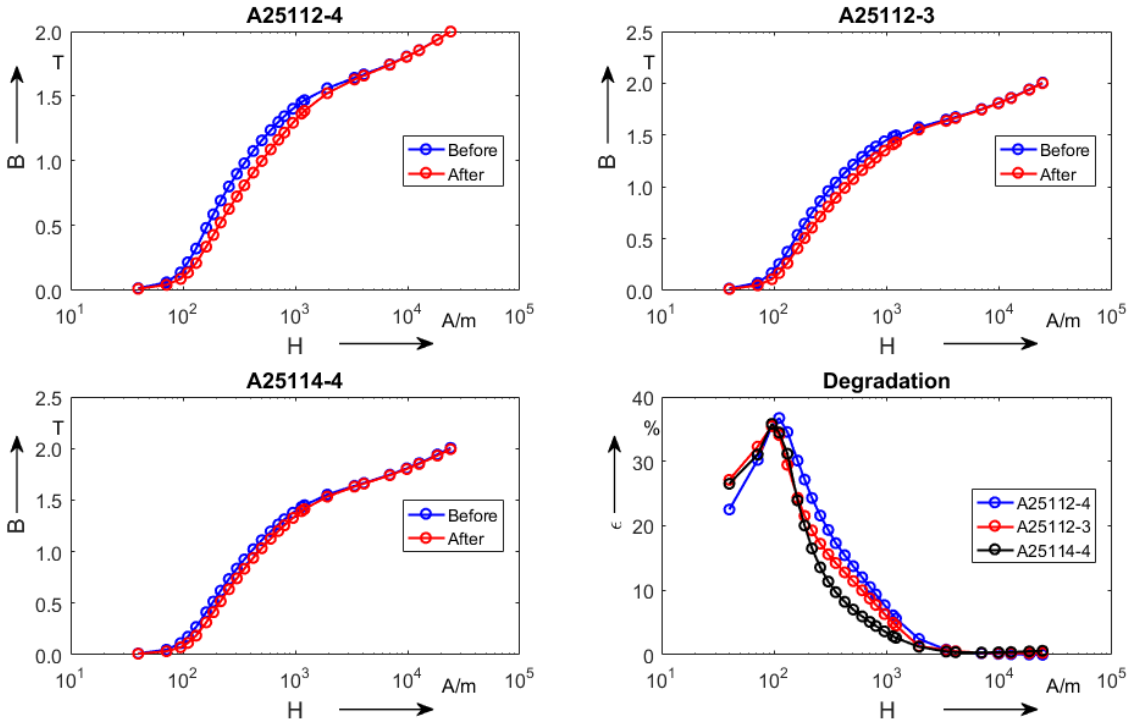

FIGURE 6.6: Comparison between the B-H curves before and after the stress (two figures upper and lower-left) and percentage degrading (lower-right)

room temperature have not been found at cryogenic temperatures. Nevertheless, the results obtained are still acceptable in comparison to the properties of the alternative materials.

Magnetic properties at high magnetic fields

The behavior of the material for much higher magnetic fields (8.6 to 11 T according to the field distribution in HL-LHC magnets) has been studied. This was achieved with the proposed superconducting permeameter. Fig.6.7 shows the initial magnetization (left) and the relative permeability (right) curves of the material. The initial magnetization curve has been measured up to a magnetic flux density of 2.82 T, corresponding to a magnetic field of about 450 kA/m. For such a level of the magnetic field, the relative permeability is 5. The permeability peak value of 1750 appears at a magnetic field of about 350 A/m.
The measurements have a relative expanded uncertainty of 0.01% (with a coverage factor of 2) on the values of H and uncertainty of 1% on the values of B and μ_r. In Fig. 6.7a, the red curve corresponds to the initial magnetization curve calculated using the Wlodarski equation. The parameters of the equation, retrieved by using the method described by Wlodarski in [141], are: $\mu_0 M_a$=0.49224 T, $\mu_0 M_b$ =1.7478 T, a =9340.0 A/m and b =214.59 A/m.
The Wlodarski fitting shows higher values of flux density at low fields (up to 200 A/m). This because the fitting does not take into account some physical phenomena that occur in this region. In particular, with this set of parameters, there

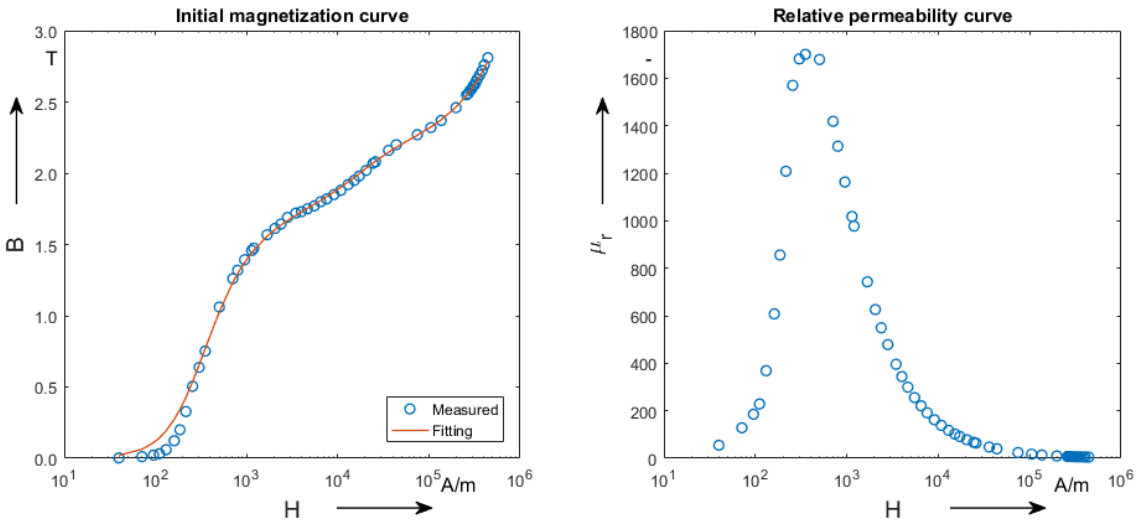

FIGURE 6.7: Results of the characterization up to a magnetic flux density of 2.82 T.

is a maximum difference of 0.15 T at 160 A/m whereas an average difference of roughly 12 mT occurs at higher fields.
Fig. 6.8 shows a comparison between the initial magnetization curve of i) ARMCO (data presented in this work), ii) MAGNETIL (data from LHC magnets' production), and iii) a standard steel (data from ROXIE database). The three *B-H* curves show a very similar magnetic behavior when well saturated ($H > 3000$ A/m). This means that the three materials have a similar chemical composition. Nevertheless, for $H < 3000$ A/m ARMCO shows a completely different behavior, while the other two present similar shapes. This means that these last two have been annealed or cold worked differently. The region of interest for the new superconducting magnets for HL-LHC has been zoomed out in Fig.6.8b. Although the three materials seem to have the same magnetic behavior (same shape of the B-H curve), in the region $20000 < H < 100000$ A/m MAGNETIL and ARMCO present a higher flux density values than ROXIE material, while for $H > 100000$ A/m, ARMCO shows higher flux density values than MAGNETIL that shows higher flux density values than ROXIE material. This demonstrates the importance of characterizing materials for magnet yokes at their operational magnetic field. This comparison also raises the problem of checking how big is the impact of using a wrong *B-H* curve during the magnet design phase. This problem is addressed in the following section for the new HL-LHC superconducting quadrupoles and dipoles.

Impact of the BH on the field quality

This section evaluates the impact of the iron magnetic properties on the magnetic transfer function (TF), defined as the ratio between the main field and the magnet current. The two Nb_3Sn High Field Superconducting magnets for the HL-LHC, MQXF and the MBH-11T are studied. Simulations are performed in ROXIE, a BEM-FEM 331 program developed at CERN [118], using three different

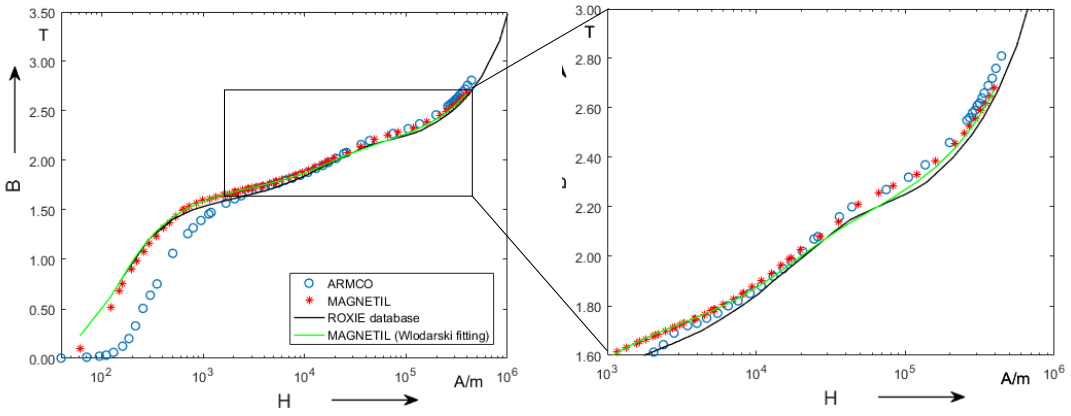

FIGURE 6.8: Comparison between the initial magnetization curve of i) ARMCO (data presented in this work), ii) MAGNETIL (data from LHC magnets' production), and iii) a standard steel (data from ROXIE database).

B-H curves: i) ROXIE database, ii) MAGNETIL measurements reported in [23, 20], iii) ARMCO measurements reported in this paper.
MBH-11T is 60 mm aperture dipole and 11.2 T field, operating at a nominal current of 11.85 kA. Each coil consists of 56 turns, 22 in the inner layer and 34 in the outer layer. The magnetic length is 5.3 m, meaning that two 11 T magnets are delivering the same integrated magnetic strength as one 8.3 T LHC main bending dipole. The transfer function on the magnet straight section as a function of the current is shown in Fig. 6.9 (right). The different iron magnetization behaviour has a significant impact on the main field. The transfer function at the nominal field is 4.5 mT/kA higher in the case of ARMCO as compared to ROXIE database and 2 mT/kA higher for MAGNETIL, showing the importance of a good magnetic characterization of the iron yoke.
MQXF is a 150 mm diameter aperture quadrupole and 132.6 T/m gradient, operating at a nominal current of 16.46 kA. Each coil consists of 50 turns, 22 in the inner layer and 28 in the outer layer. The magnet will be produced in two lengths, MQXFA and MQXFB, with a magnetic length of 4.2 m and 7.15 m respectively. Fig 6.10, left, shows the transfer function in the magnet straight section as a function of the current. The TF decreases by around 9 % from injection to nominal current due to the iron saturation effect. For this case, the different iron magnetization behaviour has an even more significant impact on the main field. The different iron magnetization behaviour has a significant impact on the main field. The transfer function at nominal field is 38 mT/kA higher in the case of ARMCO as compared to ROXIE database and 23 mT/kA higher for MAGNETIL, This case study confirms the importance of characterizing materials for magnetic yokes at their operational magnetic field.

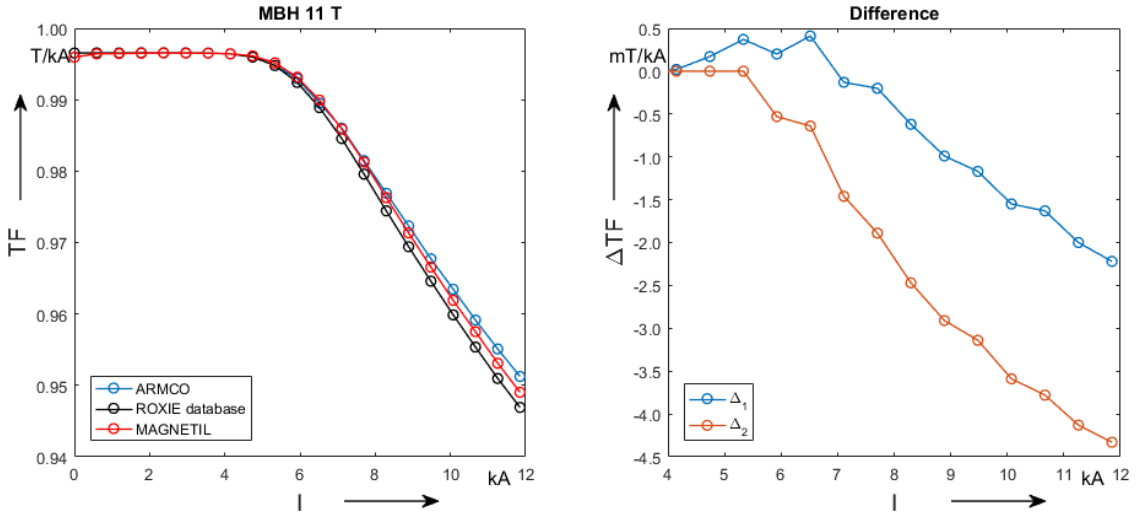

FIGURE 6.9: Comparison between the MBH-11 T transfer functions based on the BH curves of Fig.6.8. Δ_1 and Δ_2 are the differences between the transfer functions evaluated by using the ROXIE and MAGNETIL curves instead of the curve of the employed material, respectively.

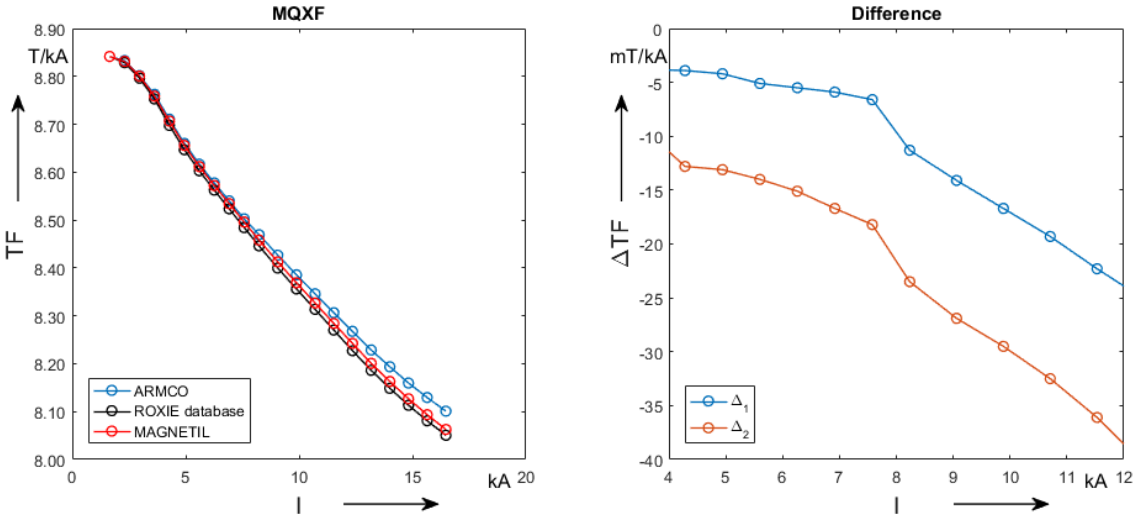

FIGURE 6.10: Comparison between the MQXF transfer functions based on the BH curves of Fig.6.8.

6.2 Case study II: Characterization of a material for magnetic shielding

In this section, CRYOPHY has been evaluated as magnetic shield material for the last-generation cryomodule prototypes of crab cavities used in particle accelerators for transverse deflection. The relative magnetic permeability has been measured at room and cryogenic temperature by means of the split-coil and the cryogenic permeameter and its lowest value at 4 K fits the minimum design criteria of 100 000 for the crab cavities experiment at CERN. Permeability after uniaxial

plastic deformation between 0% and 3% has been also measured by means of an Epstein frame. Results show that deformation induces a significant decrease in the magnetic performances, underlining that particular care must be taken during all stages of handling and operation. Finally, the attenuation inside the magnetic shields has been tested for the prototype Super Proton Synchrotron at CERN. Results highlight that at 150 mm from the opening, the magnetic field is shielded as required.

6.2.1 Material and test specimen

Cryophy, a registered trademark of Aperam, is a Ni-based ferromagnetic alloy, namely 81% of Fe, 14% of Ni, and 5% of Mo in weight. It is specifically aimed to maximize magnetic permeability at cryogenic temperatures, by a tailored composition and a defined heat treatment. Cryophy is very similar in most properties to MuMetal (ASTM A753, alloy 4), which is used as the "warm" magnetic shielding of the crab cavities outside of the helium tank.

The following sets of samples were assembled and tested at CERN laboratories:

- 15 sample rings, for quasi-static measurements of the magnetic permeability at room temperature (RT), in liquid nitrogen (77 K), and in liquid helium (4 K);
- 8 samples according to ISO 6892 [76], with a parallel length of 62 mm, for evaluating the stress-strain behavior before straining by tensile test;
- 32 strip samples (320 mm by 40 mm), for measuring AC magnetic permeability in an Epstein frame, before and after the introduction of unidirectional mechanical strain.

All the samples were annealed by the supplier, Magnetic Shields Ltd, in their final geometry, in order to avoid losses in magnetic permeability due to cutting. The samples have the thickness of 1 mm, analogously as the wall of the manufactured magnetic shields, in order to emulate their behavior in operation.

6.2.2 Experimental results

Temperature characterization

The DC magnetic properties of the samples were characterized by the proposed flux-metric method, by measuring hysteresis loops, as well as initial magnetization and relative magnetic permeability curves, at different temperatures in several operating conditions. Three tests were performed to observe the change of permeability at room temperature, with liquid Nitrogen at 77 K and with liquid Helium at 4.2 K. Figs. 6.11a and b show the hysteresis loops for excitation magnetic fields up to 10 A/m and 80 A/m, respectively, at room temperature of a 5-layer sample of Cryophy. The hysteresis loop shape is typical for a permalloy material. The sample enters in its saturation region when the applied magnetic

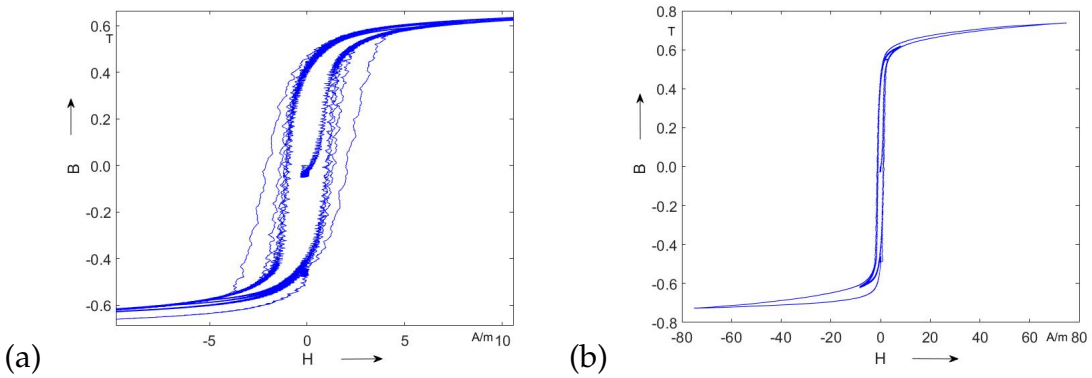

FIGURE 6.11: DC hysteresis loops of a 5-layer sample of Cryophy at room temperature for an excitation field up to (a) 10 A/m and (b) 80 A/m.

field reaches 4 A/m. The coercive field is estimated to be 1 A/m, and the highest value of the flux density induced in the sample is 0.75 T.
Fig. 6.12a shows the influence of the temperature on the initial magnetization curve. Specifically, the figure displays three initial magnetization curves at 4.2 K, 77 K, and 300 K, respectively. For a magnetic field H_0 lower than roughly 50 A/m, the material shows a flux density B_s lower at cryogenic temperatures than at RT.

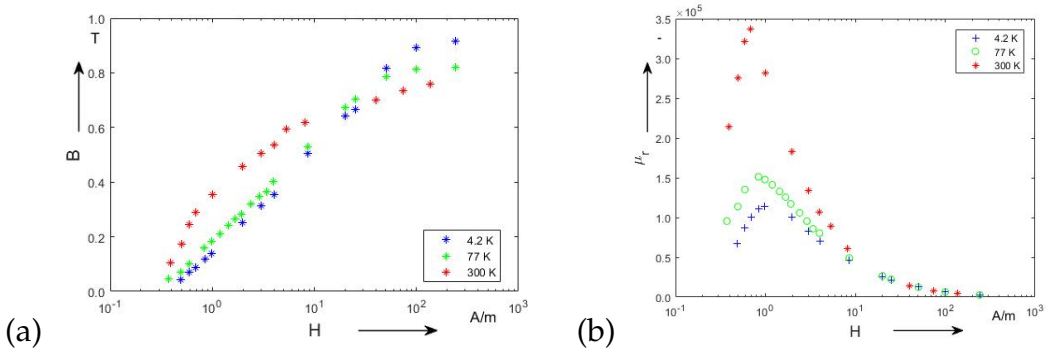

FIGURE 6.12: (a) Initial magnetization curves and (b) relative magnetic permeability of a Cryophy 5-layer sample at 300 - 77 - 4.2 K.

For lower magnetic fields, the material shows higher values of flux density at RT. This is the region where the relative magnetic permeability peak appears, as shown in Fig. 6.12b. In particular, the results highlight how the relative magnetic permeability is strongly related to temperature: The maximum peak drops from 337,000 at 300 K to about 151 000 at 77 K (55% reduction), and then to about 114 000 at 4.2 K (66% reduction). Nevertheless, the maximum relative permeability is always above the design requirement value of 100 000. The movement of the magnetic domains is influenced, among other parameters, by the microstructure of the material, its grain size, its impurity distribution, and eventual heat treatments. At low magnetic fields, the effect of the temperature is significant, because the magnetization is mostly due to the unstable boundary displacement. Due to the cryogenic condition, the thermal contraction creates a sort of freezing of the

magnetic domains. Conversely, at high fields, the magnetic behavior is mostly dominated by the magnetization of saturation. The orientation of the magnetic domains is mainly due to the much more stable magnetization rotation, which makes the effect of the temperature negligible.

Mechanical strain characterization

In mechanical tests, initially, tensile tests were carried out for determining the stress-strain behavior of the Cryophy samples. Then, the intrinsic mechanical properties of the material were verified. Finally, the uniaxial magnetic properties of the strip samples were characterized in AC by the standard Epstein frame method [71], by assessing hysteresis and relative magnetic permeability curve at varying the strain states, in several operating conditions. The tensile tests were aimed at determining the stress-strain behavior of the Cryophy samples before introducing the mechanical strain devoted to magnetic permeability tests, as well as the values of mechanical strain for the test.
The tests were carried out on an Ultimate Tensile Strength (UTS) tensile machine by clamping the upper and lower ends of the samples and using a gauge length of 50 mm. Test speed was varied between the samples, applying strain rates of $2{\cdot}10^{-4}$/s, $2{\cdot}10^{-5}$/s and $2{\cdot}10^{-6}$/s and the samples were loaded until break while recording the stress-strain curve. The stress-strain behavior of the material does not show any significant influence of strain rate (Fig. 6.13). It is thus independent of the strain rate within the applied range between $2{\cdot}10^{-4}$/s and $2{\cdot}10^{-6}$/s. The yield strength is at 139 MPa, followed by pronounced plastic deformation with an ultimate tensile strength around 500 MPa, just before break (Table 6.3). Necking of the test specimens is not observed. The material is very ductile and

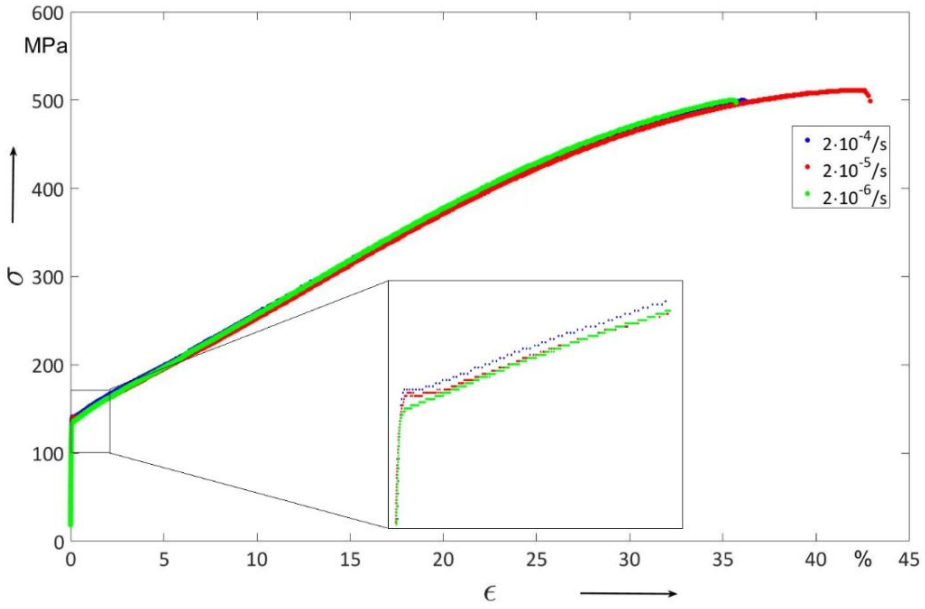

FIGURE 6.13: Stress-strain curves for Cryophy at different test speeds.

the elongation at break exceeds 35% in all cases (Fig. 6.13). An increase in surface roughness during testing has been recorded already at low elongations and increased further until the end of the test (Fig. 6.14).

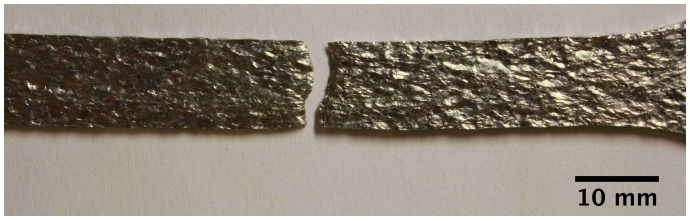

FIGURE 6.14: Surface state of tensile sample after failure. Initially, the roughness of the surface was not visible.

Since the surface state may distort or otherwise affect the magnetic measurements, it was concluded that only strain states at low deformation should be taken for these measurements. A detailed observation of the stress-strain curves at low deformation shows that the stress-strain behavior below 0.5% of elongation may vary between individual samples (Figure 6.13, zoom). Four different

TABLE 6.3: Tensile test results (uncertainty at confidence level of 95%)

$R_{\mathrm{p0.2}}$ [MPa]	R_{m} [MPa]	E [GPa]	A [%]
139 ± 6	504 ± 16	233 ± 47	38 ± 10

with $R_{\mathrm{p0.2}}$ as the yield stress at 0.2% plastic deformation, R_{m} as the ultimate tensile stress, E as the Young's modulus and A as the plastic elongation at break.

strain states were applied to four different sets of eight samples each one, likewise using the UTS tensile machine. The samples were mounted into the grips (occupying the full width of the sample) and an extensometer with a gauge length of 50 mm was used to measure the percentage of strain in the center of the samples. The desired final strain was programmed for each sample and the speed to reach this strain was 5 mm/min. The strain states applied were 0.5%, 1%, 2% and 3%.

After the straining, the strips were reduced to a length of 280 mm, to discard the areas held by, and close to the grips. The width was reduced to 30 mm to discard areas of non-uniform strain at the edges of the samples.

A first (lowest) strain state of 0.5% was thus chosen; the other three values were selected at 1%, 2%, and 3%, without considering the elastic spring-back (the elastic part of the deformation). Considering an elastic modulus of 230 GPa, the selected strain of 0.5% would go back to 0.44% and a strain of 3% while under stress would spring back to 2.92% when released. The stresses needed to reach these strain states are 143 MPa, 150 MPa, 163 MPa and 175 MPa, respectively (Tab. 6.4).

Upon visual observation of the samples after straining, an increase in surface roughness between the different strain states is visible, which is confirmed by

TABLE 6.4: Strain states used for permeability measurements and corresponding stresses.

Nominal strain [%]	Calculated strain after spring-back [%]	Corresponding stress [MPa]
0.5	0.44	143
1.0	0.93	150
2.0	1.93	163
3.0	2.92	175

surface roughness measurements (Fig. 6.15). Between 0% and 1% of strain, the roughness gradually increases; between 1% and 2% R_a doubles before it reaches its maximum at 3% strain.

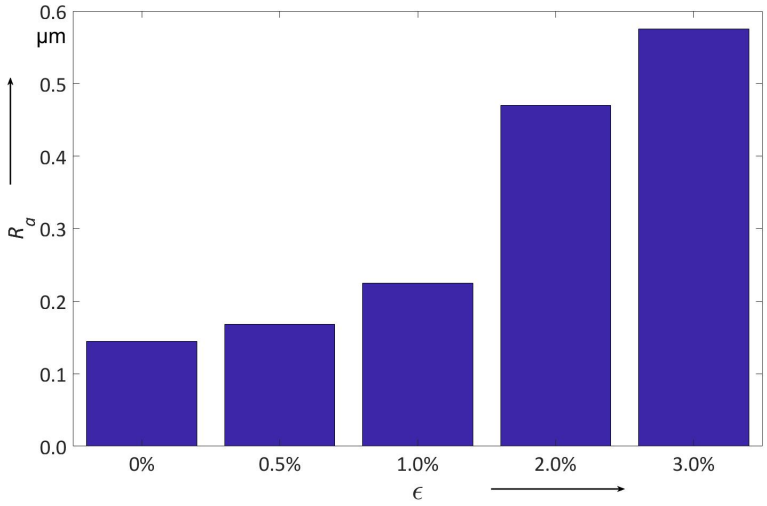

FIGURE 6.15: Surface roughness R_a of strained samples.

AC magnetic properties measurements on strained samples

The hysteresis curves show the effect of the mechanical strain on the magnetic behavior. The unstrained sample has a much lower coercive field and reaches about twice the magnetization (indicated by the higher magnetic induction) as the sample with a strain of 1% (Fig. 6.16a). As expected for this application, negative behavior increases with increasing strain. A noise is observed in the magnetic field strength as a result of the measurement frequency. At higher fields, magnetization of the strained materials is easier, thus the difference between unstrained and strained material is less pronounced. The coercive field increases with mechanical strain, making the material magnetically harder. At a field of 230 A/m, and in contrast to the hysteresis at 20 A/m, a saturation is observed for the unstrained material, indicated by the asymptotic form of the B-H curve at high field strength. However, the strained samples do not reach the saturation induction of

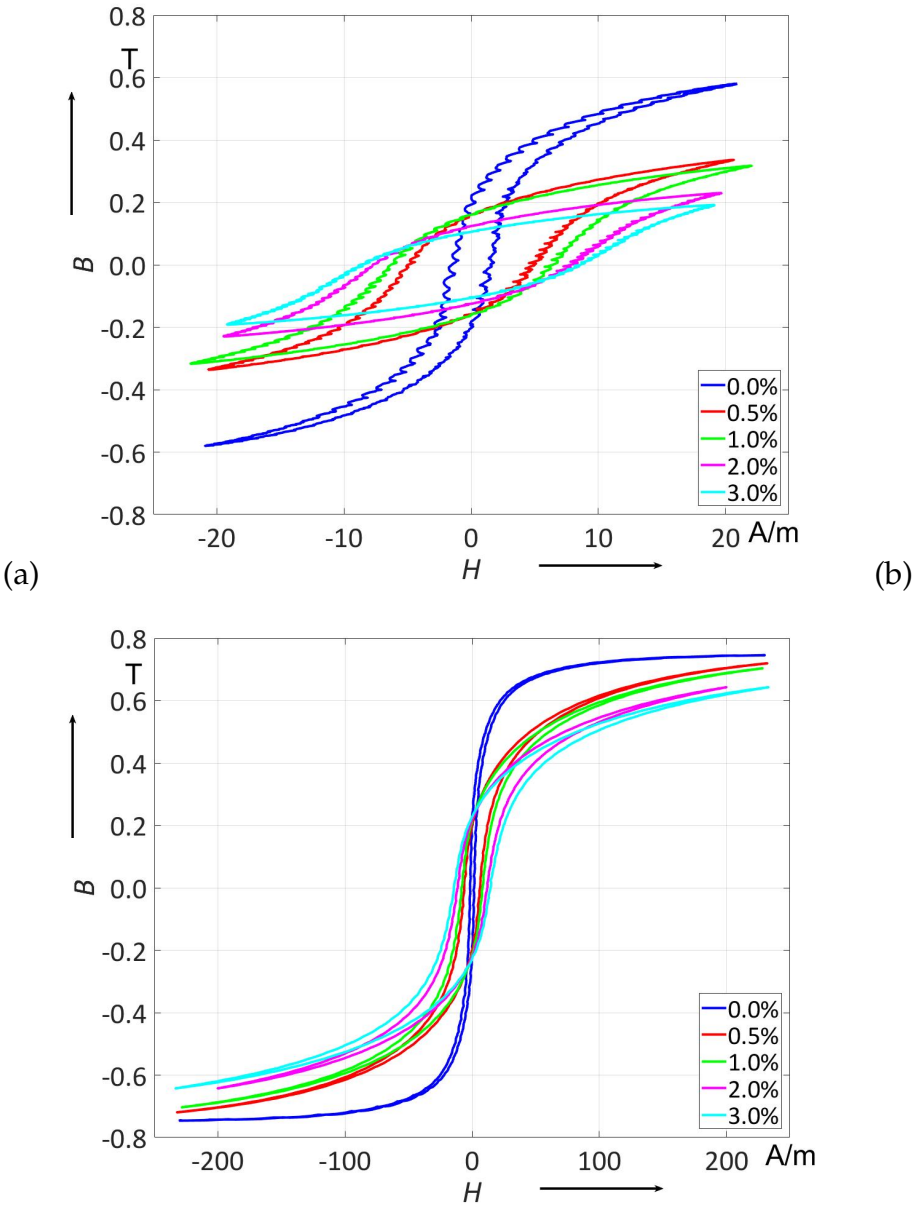

FIGURE 6.16: Hysteresis curves for different strain states of Cryophy at 0.5 Hz, (a) 20 A/m, and (b) 230 A/m.

the unstrained state (Fig. 6.16b). The measurement frequency is the same. Thus the noise in field strength is identical.
Besides the effect of the strain states, the hysteresis curves also show the influence of the excitation frequency. The higher this frequency, the less time the material has to respond, highlighting the time-dependence of the magnetization. Therefore, the coercive field and the residual flux density increase according to the frequency. At higher magnetic fields, which facilitate fast magnetization, the same magnetization is reached for all frequencies (Fig. 6.17a). The magnetization of the material for a high frequency can only follow above a certain field; at lower fields the magnetization cannot follow the field in the time of one cycle at 50 Hz

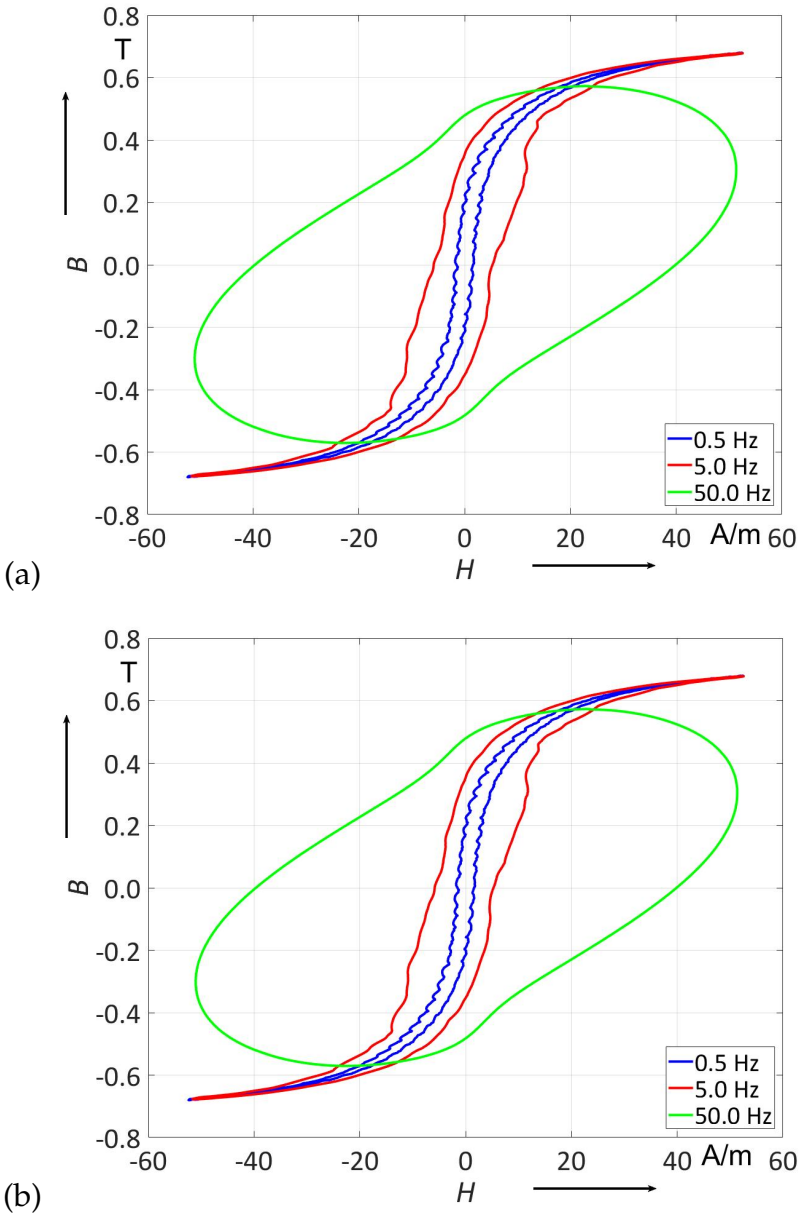

FIGURE 6.17: Hysteresis curves of unstrained Cryophy for different measurement frequencies at (a) 100 A/m and (b) 50 A/m.

(Fig. 6.17b).
As a consequence of the observed hysteresis, the relative magnetic permeability of Cryophy at 0.5 Hz shows a strong dependence on the mechanical strain, which is most pronounced at low field strength. In the unstrained case, the permeability peak is out of the measurement range; by increasing strain, it shifts towards higher field strength (Fig. 6.18). At the same time, the peak permeability significantly decreases with the strain.
An increase in frequency of the input signal shows a decrease of the relative magnetic permeability at low fields. At fields higher than 50 A/m, the curves for all frequencies are congruent (Fig. 6.19). This reflects what was found in Fig. 6.17:

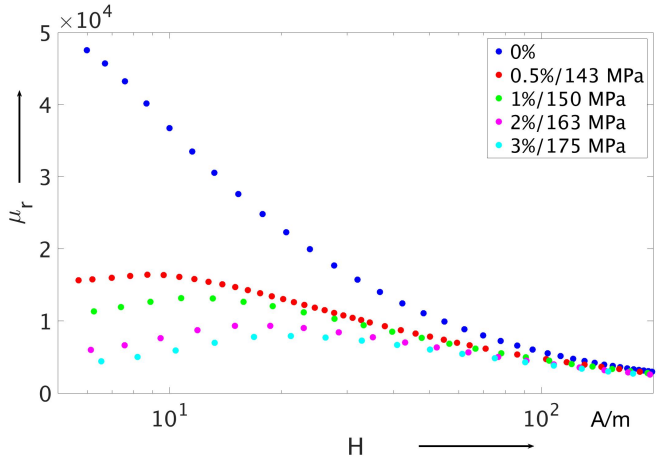

FIGURE 6.18: Relative magnetic permeability of Cryophy measured with the Epstein frame at 0.5 Hz for a different mechanical strain.

the saturation magnetization is identical at high fields, but for low fields the magnetization decreases with the frequency. Analogous behavior is observed for the

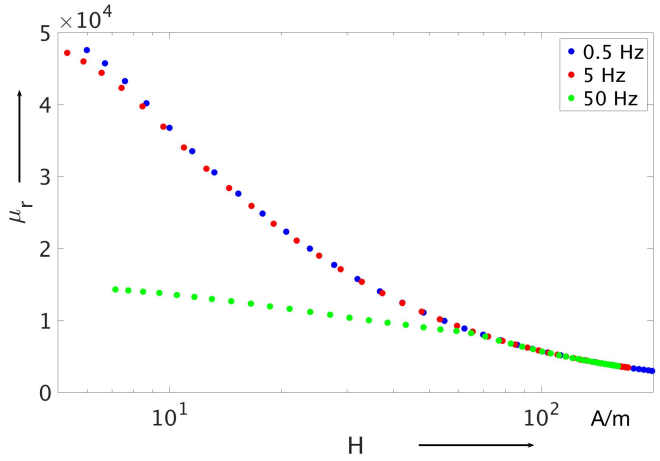

FIGURE 6.19: Relative magnetic permeability of unstrained Cryophy at varying measurement frequency.

curves at different strain states: for a frequency of 50 Hz, the curves are joining above 50 A/m (Fig. 6.20).

Evaluation of the magnetic shield attenuation

The measurement of the magnetic attenuation inside the shield aims to verify the absorption of the external magnetic field by the manufactured magnetic shields for the SPS prototype test.
The layout of the measurement system, hosted at CERN's magnetic measurement laboratory in Geneva, is shown in Fig. 6.21. It mainly consists of i) a fluxgate by Bartington Instruments, with an uncertainty of ± 1 nT, ii) a Magmeter Bartington Instruments as a display unit, iii) a high-precision linear translation stage with a

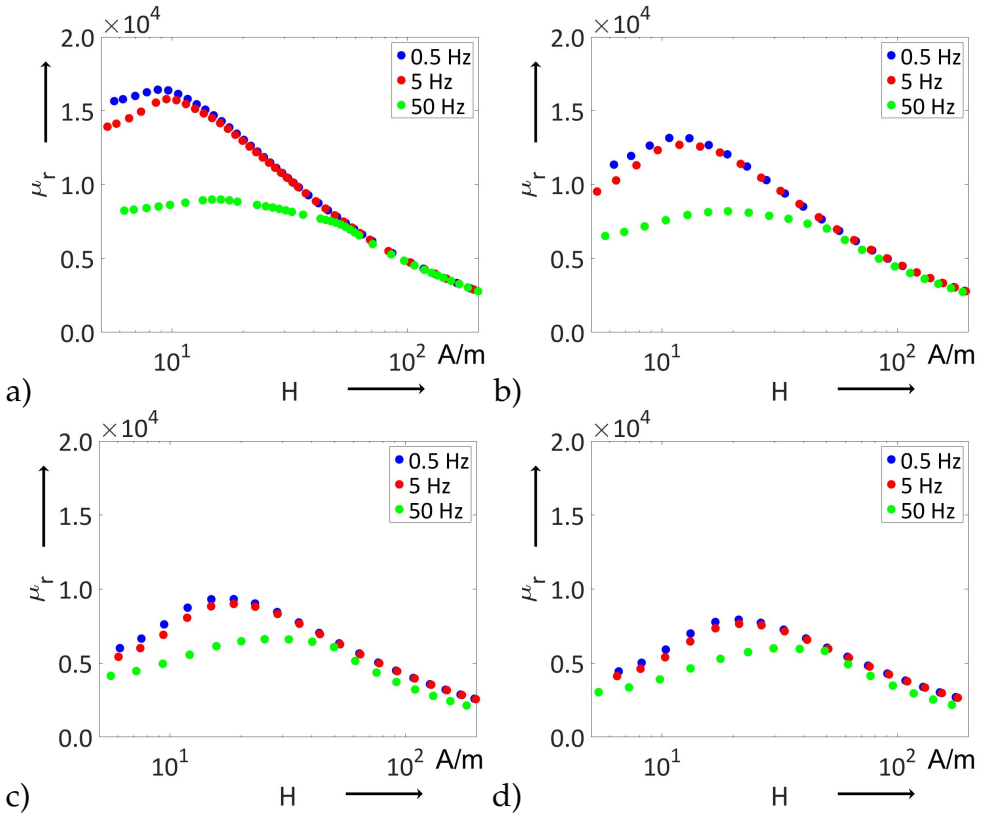

FIGURE 6.20: Relative magnetic permeability of strained Cryophy in dependence of measurement frequency: a) 0.5%, b) 1%, c) 2%, and d) 3%.

controller for moving the fluxgate with a relative precision of 1 ppm and recording the relative distance between two consecutive measurements, (iv) and a National Instrument acquisition card USB-6366. The overall measurement system is automatized by means of a suite of interactive programs developed in C++ using the above mentioned framework for magnetic measurements (FFMM [16]). Fig. 6.22 shows the geometry of the cryomodule magnetic shield.
The measurement is carried out by moving the fluxgate along the z-axis and acquiring the amplitude of the magnetic field in the three directions x, y, and z. The magnetic attenuation is defined as the ratio of the magnetic field without and with the shield:

$$a_x = \frac{B_b(x)}{B_s(x)}; \quad a_y = \frac{B_b(y)}{B_s(y)}; \quad a_z = \frac{B_b(z)}{B_s(z)} \tag{6.1}$$

with a_x, a_y, and a_z the attenuation for each axis; B_b and B_s the flux density measured without and with the shield, respectively. The total attenuation is calculated as:

$$a_{\text{total}} = \sqrt{a_x^2 + a_y^2 + a_z^2} \tag{6.2}$$

Fig. 6.23 shows the change of magnetic field in the three directions with (*u lis(s)*) and without the shield (*u lis(b)*, background field), plotted against the axis z along

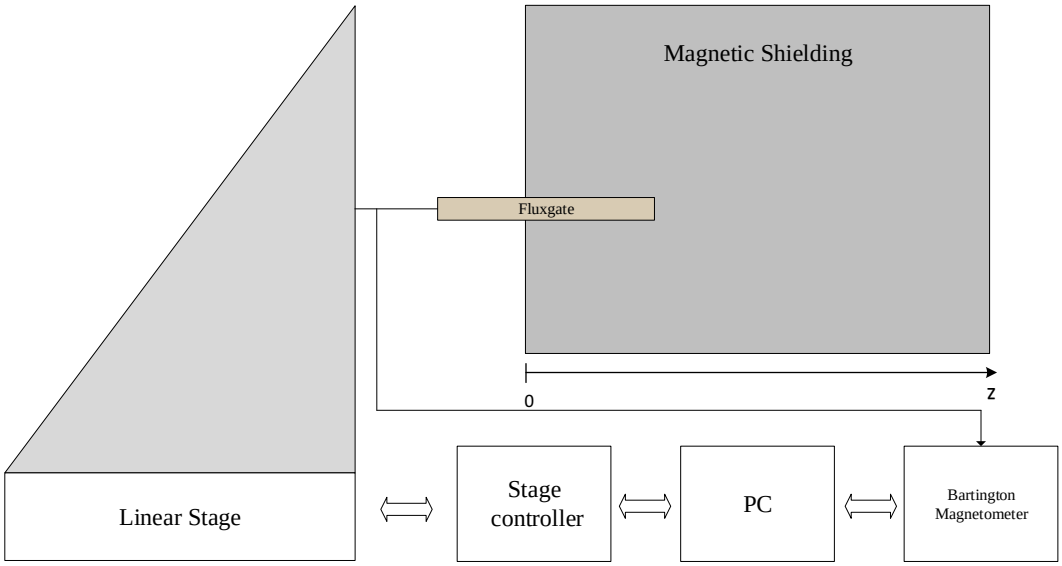

FIGURE 6.21: Layout of the attenuation measurement system.

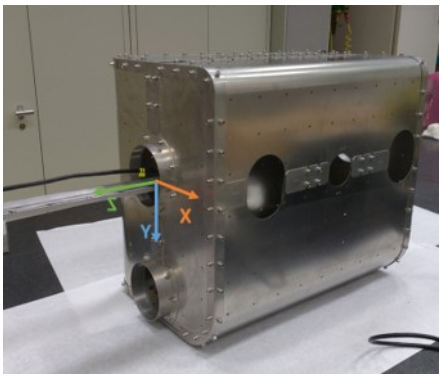

FIGURE 6.22: Cold magnetic shield of the Crab Cavity experiment at SPS

which the shield is entered. The components x and y of the flux density are attenuated earlier than the component z: at 100 mm from the opening the x- and y-components of the flux density are completely shielded. At 150 mm from the opening, the magnetic field is entirely shielded.

Discussion

The DC measurement results at different temperatures show that, even though the material is designated for use at cryogenic temperatures, it also has a superior magnetic behavior at room temperature. This underlines the advantage of a warm magnetic shield outside of the cryogenic vessel. Conversely, the advantage of the cold shield is its position directly around the cavity, without any other possibly interfering equipment. The peak permeability at 4 K is just above the design value of 100 000, so that any adverse effects, i.e. mechanical deformation, will result in a lower permeability.

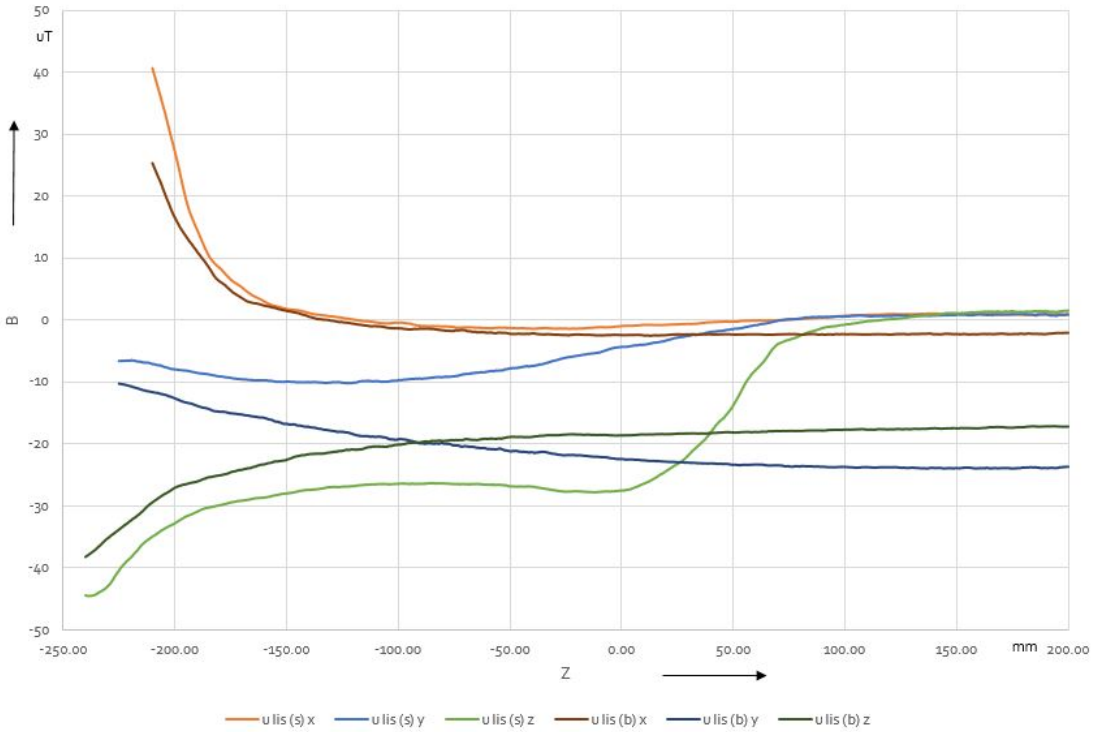

FIGURE 6.23: Magnetic field with (*u lis(s)*) and without (*u lis(b)*) the sample. The point z=0.00 mm corresponds to the center of the hole.

The relative magnetic permeability of a ferromagnetic material depends on its magnetization, which is expressed in the magnetic flux density. During the Epstein frame measurements, a decrease in relative permeability was observed with increasing mechanical strain, more pronounced at low fields, and with increasing measurement frequency at low fields.
Assuming that a ferromagnetic material contains many randomly-oriented domains in which the magnetization is saturated, its response to an external magnetic field is described by two mechanisms. Under the effect of a low external field, favorably-oriented domains are growing at the expense of those unfavorably oriented. By applying a higher external field, the magnetization turns to accord with the orientation of the external field [79].
The mechanical strain in the samples increases the dislocation density. The experimental results highlight that this increment has an adverse effect on the process of magnetization and therefore the magnetic permeability. Thus, the existence of dislocations is hindering both the growth and the orientation of domains (pinning of domains).
The AC measurement results show that a frequency variation affects the material magnetic behavior only for low fields. In the case of 50 Hz, a magnetic field value can be detected, below which the related trend $\mu_r - H$ is distinct from the other curves at lower frequencies. A lower threshold can be detected, below which the $\mu_r - H$ trend for 0.5 Hz is different compared with the one at 5 Hz. The process at higher fields, namely the orientation of domains, is a process (a simple flipping of orientation) faster than the growth of domains, which involves a more significant

number of energetic steps during the turning of the Bloch walls, creating a strong time dependency [79]. Therefore, the process of domain growth is much more affected by a high frequency. The effect of the domains flipping requires certain energy, which is introduced by a sufficiently-high external magnetic field.
A direct comparison between DC and AC (Epstein frame) measurements is not possible. The results show that at a specific excitation magnetic field the corresponding flux density measured in DC is much higher than in AC. Due to measurement limitations, it was not possible to determine the position of the peak permeability for the unstrained material at 0.5 Hz. Assuming that the peak permeability for the unstrained material at 0.5 Hz is around 50 000, there is a factor of about 7 between the peak permeabilities obtained at DC and 0.5 Hz.
The magnetic field in the CERN accelerator complex can be modeled as a ramped DC field, so that the negative influence of higher frequencies may be disregarded for this application.
An additional effect that can adversely affect the magnetizability, and therefore limit the magnetic permeability, is the surface roughness as a side effect of plastic deformation. However, considering the rather low difference in roughness between strains of 0% and 0.5%, in combination with the high loss of magnetic permeability, the plastic strain is the predominant cause of the change in permeability.
Finally, the shielding performance of the crab cavity cryomodule was tested using a custom measurement system developed at CERN for this purpose. The results are encouraging. The magnetic shield is able to shield the inner part of the cryomodule from a surrounding magnetic field of roughly 30/40 μT, generated by the surrounding devices, such as electromagnets, presented in the laboratory. The components x and y of the magnetic field are attenuated earlier than the z-component.

6.3 Case Study III: Effect of B-H curve on field quality for normal conducting magnets

In this section, the importance of magnetic material measurements in the framework of the design of magnets for particle accelerator is discussed.

6.3.1 Characterization of ferromagnetic materials

This paragraph shows the results of the magnetic characterization of five different ferromagnetic materials. The materials have been (or will be used) for the production of yokes of several normal conductor magnets at CERN.
Fig. 6.24 shows the initial magnetization profiles (left) and the relative permeability curves of the materials (right). In Fig. 6.26, the ARMCO curves stored in a CERN database and in OPERA [104] are compared with the curves obtained experimentally from its magnetic characterization. The OPERA trends are quite

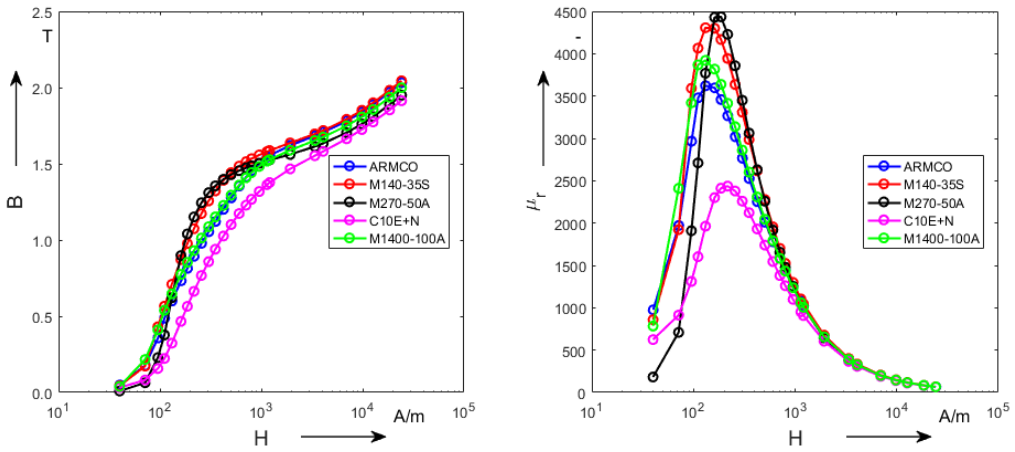

FIGURE 6.24: Comparison among the initial magnetization curves (left) and relative permeability curves (right) of the five samples.

different from the other two, showing higher permeability peak and lower saturation level. The other two initial magnetization trends are quite similar (the logarithmic scale on x-axis amplifies the difference). This means they could refer to the same material and that some post-production treatments or different annealing probably cause the differences. Discrepancies are stronger in the first part of the magnetization curve, up to 1000 A/m. After this threshold, both curves have the same shape, showing that the saturation region is less sensitive to annealing and other treatments. On the other side, the relative permeability curve and, especially, the permeability peaks show significantly different behaviors.

This comparison raises the problem of checking how big is the impact of using

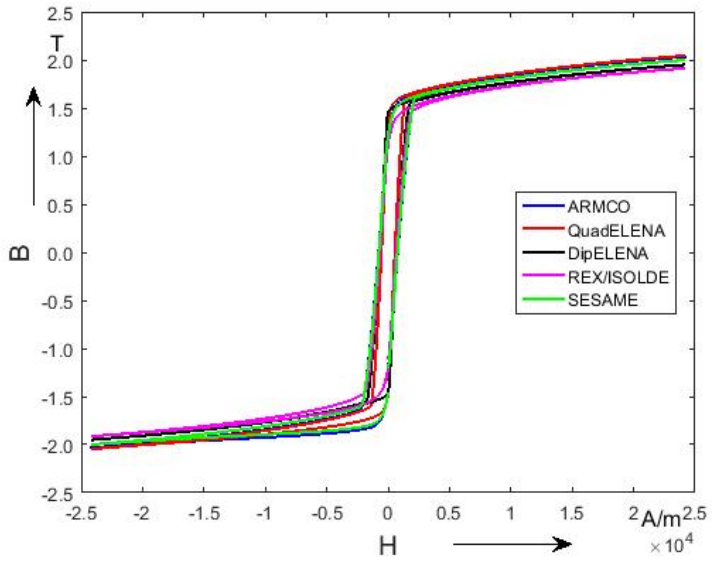

FIGURE 6.25: Hysteresis cycles

a wrong B-H curve during the magnet design phase. This problem is addressed in the following section for a case study.

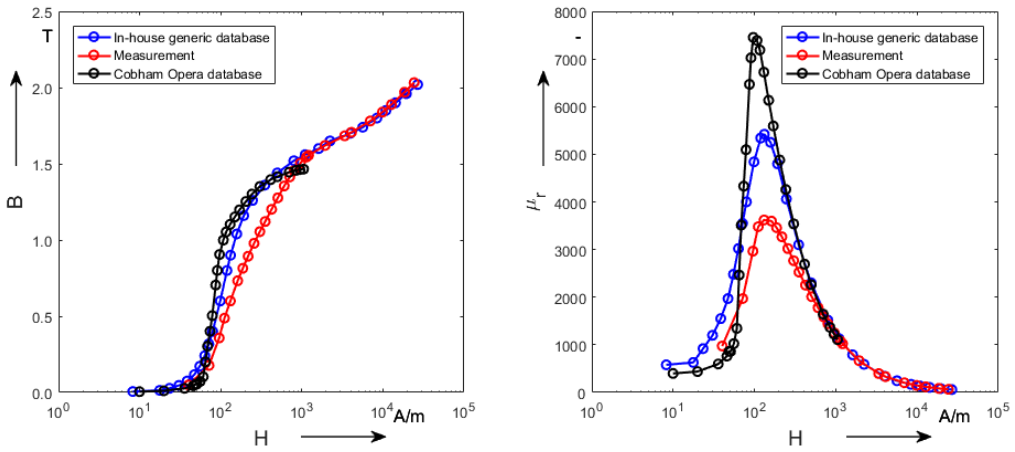

FIGURE 6.26: Comparison among initial magnetization (left) and permeability curves (right) of ARMCO obtained from CERN database (blue), OPERA software (black) and experimentally measured (red).

6.3.2 Case Study: Q200 quadrupole magnet

This section shows how the magnetic properties of a magnet yoke can affect the performance of the whole magnet. A case study based on the normal-conducting quadrupole magnet Q200 [103, 127] and Finite Element Analysis (FEA) is presented. The magnet has a rated current, $I_n = 750$ A, and 63 turns per pole to achieve a nominal gradient of $G = 11.0$ T/m and integrated gradient of $int_G = 22.05$ T. Fig. 6.26 shows the three B-H curves used for the simulation: (1) Cobham OPERA database[127], (2) in-house CERN database, and (3) measured from a steel sample.

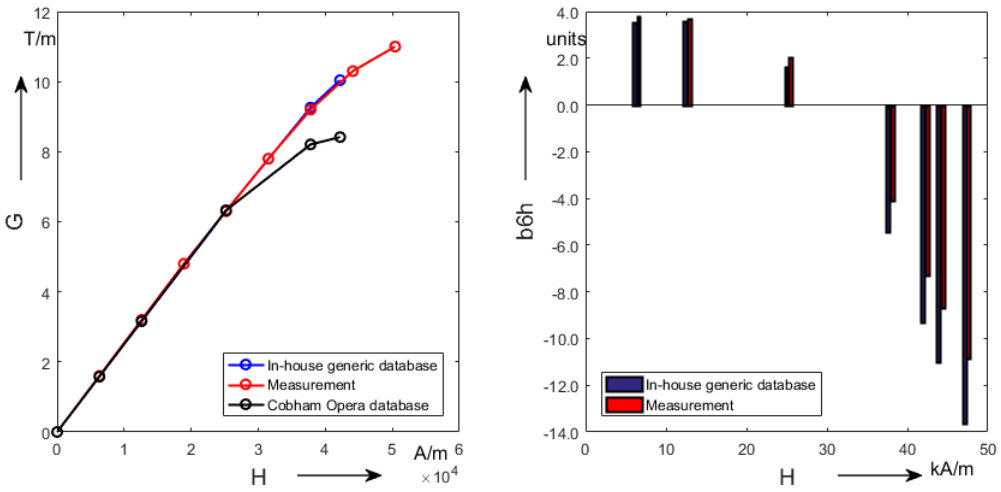

FIGURE 6.27: Flux density gradients inside the Q200 quadrupoles for the three cases under study (left) and 6^{th} harmonic values as function of the magnetomotive force (right).

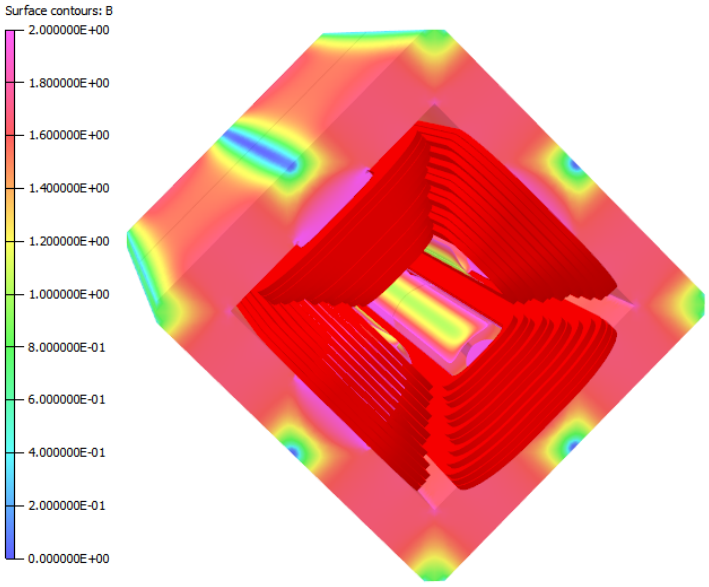

FIGURE 6.28: FE simulation of the Q200 quadrupoles of the East Are

In Fig. 6.27 (left), the gradient at the center of the magnet for all cases is compared with the gradient found by means of magnetic measurements on the magnet [93]. It can be seen that the simulation results of case (1) are very different compared with the results from the magnetic measurements. Therefore, it can be concluded that this B-H curve does not accurately represent the properties of the steel used for this magnet. On the other hand, the results of case (2) are consistent with the magnetic measurements.
In addition to the magnitude of the gradient it is important to guarantee also a good field quality. The field quality can be measured from the amplitude of the magnetic field harmonics. The integrated harmonics for the cases 2 and 3 are shown in Tab. 6.5 and Tab.6.6, while Fig. 6.27 (right) shows the normalized sixth harmonic b_6 as a function of the magnetic field. It can be seen that, as the magnetic field increases, there is a difference between the sixth harmonic for case (2) and the measurements (3). This because the b_6 is highly sensitive towards the saturation of the pole profile. This case study confirms the importance of having a reliable B-H curve during the design process to minimize the risk of designing a magnet that doesn't respect the field quality requirements.
In conclusion, five samples of different ferromagnetic materials were analyzed experimentally and compared with literature results. These materials have been (or will be) used for producing yokes for several normal-conductor magnets at CERN, such as REX-ISOLDE main dipole, ELENA dipole and quadrupole, and SESAME dipole. The comparison with literature shows several disagreements. The main one of them has been analyzed in detail in a case study based on finite element simulation of a quadrupole magnet installed in CERN. This analysis shows that a good knowledge of the yoke initial magnetization curve is essential to guarantee a given level of magnet performance, especially concerning its field quality.

TABLE 6.5: Simulation results on Q200 quadrupole magnet using CERN database BH curve

F_m [kA/m]	6.3	12.6	25.2	37.8	42.21	44.1	47.25
G [T/m]	1.5800	3.1645	6.3286	9.2684	10.0307	10.3137	10.7149
G_theo [T/m]	1.5834	3.1667	6.3335	9.5002	10.6085	11.0835	11.8752
L_mag [mm]	2103.61	2103.02	2097.83	2070.02	2060.61	2056.7	2052.2
nu[%]	99.8	99.9	99.9	97.6	94.6	93.05	90.23
G_int [T/m]	3.3237	6.6550	13.2762	19.1858	20.6694	21.2123	21.9895
b_6	3.8	3.7	2.0	-4.1	-7.3	-8.7	-13.6
b_{10}	-0.5	-0.6	-0.8	-1.7	-2.1	-2.2	-2.5
b_{14}	-0.2	-0.2	-0.2	-0.2	-0.2	-0.2	-0.2
b_{18}	0.0	0.0	0.0	0.0	0.0	0.0	0.0

TABLE 6.6: Simulation results on Q200 quadrupole magnet using measured BH curve

F_m [kA/m]	6.3	12.6	25.2	37.8	42.21	44.1	47.25
G [T/m]	1.5778	3.1609	6.3111	9.2596	10.0419	10.3348	10.7725
G_theo [T/m]	1.5834	3.1667	6.3335	9.5002	10.6085	11.0835	11.8752
L_mag [mm]	2103.31	2102.50	2071.9	2062.0	2097.42	2057.3	2047.0
nu[%]	99.7	99.8	99.6	97.47	94.66	93.24	90.71
G_int [T/m]	3.3187	6.6458	13.2370	19.1845	20.7065	21.2621	22.0514
b_6	3.5	3.6	1.6	-5.5	-9.3	-11.0	-13.6
b_{10}	-0.6	-0.6	-0.9	-1.9	-2.3	-2.6	-2.9
b_{14}	-0.3	-0.3	-0.3	-0.3	-0.3	-0.3	-0.3
b_{18}	-0.1	-0.1	-0.1	-0.1	-0.1	-0.1	-0.1

6.4 Conclusions

In this chapter, the proposed flux-metric systems described in Chapter 3 have been employed for characterizing ARMCO for magnet yokes and CRIOPHY for magnetic shields.

The magnetic properties ARMCO® Pure Iron, have been measured, within annealing treatment sequences from 750 °C to 850 °C, at operation temperatures of 4 K to 300 K. It is shown that annealing treatment improves the magnetic performance of the material, if the material is kept at room temperature. However, this

improvement disappears after cooling down the material to the operation conditions of 4 K. The dependency on the operation temperature was shown by testing the material at the cryogenic temperature of roughly 4 K, 77 K and at room temperature. The magnetic performance the material shown at room temperature have not been found at cryogenic temperatures. Nevertheless, the results obtained are still acceptable in comparison to the properties of the alternative materials. Tests performed before and after the application of a mechanical stress have also been studied to validate the production process.
The behavior of the material for much higher magnetic fields (8.6 to 11 T according to the field distribution in HL-LHC magnets) has been studied as well. The results present an initial magnetization and relative permeability curves up to nearly 450 A/m, the higher value of saturation being 2.82 T. A similar level of saturation is expected when the magnets are powered at their nominal current values. The properties of this material have been compared with the material used for the LHC magnet yokes and with similar material from ROXIE database. Significant discrepancies have been found, especially at a high level of saturation.
The effects of temperature and mechanical strain on Cryophy's magnetic properties have been studied in detail by employing the proposed flux-metric systems, proving the feasibility of its use as the cold magnetic shield material of the crab cavities cryomodule prototype. The results of the DC magnetic characterization showed a strong influence of temperature on Cryophy relative magnetic permeability. Experiments highlight a reduction of the relative permeability peak by a factor of two from room to cryogenic temperature, and then an extra variation of about one third when the temperature goes from 77 K to 4.2 K. Nevertheless, the relative magnetic permeability peak was found to be systematically higher than the magnetic shield design requirement of 100 000.
Finally, the importance of assessing the magnetic measurements of materials used for the construction of particle accelerator magnets has been discussed, investigating how different B-H curves could affect the results during the design of a magnet. This has been assessed using OPERA simulation of a quadrupole magnet installed in the CERN North Area. The case study showed that even similar B-H curves could cause significant differences in the magnet's field quality.

Chapter 7

Validation of the methods for weakly magnetic materials

In this chapter, the validation of the proposed flux-metric method extended to the characterization of weakly magnetic materials is illustrated. As a case study, the series production of co-wound 1.430 stainless steel tapes, the material used for the quench detection in ITER TF coils [123], is presented.
The validation of the novel magneto-metric based method for the open circuit magnetic characterization of very weakly magnetic materials is presented as well. As proof of principle and to assess the proposed method's accuracy, this approach will be applied to a reference alloy sample with a known relative magnetic permeability [73].

7.1 Prosed flux-metric based method

A challenging problem arises from the series production of stainless steel tapes: magnetic and paramagnetic materials exhibit different magnetic properties according to the production process (i.e. annealing and cold work). Consequently, samples of this material differently treated have to be characterized in order to find the optimal cold work and annealing able to minimize raising of magnetism. In the following, the novel approach specific for weakly magnetic material has been employed for measuring the magnetic properties of the series production co-wound stainless steel tapes for quench detection in ITER TF coils [19]. The aim has been to validate a time and cost-saving magnetic characterization within an acceptable uncertainty range.

7.1.1 Material and test specimen

Fifteen sample rolls of annealed 1.4310 steel tape, designed for the quench detection system of ITER TF coils and manufactured by Studer (CH) supplier of Streiffband (Herznach, Switzerland) were tested magnetically at CERN. These tests aim to assess the relative magnetic permeability $\boldsymbol{\mu}_r$ of the material, which is expected to be within the range $1 - 6$ in the solution annealed state, after one

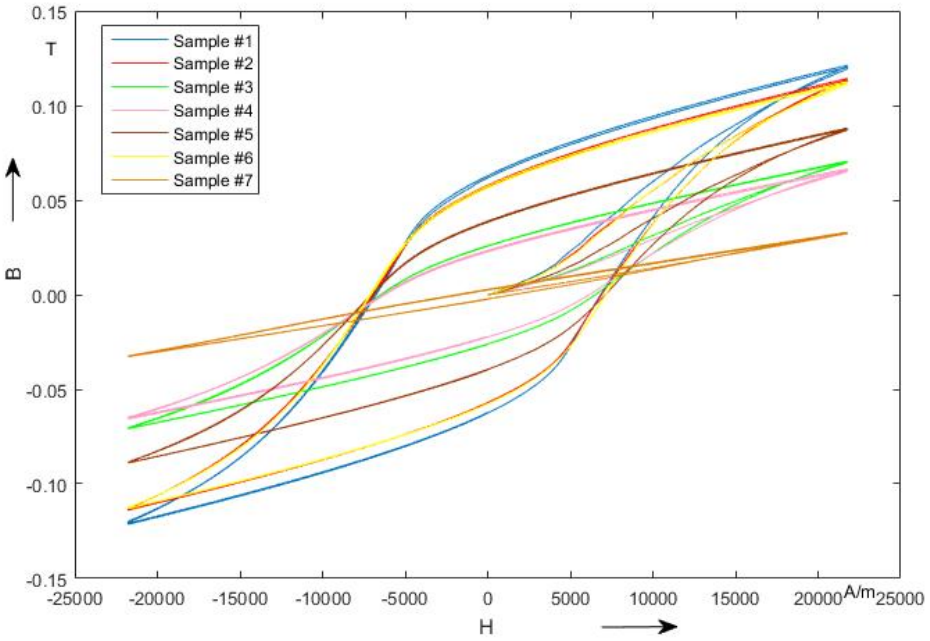

FIGURE 7.1: B-H curves for the first seven samples.

final skin pass. The final skin pass was introduced to improve the mechanical resistance as a trade-off between relatively high mechanical resistance and low relative magnetic permeability. The results of earlier tests made in 2014 on a roll of cold-worked 304 steel can be found in [33], while the results of a pre-production batch of annealed 304 and 316L austenitic steel are reported in [32].

The tape has a nominal width of 2.8 mm and a thickness of 0.05 mm. Upon request of CERN, the tape was rolled at Streiffband directly on a cardboard spool having a size compatible with the test equipment. With respect to the rolls used in 2014 [32], obtained by stripping manually the tape off the fabric at CERN, this method achieves a more uniform and compact roll geometry. Moreover, the quantity of material tested in each measurement is almost doubled, leading to higher signal levels and more accurate results.

7.1.2 Experimental results

For each one of the fifteen samples, the measured B-H hysteresis cycle and the computed $\mu_r(H)$ curves are plotted in Figs. 7.1-7.2, and 7.3-7.4, respectively. In the figures, only the part of the $\mu_r(H)$ curves where $\mu_r > 1$ are shown since the uncorrected component of the flux offset causes the term in $\frac{\phi}{H_0}$ to diverge as H_0 tends to 0. The summarized results are reported in Table 7.1, where columns 3, 4, 5, and 6, respectively, show i) the relative permeability peaks corresponding to a ramp-rate of 15 A/s, ii) the relative permeability peaks corresponding to a ramp-rate of 20 A/s, iii) the extrapolated peak value of μ_r, and (iv) the estimated error ought to the dynamic effects. Moreover, the value of H where the permeability peak occurs is reported in the second column. By analyzing the first four tapes,

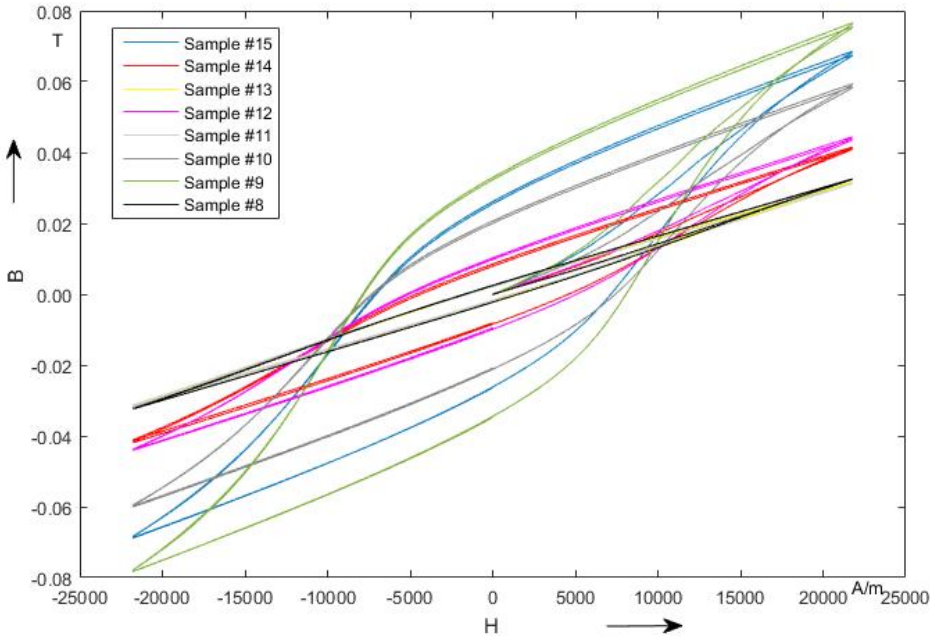

FIGURE 7.2: B-H curves for the last eight samples.

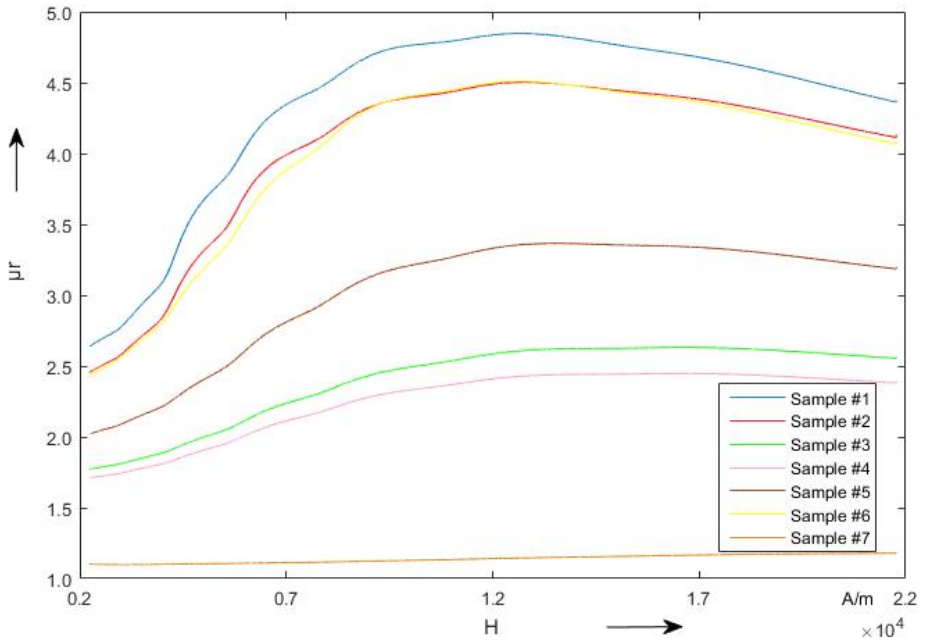

FIGURE 7.3: Relative permeability curves for the first seven samples.

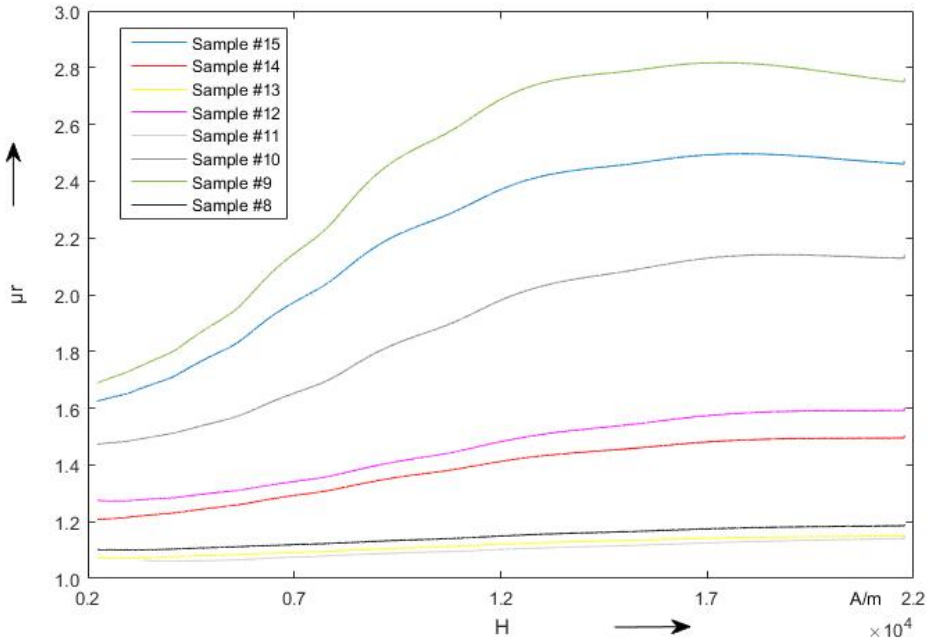

FIGURE 7.4: Relative permeability curves for the last eight samples.

it can be noticed that the first two samples exhibit a peak magnetic permeability roughly twice than the two last ones. This result was qualitatively confirmed by an independent test measuring the magnetic forces on 20 mm slivers cut off the rolls and exposed to a strong magnetic field. A difference in the hysteresis cycle shape is also evident in Fig. 7.1, which shows a higher squareness equivalent to a more pronounced maximum in the $\mu_r(H)$ curve, see Fig. 7.3. This results oriented the producer toward manufacturing the other samples analogous as for the third and fourth sample. The lowest obtained value is $\mu_r = 2.4$, higher than for pre-production annealed 1.4310 samples in 2014 (1.4 and 1.7). However, the present measurements take advantage of a better acquisition system and drift correction strategy. Therefore, the results might not be directly comparable with results obtained previously. In order to avoid any impact on the steel tape, from the sample number 5 the producer has not pulled the steel tape thought the measuring equipment. This brought to a lower magnetization of the sample number 7 and 8, with a relative permeability peak around 1.2. Neglecting the sample number 9, all the remaining samples showed a relative permeability value lower than 2.5, (see Fig. 7.4) matching the ITER requirements. Finally, it appears that the samples number 11 and 13, manufactured with a rougher tape, showed the lowest magnetization, with relative permeability peaks of 1.07 and 1.15, respectively. These results oriented the producer to choose this kind of tape for the successive test campaigns. An important aspect that remains to be assessed concerns the relevance of the present tests, maxing out at $H = 24$ kA/m, concerning the operating conditions of the tape that will range in the several MA/m. In the future, it would be worth introducing the following further improvements: i) take into account the radial dependence H(r) across the sample rolls, and ii) establish

TABLE 7.1: Sample roll test results

Sample #	H_{peak} [kA/m]	$RPP_{15A/m}$ [-]	$RPP_{20A/m}$ [-]	$\mu_r peak$ [-]	Error [%]
1	12.562	4.837	4.843	4.816	0.57
2	12.787	4.370	4.392	4.304	2.05
3	16.440	2.633	2.631	2.625	0.31
4	16.789	2.448	2.442	2.447	0.33
5	13.486	3.367	3.369	3.364	0.15
6	12.672	4.512	4.508	4.496	0.36
7	20.276	1.181	1.1785	1.171	0.85
8	20.340	1.184	1.770	1.156	2.42
9	17.050	2.817	2.798	2.741	2.77
10	18.689	2.140	2.127	2.088	2.49
11	21.771	1.142	1.131	1.076	4.86
12	21.771	1.592	1.587	1.572	1.27
13	21.771	1.1505	1.15	1.1485	0.17
14	21.770	1.496	1.494	1.488	0.40
15	17.808	2.497	2.483	2.441	2.24

a consistent pre-cycling procedure to evaluate and control the residual magnetic density B_r.
In conclusion, in this section, as a proof of principle, the proposed method was applied to the measurement of the magnetic properties of series production co-wound stainless steel tapes for quench detection in ITER TF coils. These results demonstrate the feasibility of this method for the characterization of material with a permeability between 1.0 and 6.0. However, the method has poor accuracy when the tested material has a permeability close to 1. This is mainly due to the extremely low SNR of the signal picked up by the sensing coil.

7.2 Proposed magneto-metric based method

In this section, the system architecture of the novel magneto-metric based method for the open circuit magnetic characterization of very weakly magnetic materials is illustrated. As proof of principle, this approach is applied to a reference alloy sample with a known relative magnetic permeability.

7.2.1 System architecture

The layout of the open circuit measurement system, hosted at CERN's magnetic measurement laboratory in Geneva, is shown in Fig. 7.5. It mainly consists of i) a reference dipole magnet (MCB22) able to generate a magnetic field up to 1 Tesla with uniformity better than $3 \cdot 10^{-4}$ over a volume of 1500 x 300 x 70 mm^3; ii) a

nuclear magnetic resonance teslameter (NMR - Metrolab PT2025) [101], sensitive to the norm of the vector flux density, with a precision of 0.1 parts per million (ppm) and an absolute accuracy of 5 ppm; and iii) a high-precision linear translation stage and a stage controller for moving the NMR with a relative accuracy of 1 ppm and recording the relative distance between two consecutive measurements. The overall measurement system is automatized using a suite of interactive programs developed in C++ using the framework FFMM (PC FFMM) [16].

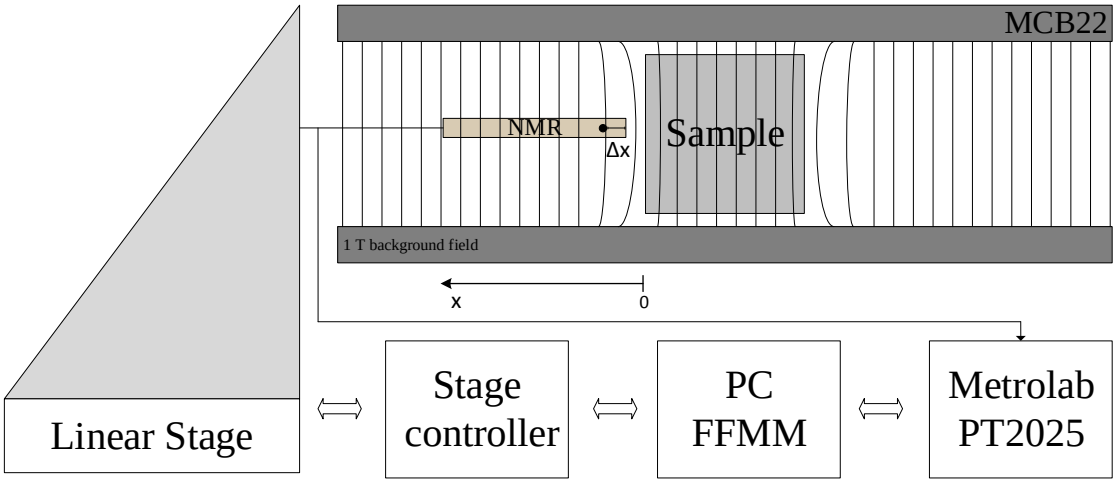

FIGURE 7.5: Measurement system layout.

7.2.2 Method validation by means of a reference sample

As proof of principle and to assess the proposed method's accuracy, this approach has been applied to a reference alloy sample with a known relative magnetic permeability [73]. The results of the magnetic material identification are presented and discussed in the following sections.

Magnetic measurements

Fig. 7.6 shows the results of the local magnetic measurements. In particular, the flux density generated from the dipole magnet in the case of perturbation due to the presence of the reference sample SN643 and in the absence of sample (measurement of the background field), are presented. The perturbation decays asymptotically as the inverse of the distance cubed, as expected for the far field of an elementary magnetic dipole perturbation.

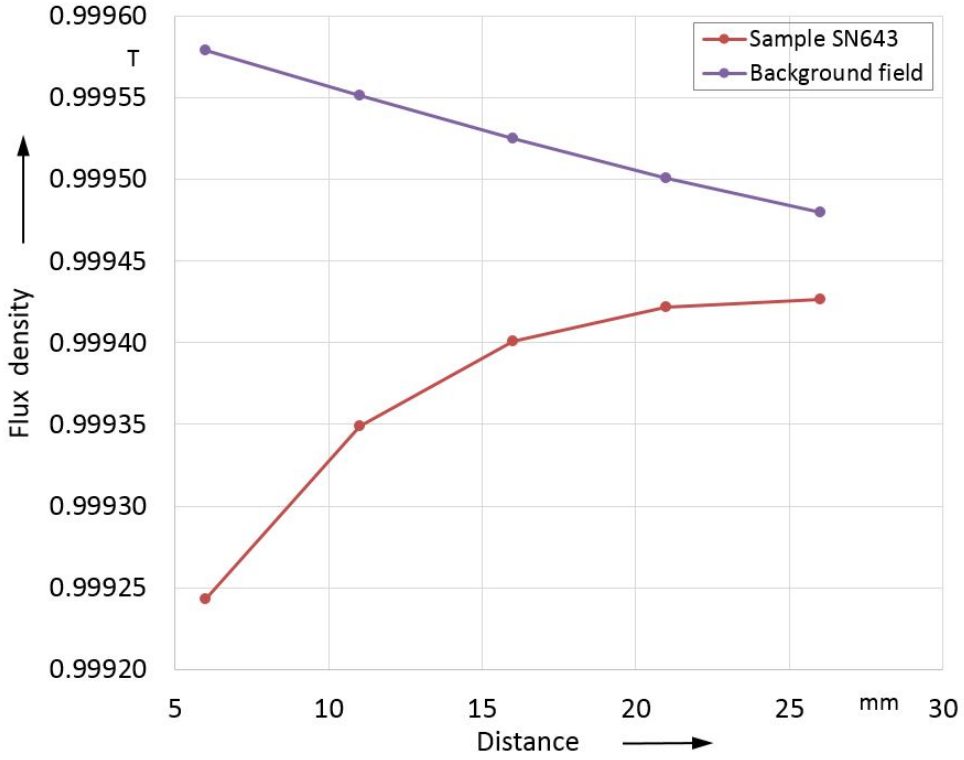

FIGURE 7.6: Magnetic measurements results

Relative magnetic permeability identification

The results of the inverse problem formulation are summarized in Table 7.2. The calculation is based on comparing measured with simulated data using a Levenberg-Marquardt algorithm in Matlab. A good correspondence between the

TABLE 7.2: Magnetic relative permeability identification

	Reference μ_r [-]	**Estimation** μ_r [-]	Δx [mm]
$C1$	1.00384 ± 0.00031	1.00396	-
$C2$	1.00384 ± 0.00031	1.00392	-0.017

estimated and reference permeability is observed: both estimated values lie in the uncertainty range of the reference value. The smallest error is given unsurprisingly by case 2, which includes an additional parameter into the fit. $C2$ tries to recover the distances sample-sensor at which the local magnetic measurements are performed assuming that all the distances are affected by the same offset. This is consistent with the fact that the actual position of the probe inside the sensor is known with an uncertainty of 1 mm, while the relative distance between two measurements is known with an uncertainty of 10^{-3} mm. Further work with different reference samples is required in order to assess whether this formulation is well-posed or not.

7.3 Conclusions

In this chapter, the unknown magnetic properties of the ITER TF coils quench detection stainless steel have been analyzed utilizing the proposed flux-metric method for weakly magnetic materials. The tests have been helpful to the producer to identify the best annealing and cold work for achieving the lowest material magnetization. This is an essential requirement of the quench detection system, considering the extremely high field working conditions.
Moreover, the magneto-metric method proposed in this dissertation for weakly magnetic materials with a relative magnetic permeability μ_r less than 1.05 has been validated employing a reference sample. The case study shows good agreement between the estimated relative magnetic permeability and the reference value of the sample: the accuracy of the proposed method is better than 3% for the susceptibility. This method, while still time-consuming at this stage, has been found to be effective for the difficult problem posed by weakly magnetic materials. In view of future series test campaigns, its efficiency could be improved by standardizing the setup and the shape of the sample.

Chapter 8

Validation of the proposed magnetic axis monitoring method

In this chapter, the proposed Hall sensors-based method for the real-time monitoring of single-coil solenoids is validated with a case study on a model of a multi-coil solenoid. The measurement uncertainty and optimizing the placement of the Hall transducers are assessed as well.
Furthermore, for validating the proposed method for multi-coil solenoids, the requirements of the European project ELI-NP are taken into account as a case study, and the field model is discussed. In particular, an uncertainty analysis is carried out for minimizing the uncertainty in measuring the multi-coil solenoid magnetic axis. Then, the results of simulations based on both analytical and finite-element models of the ELI-NP multi-coil solenoid are reported, in order to validate the method numerically.

8.1 Proof of principle for a single-coil solenoid

The proposed method for monitoring the solenoid axis misalignment is summarized by (5.19) and (5.21) when employing radially- or axially-placed uniaxial Hall transducers, respectively. The measurement procedure is summed up as follows:
At installation:

- Place the transducers by defining R_0 and d;
- Obtain the needed field components and derivatives at $(R_0, -d/2)$ and $(R_0, +d/2)$ in the solenoid reference system;

In operation:

- Measure B_m at the Hall transducers points;
- Compute $x_{O'}$, $y_{O'}$, v_1, and v_2;
- Compute the related uncertainties.

The parameters defining the magnetic axis misalignment depend on the longitudinal and radial positions of the transducers (R_0 and d), as well as on the specific longitudinal and radial field profile of the solenoid (represented by the field derivatives). Therefore, the transducers must be placed by taking into account that different positions can lead to a different uncertainty of the final result. Moreover, the misalignment parameters depend on the field profile, therefore, in general, optimal placement of the transducers cannot be found. Instead, the optimization must be carried out by evaluating the uncertainty for the specific solenoid according to its field.
This optimization procedure is highlighted by two case studies presented in this section, referring to two different models of a single coil of the multi-coil magnet to be employed in the ELI-NP project [47]. First, an analytical model for the single solenoid is considered, obtained from the geometries of a single coil of the ELI-NP magnet. Then, a FE model of the coil was obtained from the FEM of the multi-coil solenoid as a whole, by extracting the field of one of the coils.
Details about the employed field models are discussed in the next subsection. Then, the uncertainty is assessed and the optimal placement of the transducers is determined. Finally, simulations proving the effectiveness of the method in identifying the misalignment axis are reported.

8.1.1 Field models

Analytical model

A multi–solenoid made of 12 identical coils (the ELI-NP solenoid type B) was tested at the manufacturer (Danfysik) facility in 2015. In this section, an analytical model of one of the coils of the magnet is considered. Among the models proposed in the scientific literature, a model of 2009 from MIT and the Community College of Vermont [42] is taken into account. This model is based on a generalized elliptic integral that is easily computable with a fast numerical algorithm, and it allows to calculate the magnetic flux density of a single layer solenoid. In particular, the solenoid was modeled in MATLAB with geometrical parameters such as the number of turns (N), the length (L), the aperture radius (R), and the operating current (I_{op}). The field of a multi-layer solenoid can be also simulated as a superposition of single layer solenoids with increasing aperture radius. Fig. 8.1 shows B_r and B_z at the plane $y = 0$ for $x \in [-R; +R]$ and $z \in [-L; +L]$. Due to the axisymmetry, the field for half a plane would be enough, but the entire plane is shown for clarity. The solenoid model has 12 layers, 9 turns per layer, length equal to 93 mm, aperture radius equal to 153,1 mm, and operating current I_{op} = 177 A. Such parameters were chosen according to the characteristics of a single coil of the ELI-NP type B solenoid. In Fig. **??**, the section at $y = 0$ of the solenoid is also shown as a rectangle under the surface representing the field components, to highlight the solenoid dimensions better.

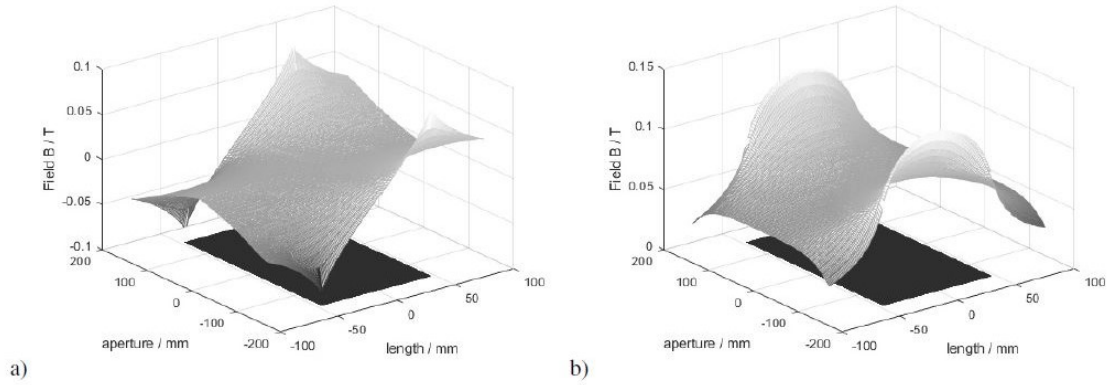

FIGURE 8.1: Radial (a) and axial (b) components of B for a multi-layer solenoid at the plane $y = 0$ calculated with an analytical model based on a generalized elliptic integral.

Numerical model

During the factory acceptance test (F.A.T.) of the ELI-NP multi-solenoid Type B, several magnetic, electrical, and hydraulic measurements have been performed, including a magnetic flux density mapping along several paths for two configurations: (i) by powering all the coils with the same current polarity ($++++$ configuration), and (ii) by alternating the current polarity for each coil triplet ($++--$ configuration). However, for both the configurations, only the longitudinal component of the flux density (B_z) was measured, so such measurements were not used directly to assess the derivatives needed for the measurement methods, because also the radial flux density would be required. Conversely, a FEM model was exploited and the longitudinal component output from the FEM was compared with the measured data.
A finite element analysis (F.E.A.) of the ELI-NP multi-solenoid type B was performed using Poisson Superfish software, in order to map the flux density generated by the twelve solenoid coils operating in DC. The simulation is a 2D model of the magnet with cylindrical symmetry, where all the coils and iron yoke dimensions were obtained by mechanical drawings and dimensional tests supplied by Danfysik. Each coil, composed by 108 turns, was powered with the nominal current of 177 A reaching an Ampere·Turns value of 19.116 A. The iron yoke material was modeled with a 17-4 ph stainless steel first magnetization curve. It is a mild steel, approximating the original iron yoke material (steel 37) satisfyingly. The output of the simulation is a field map of the radial and axial flux density components B_r and B_z, assessed in the inner aperture coil air region, with a corresponding step of 2 mm and 1 mm, respectively. Also, all the derivatives of B_z and B_r in radial and longitudinal direction were included in the output files.
The measured B_z component measured during the F.A.T. was compared with the B_z calculated through the simulations. As shown in Fig. 8.2, excluding the ends part of the fringe fields, the curves matched significantly within 2%. This error is negligible with respect to the measured and the simulated total integral field, over several trajectories at a different radius from the mechanical axis (Table 8.1).

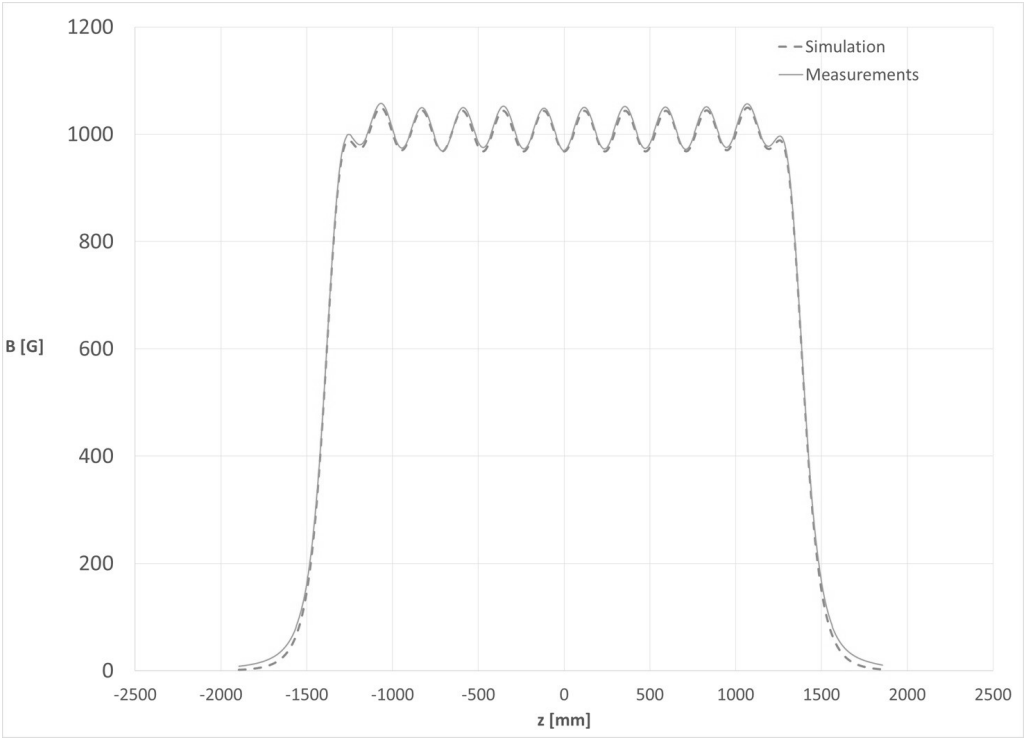

FIGURE 8.2: Simulated and Measured Longitudinal Component of the Magnetic Field along the magnet axis.

	Simulated Field integral [T·mm]	Measured Field integral [T·mm]	Δ Field Integral [%]
$R = 0$ mm	287.7348	284.3833	1.2
$R = 30$ mm	287.7259	284.3843	1.2
$R = 60$ mm	287.7341	284.3871	1.2
$R = 90$ mm	287.8302	284.3914	1.2
$R = 120$ mm	287.9348	284.4397	1.2

TABLE 8.1: Comparison between Simulated and Measured Field Integral.

By relying on the same magnet model, only one coil per time can be supplied in order to obtain the field irradiated by a single solenoid. In Fig. 8.3, the coil considered for the FEM model is highlighted. This is the third of the first triplet and the field was simulated in the spatial region also highlighted in a lighter gray. The results of this simulation were employed for optimizing the transducers placement and validating the method.

8.1.2 Uncertainty assessment

The uncertainties of the O' coordinates, v_1, and v_2 were assessed by considering their explicit expressions, obtained by exploiting the symmetries of the magnetic

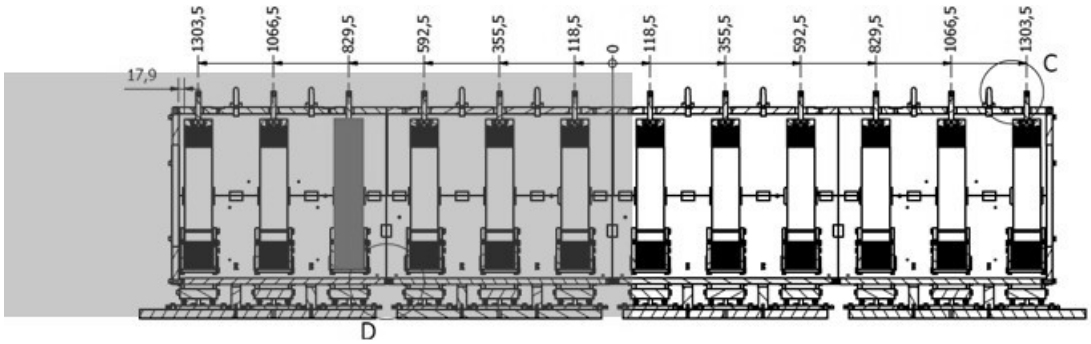

FIGURE 8.3: Geometry of the ELI-NP multi-coil magnet. The coil supplied for the single solenoid model simulation is highlighted (gray) together with the spatial region of interest for the FEM (light gray).

flux density irradiated by the solenoid. In particular, the (5.20) and (5.22) have to be considered, for radial and axial Hall transducers, respectively. The uncertainty was computed by using the "law of propagation of the uncertainties" (LPU) for each equation. For the sake of brevity, only $x_{O'}$ and v_1 for radial transducers are here considered, but the same reasoning can be applied for $y_{o'}$ and v_2, and for axial transducers. The squared standard uncertainties are:

$$
\begin{aligned}
u_{x_{O'}}^2 &= \frac{u_B^2}{4\left(\frac{\partial B_r}{\partial r}\Big|_0\right)^2} + \left(\frac{x_{o'}}{\frac{\partial B_r}{\partial r}\Big|_0}\right)^2 u_\partial^2 \\
u_{v_1}^2 &= \frac{u_B^2}{\left(\frac{\partial B_r}{\partial r}\Big|_0 - 2\frac{R_0}{d}\,\frac{\partial B_r}{\partial z}\Big|_0 - 2\frac{B_{z0}}{d}\right)^2} + \\
&+ \left(\frac{v_1}{\frac{\partial B_r}{\partial r}\Big|_0 - 2\frac{R_0}{d}\,\frac{\partial B_r}{\partial z}\Big|_0 - 2\frac{B_{z0}}{d}}\right)^2 \left[\left(1 + 4\frac{R_0^2}{d^2}\right) u_\partial^2 + \frac{4}{d^2} u_f^2\right] + \\
&+ \left(\frac{v_1}{\frac{\partial B_r}{\partial r}\Big|_0 - 2\frac{R_0}{d}\,\frac{\partial B_r}{\partial z}\Big|_0 - 2\frac{B_{z0}}{d}}\right)^2 \left[4\left(\frac{B_{z0}}{d^2} + \frac{R_0}{d^2}\,\frac{\partial B_r}{\partial z}\Big|_0\right)^2 + \frac{4}{d^2}\,\frac{\partial B_r}{\partial z}\Big|_0^2\right] u_g^2
\end{aligned}
\tag{8.1}
$$

where, u_B is the uncertainty of the values measured by the transducers, supposed equal for all the transducers outputs; u_g is the uncertainty related to the transducers placing, supposed equal for both geometrical parameters, R_0 and d; u_∂ is the uncertainty of the derivatives of B_r, and u_f is the uncertainty of the B_{z0} value. The last contributions arise from the field model, and they express the goodness of fitting with respect to the measured field. Once the above uncertainties are known, $u_{x_{O'}}$ and u_{v_1} are expressed as a function of (R_0, d) in order to find the optimal placement.

Assuming typical values of $u_B \approx 10^{-4}$ T for Hall transducers and $u_{R0} \approx u_d = u_g \approx 10^{-5}$ m, in a placement by laser tracking. Moreover, considerations about the field model suggest that derivatives and field components uncertainties are in the order of percents of their respective values.

To have a better understanding of the contributions to the total uncertainty, it

is possible to demonstrate that the uncertainty related to the placement parameters is negligible with respect to that of the field measurements, under the above assumptions. This can be understood by noticing that:

$$\left(1+4\frac{R_0^2}{d^2}\right)u_\partial^2+\frac{4}{d^2}u_f^2 \gg 4\left(\frac{B_{z0}}{d^2}+\frac{R_0}{d^2}\left.\frac{\partial B_r}{\partial z}\right|_0\right)^2 u_g^2+\frac{4}{d^2}\left.\frac{\partial B_r}{\partial z}\right|_0^2 u_g^2. \tag{8.2}$$

According to the adopted field values, in fact, the derivatives values are of the order of 1 T/m, B_{z0} is about 0.06 T in the points of interest, and $u_g \approx 10^{-5}$ m. For the considered solenoid, therefore, the second term is in the order of 10^{-4} m. Given the values of the derivatives and B_{z0}, $u_\partial \approx 10^{-2}$ T/m, while $u_f \approx 10^{-3}$ T, when the relative uncertainties arising from the field model are within the order of percent. Moreover, the contribution related to u_∂ is dominant at the first member, because u_f is an order of magnitude below, while their coefficients are of the same order. Finally, the coordinates of O' and the values of v_1 (and v_2) are below 1 mm for a small misalignment. Thus, considering only the uncertainty contributions of u_B and u_∂, (8.1) can be rewritten as:

$$\begin{aligned} u_{xo'}^2 &\approx \frac{u_B^2}{4\left(\left.\frac{\partial B_r}{\partial r}\right|_0\right)^2} \\ u_{v1}^2 &\approx \frac{u_B^2+v_1^2\left(1+4\frac{R_0^2}{d^2}\right)u_\partial^2}{\left(\left.\frac{\partial B_r}{\partial r}\right|_0-2\frac{R_0}{d}\left.\frac{\partial B_r}{\partial z}\right|_0-2\frac{B_{z0}}{d}\right)^2} \end{aligned} \tag{8.3}$$

The uncertainty minimization is hence limited by the Hall transducers technology, even if this can be mitigated by the transducers placement (minimization of the denominators).

As an example, when monitoring the solenoid magnetic axis, there could be interest in the point $(x_{O_2'}, y_{O_2'}, z_{O_2'}) = (x_{O'}+v_1/2, y_{O'}+v_2/2, +d/2)$, and one of the uncertainties of interest would be:

$$u_{x_{O_2'}} = \sqrt{u_{x_{O'}}^2+\frac{u_{v1}^2}{4}} \tag{8.4}$$

The values of this uncertainty as a function of (R_0, d) are shown in Fig. 8.4, when employing the analytical model or the FEM. The minimum is obtained when R_0 is the 90% of the aperture, and d equals about the 90% of the solenoid length for both cases, thus the transducers have to be placed slightly inside the magnet aperture to minimize $u_{x_{O_2'}}$. Similar considerations stand for $u_{y_{O_2'}}$ and the optimal placement could aim to minimize both the uncertainties separately, or their combination.

8.1.3 Simulation Results

Once fixed R_0 and d, the effectiveness of the proposed method can be proved by simulation, through either the analytical or FE field model. A known misalignment is imposed in order to calculate the reference quantities identifying

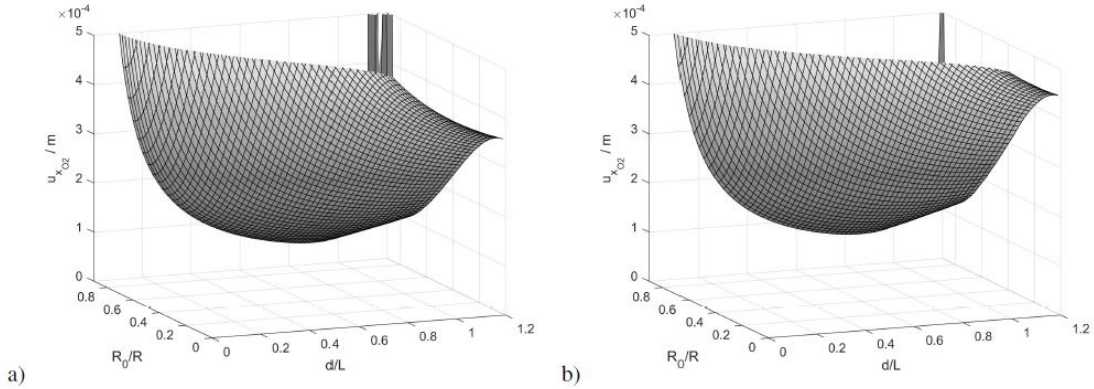

FIGURE 8.4: Uncertainty of the "x" coordinate of O_2' for the case of radially placed Hall transducers, calculated with the analytical model (a) and with the FEM model (b).

the magnetic axis (reference values of O', v_1, and v_2). Then, these quantities are estimated by the equations of the method, and a corresponding uncertainty can be assessed. In the simulation, the misalignment is implemented with a rotation and then a translation of the solenoid. When employing the analytical field model and the misaligned magnetic axis is rotated of angles up to $\pi/1000$ and translated of 1/1000 times the solenoid length, simulation results show that the estimated error is always below 10^{-7} m. These are reasonable maximum misalignments in the cases of interest. When employing the FE model, taking into account the same misalignment, the uncertainty is higher but always below 10^{-6} m.

8.2 Proof of principle for a multi-coils solenoid

The method for the magnetic axis monitoring proposed in Section 5.2 for multi-coil solenoids was validated numerically on a case study related to the Solenoid B of the project ELI-NP [47], a multi-coil magnet made of 12 coils, whose magnetic axes overlap in the aligned case. As for the single-coil, two magnetic flux density models were adopted during the simulations, namely an analytical and a finite-element model. The latter matches the field component B_z measured by the manufacturer Danfysik. The 12 coils are assumed as equal both for the analytical and FEM model of the magnet, in accordance with the data extracted from the datasheet of the ELI-NP Solenoid B.
The method can be applied if (i) the magnet is misaligned according to a piecewise axisymmetry, and (ii) the magnetic flux density equals the superposition of the fields irradiated by the N coils (*superposition property*). Indeed, the superposition is trivially verified for the field analytical model, because this model is precisely obtained by summing the radial and axial field components at all the points of interest, taking into account the fields irradiated by each coil. Conversely, the FEM model was obtained by a CAD. The field obtained with the FEM could differ from the analytical model, owing to effects that are not considered in superimposing the field of the coils, for example, mutual coupling between the

coils or because of magnetic shields. In magnet design, magnetic shields are often employed (i) to limit fringe flux, and (ii) to reduce the number of ampere-turns for a given focal length. However, the shield introduces a disruption in the magnetic flux density, such that the superposition principle is not applicable. This was confirmed through the following procedure:

1. A FEM simulation of the multi-coil magnet as a whole was carried out, and the B_r and B_z were extracted. The FEM model is such that the B_z values match the measurements on the actual magnet provided by the manufacturer.

2. A FEM simulation of a single coil of the magnet allows one to extract its individual field components too. Thus, the field of an ideal N-coil magnet was obtained shifting properly the field configuration of the single coil and then summing the obtained field values for each of the spatial points of interest.

3. This field, which surely satisfies the superposition property, was compared with the previous multi-coil FEM model. The results pointed out an error not negligible at all, especially at the magnet ends. The cause of this error was attributed to the magnetic shield.

4. To verify this hypothesis, another FEM simulation was carried out without the magnetic shield. An error much lower, compatible with the FEM residual numerical error, was obtained. Therefore, the superposition property is verified for the ELI-NP multi-coil magnet without the shield.

Hence, for the rest of the dissertation, for the sake of the simplicity, the ELI Solenoid B is considered without the magnetic shield. The case with the shield can be treated analogously, provided that the fields of the first and the last coil are properly modified, taking into account the distortion caused by the shield. In the following, further details on the field models are reported.

8.2.1 Field models

As already done in the previous section for a single multi-layer coil, the analytical model is based on a generalized elliptic integral [42], with proper extensions to the multi-coil case. The magnet aperture radius equals $153.1\,\mathrm{mm}$ and its length is $2770\,\mathrm{mm}$. Fig. 8.5 shows B_r and B_z at the plane $y = 0$ for the spatial region of interest. To visualize the field configuration, it is enough to plot only the values for $y = 0$ due to the axisymmetry.

The FEM simulation was performed by the field solver Poisson Superfish, with steps along the magnet aperture and length of $1.0\,\mathrm{mm}$ and $0.5\,\mathrm{mm}$, respectively. In the FEM model, Dirichlet boundary conditions are imposed on all the four sides of the rectangular background. With the aim of properly placing the background sides, several simulations have been run to avoid introducing any error into the field at magnet ends while optimizing the processing speed. The distance between both the end plates of the iron and the background sides normal

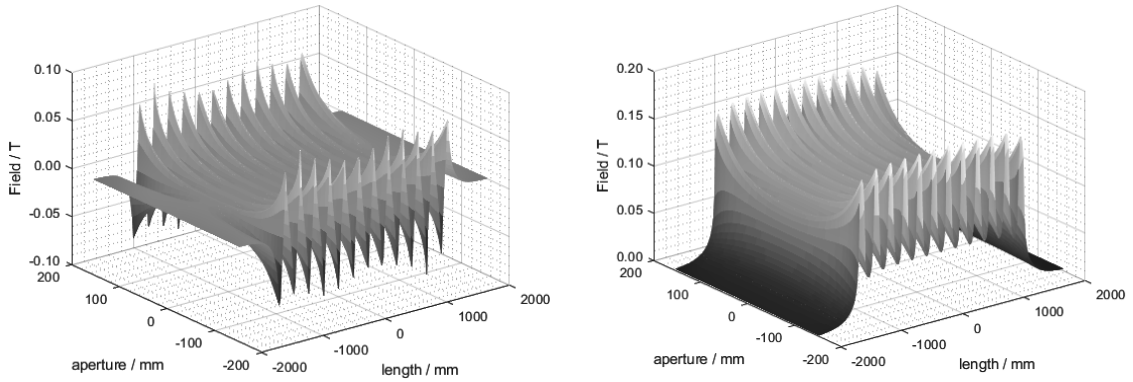

(A) (B)

FIGURE 8.5: Radial (a) and axial (b) components of B at the plane $y = 0$ for the ELI-NP multi-coil Solenoid type B (analytical model based on a generalized elliptic integral).

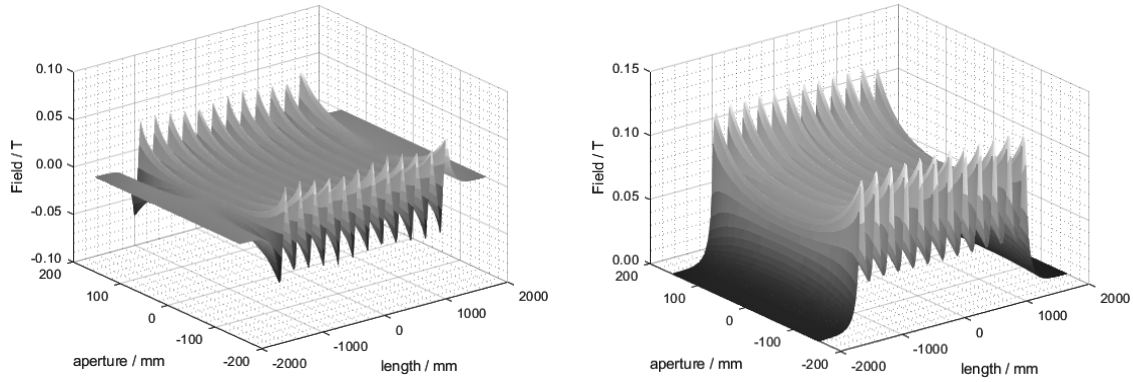

(A) (B)

FIGURE 8.6: Radial (a) and axial (b) components of B at the plane $y = 0$ for the ELI-NP multi-coil Solenoid type B (FEM simulation by Poisson Superfish).

to the magnet axis, is more than $1200\,\mathrm{mm}$, while the side parallels to the magnet axis is displaced at $100\,\mathrm{mm}$ over the iron. By several simulations, we verified that increasing these distances does not affect the results. The output of the simulation is again a field map of the radial and axial flux density components B_r and B_z, together with their radial and axial derivatives. In Figs. 8.6, the resulting radial (a) and axial (b) components of B are shown at the plane $y = 0$, for a multi-coil solenoid without magnetic shield. The impact of the magnetic shield is highlighted in Figs. 8.7, where the B_z behavior is compared with the shield (a) and without (b), as seen from the side of the magnet. Some peaks at the end of the magnet arise with the magnetic shield. Without the shield, the field is less limited at the fringe zones and, for the same operating current, is less intense.

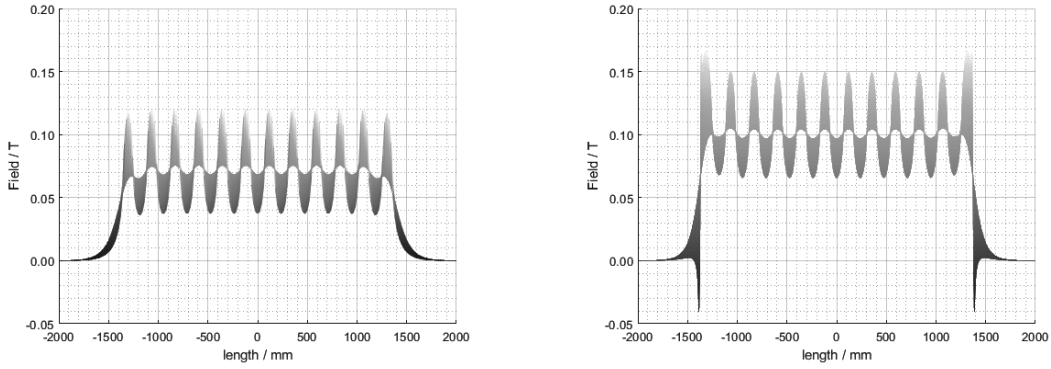

(A) (B)

FIGURE 8.7: B_z behavior at $y = 0$, seen from the magnet side, for a magnet without (a) and with magnetic shield (b).

8.2.2 Uncertainty assessment

The system of equations (5.27)-(5.28) can be written as:

$$\mathrm{A}\mathbf{x} = \mathbf{B} \tag{8.5}$$

with:

$$\mathbf{x} = \begin{bmatrix} x_{O'_{0,1}} \\ y_{O'_{0,1}} \\ v_{x,1} \\ v_{y,1} \\ \dots \\ x_{O'_{0,N}} \\ y_{O'_{0,N}} \\ v_{x,N} \\ v_{y,N} \end{bmatrix}, \qquad \mathbf{B} = \begin{bmatrix} B_m(H_{13}) - B_m(H_{11}) \\ B_m(H_{14}) - B_m(H_{12}) \\ B_m(H_{23}) - B_m(H_{21}) \\ B_m(H_{24}) - B_m(H_{22}) \\ \dots \\ B_m(H_{2N-1,3}) - B_m(H_{2N-1,1}) \\ B_m(H_{2N-1,4}) - B_m(H_{2N-1,2}) \\ B_m(H_{2N,3}) - B_m(H_{2N,1}) \\ B_m(H_{2N,4}) - B_m(H_{2N,2}) \end{bmatrix}, \tag{8.6}$$

where, A is a $4N \times 4N$ matrix, $\mathbf{B}$ is an array of $4N$ terms obtained as the difference between couples of measured field values, and $\mathbf{x}$ is the array of the unknowns. This linear system is easy to be solved numerically, but an analytical expression for $\mathbf{x}$ cannot be obtained just as easily. For this reason, the law of propagation of the uncertainties (LPU) cannot be applied directly to an explicit expression of $\mathbf{x}$. The measurement procedure consists of two main steps: *At installation:*

- Place the transducers at both sides of each coil, defining R_0 and d;
- Obtain the needed field components and derivatives at $(R_0, -d/2)$ and $(R_0, +d/2)$ in each coil reference system;

In operation:

- Measure B_m at the Hall transducers points;
- Compute $\mathbf{x} = \mathrm{A}^{-1}\mathbf{B} = \mathrm{I}\mathbf{B}$;

- Compute the related uncertainties.

The distance d between the transducers planes is equal for all the planes couples, and the distance R_0 of a transducer from the aligned magnetic axis is equal for all the $8N$ transducers. Furthermore, the field data needed for the calculation of A is related to the FE model of a single coil of the magnet. Namely, the field components and derivatives at the starting points are not derived from the multi-coil field model, but from the model of one of the N coils. The optimal placing is determined by an uncertainty analysis.

The contributions to the total uncertainty derive from the measurement, the field model, and the transducers placement (geometrical parameters R_0 and d). This last contribution can be neglected by assuming a placement by laser tracking. Let us recall the general LPU expression to adopt when the quantities contributing to the uncertainty are not correlated [48]:

$$\begin{aligned}\mathbf{u}_{\mathbf{x}}^2 = \sum_i \left(\frac{\partial \mathbf{x}}{\partial c_i}\right)^2 u_{c_i}^2 = \Gamma + \Delta = \sum_{h=1}^{2N}\sum_{k=1}^{4}\left(\frac{\partial \mathbf{x}}{\partial B_{hk}}\right)^2 u_{B_{hk}}^2 + \\ + \sum_{j=1}^{N}\left[\left(\frac{\partial \mathbf{x}}{\partial c_{r_j}}\right)^2 u_{\partial r_j}^2 + \left(\frac{\partial \mathbf{x}}{\partial c_{z_j}}\right)^2 u_{\partial z_j}^2 + \left(\frac{\partial \mathbf{x}}{\partial c_{f_j}}\right)^2 u_{f_j}^2\right]\end{aligned} \tag{8.7}$$

Expression (8.7) means that the LPU has to be applied for each component of $\mathbf{x}$. $\mathbf{u_x}$ is an array of uncertainties, and c_i is a generic contribution to the uncertainty. In the present case, this can be one of the $B_{hk} = B_m(H_{hk})$, which are $8N$ different measurements, or one of the $3N$ field data (2 derivatives and 1 field value per plane). The field data related to the odd number planes can be led back to the even number planes data. Thus only $3N$ different values appearing in the matrix A have to be considered. The equation shows that the total uncertainty is a combination of several components, calculated independently, where the sensitivity coefficients are obtained deriving with respect to each contribution c_i. This uncertainty can be seen as the sum of two terms, Γ and Δ. The first term, Γ, groups the uncertainties associated to the measured field values, while the second term, Δ, contains the field model uncertainties associated to the field derivatives, $u_{\partial r_j}$ and $u_{\partial z_j}$, and the field values, u_{f_j}. These terms are here considered separately. Referring to (8.5), it can be observed that the measured field values B_{hk} are only contained in the array $\mathbf{B}$. Therefore, it is easy to demonstrate that the related contribution is equal to:

$$\mathbf{u}_{\mathbf{x}B}^2 = 2\sum_j \left(\mathbf{I^j}\right)^2 u_H^2 \tag{8.8}$$

where $\mathbf{I^j}$ is the j-th column of the inverse matrix $\mathrm{I} = \mathrm{A}^{-1}$, and u_H is the uncertainty associated to a single measurement, supposed equal for all the Hall transducers. Considering the term Δ, by differentiating (8.5), the following expression can be obtained:

$$\begin{aligned} \frac{\partial(\mathrm{A}\mathbf{x})}{\partial c_i} = \frac{\partial \mathrm{A}}{\partial c_i}\mathbf{x} + \mathrm{A}\frac{\partial \mathbf{x}}{\partial c_i} = \frac{\partial \mathbf{B}}{\partial c_i} = \mathbf{0} \Rightarrow \\ \Rightarrow \frac{\partial \mathbf{x}}{\partial c_i} = -\mathrm{A}^{-1}\left(\frac{\partial \mathrm{A}}{\partial c_i}\mathbf{x}\right) = -\mathrm{A}^{-1}\left[\frac{\partial \mathrm{A}}{\partial c_i}\left(\mathrm{A}^{-1}\mathbf{B}\right)\right] \end{aligned} \tag{8.9}$$

In particular, this can be used to calculate the contribution from the derivatives and field values extracted from the field model. The derivative applied to a matrix, or more generally to an array, corresponds to the derivation of all its elements. For a generic contribution c_i, after the matrix derivative is calculated, it is easy to obtain the LPU coefficient simply following eq. (8.9). Then, a simple algorithm can be implemented to calculate the total measurement uncertainty.

8.2.3 Simulation Results

The above LPU expression was exploited to minimize the measurement uncertainty at varying the transducers placement. The results of the simulations are reported in the following.
The uncertainty in the magnetic axis identification was computed by considering initially a point of interest, belonging to the axis: $(x_{O'_2}, y_{O'_2}, z_{O'_2}) = (x_{O'} + v_x/2, y_{O'} + v_y/2, +d/2)$. The uncertainty related to one of the coordinates is expressed, for example, by eq. (8.10):

$$u_{y_{O'_2}} = \sqrt{u^2_{y_{O'}} + \frac{u^2_{v_y}}{4}} \tag{8.10}$$

where $u_{y_{O'}}$ and u_{v_y} are elements of the array of uncertainties $\mathbf{u_x}$ of eq. (8.7). In there, the uncertainty of the transducers is supposed to equal, and it is $u_B \approx 10^{-4}\,\mathrm{T}$. The uncertainty of the placement, supposed equal for R_0 and d, is $u_g \approx 10^{-5}\,\mathrm{m}$ when using laser tracking, thus, these contributions are neglected. Then, the contributions arising from the field model are u_∂ and u_f: these are the uncertainty of the derivatives of $B_{r,i}$ and $B_{z,i}$, respectively. Both of them express the goodness of fitting of the field model concerning the measured field. Taking also into account the derivatives and field values, it can be said that, for the considered solenoid field model, $u_\partial \approx 10^{-2}\,\mathrm{T\,m^{-1}}$, while $u_f \approx 10^{-3}\,\mathrm{T}$.
Actually, the uncertainty expression (8.10) has to be calculated for the N coils, in order to understand if the optimum is found for the same (R_0,d) point. After some simulations, however, the optimal placing of the N planes couples is approximatively the same for all the N coils. This optimum corresponds to R_0 equal about to the $90\,\%$ of the aperture, and d equals about $75\,\%$ of the coil length L, considering the planes placing for each coil relative to the coil reference system. The uncertainty of $y_{O2'}$ is reported in Fig. 8.8 for one of the coils.

Finally, the difference between the axis parameters obtained by applying a known misalignment (*reference parameters*), and the same parameters calculated with the presented method, is estimated numerically. In applying the method, the optimal transducers placement is exploited. The difference from the reference parameters

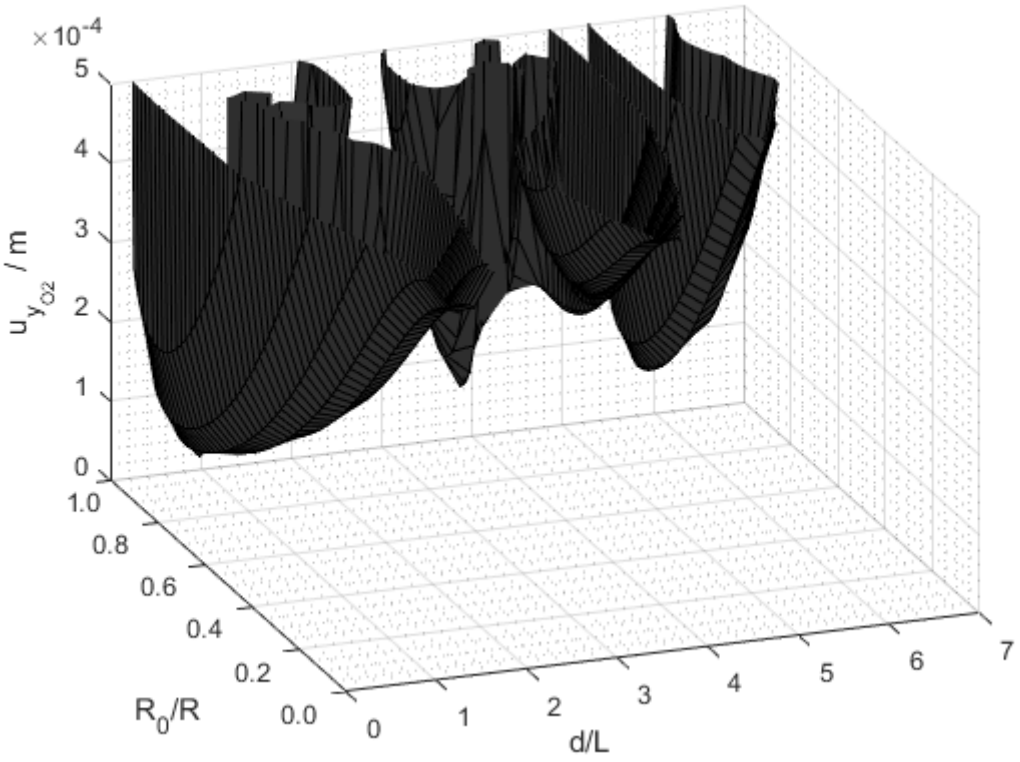

FIGURE 8.8: Uncertainty of the "y" coordinate of O_2' for the case of radially-placed Hall transducers, calculated with the analytical model for the coil number 2 of the ELI-Solenoid B.

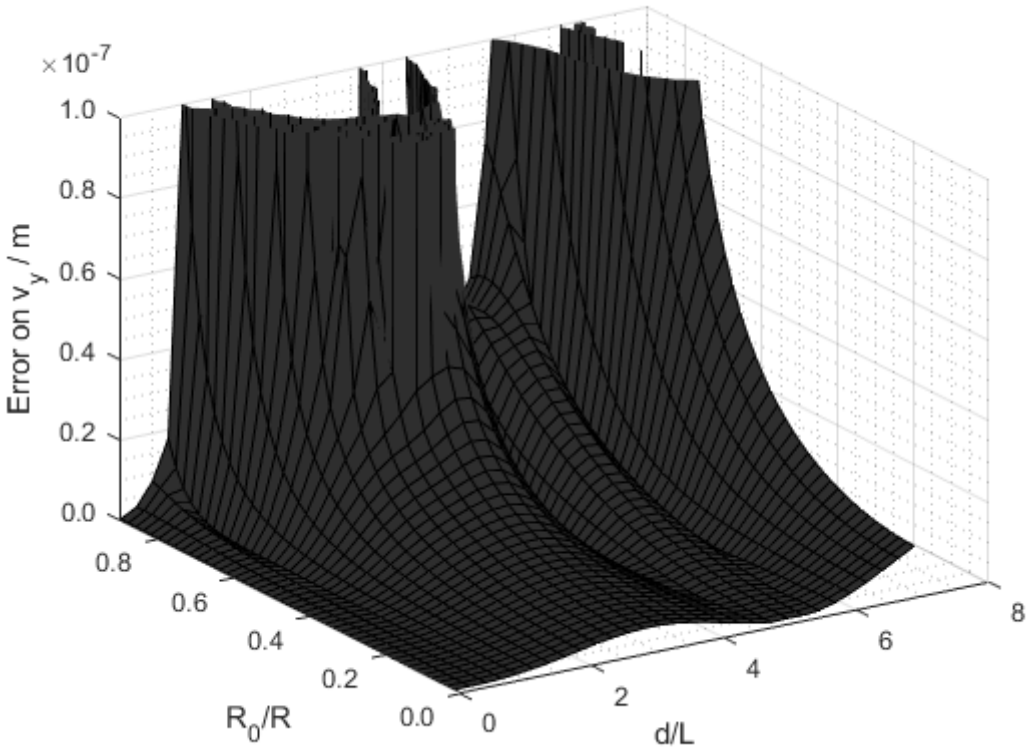

FIGURE 8.9: Measurement error, estimated with the analytical model for the $v_{y,2}$ axis parameters of the ELI-Solenoid B.

mainly depends on the first-order Taylor expansion adopted as local field model. In particular, if the misaligned magnetic axes are rotated of angles up to $\pi/1000$ and translated of 1/1000 times the length of a single coil (which are considered maximum misalignments in the application of interest), the measurement error was estimated to be always below $1\,\mu\mathrm{m}$. These results refer to simulations with both the analytical and FEM field model. Therefore, the method is validated for the case of interest because the maximum error is acceptable. For the sake of clarity, the measurement error is mapped at varying (R_0, d) in Fig. 8.9. It is shown that the error can also be below $0.1\,\mu\mathrm{m}$ for a proper transducers placement. However, the uncertainty minimization is the bottleneck of the method performance.

8.3 Conclusions

In this chapter, the proposed methods for monitoring in real time the magnetic axis misalignment in both single and multi-coil magnets have been validated on a challenging case study on the European project "ELI Nuclear Physics" (ELI-NP). The uncertainty in measuring the magnetic axis was studied with the aim of finding the optimal placing of the transducers, where the minimum uncertainty is achieved. In particular, simulations results, based on both analytical and finite-element models of the ELI-NP multi-coil solenoid, point to an uncertainty

below $100\,\mu\mathrm{m}$, for misalignment of the magnetic axes in rotation up to $\pi/1000$ and in translation of $1/1000$ times the length of a single coil. This uncertainty is limited by the Hall transducers technology, but has a potential for large improvement margins, because the measurement model error is below $1\,\mu\mathrm{m}$. The Hall transducer technology limits this uncertainty, but there are large margins for improvement because the estimated measurement model error is below $1\,\mu\mathrm{m}$. Further work will be directed towards an experimental evaluation of the method on an actual solenoid.

Chapter 9

Conclusions

The research presented in this thesis proposed novel solutions for characterizing magnetic materials and monitoring solenoids' magnetic axes, facing the recent challenges raised from the design of the next-generation particle accelerators.
An achievement of this work consisted in the design, prototyping and validation of a superconducting permeameter to characterize magnetic materials at a level of saturation of nearly 3 T and cryogenic temperature of 4.2 K. From these, the values at 1.94 K, the operational temperature of the LHC magnets, can be easily obtained. The solution consists of a customized measurement system that employs superconducting coils and is based on a flux-metric method. The main problem of employing superconducting coils, an undesired quench, has been addressed successfully by specific quench protection simulations, which has lead to a self-protected system. This measurement system was validated on a sample of ARMCO® Pure Iron for the iron yoke of the new HL-LHC magnets.
An approach based on a standard flux-metric method is proposed for the characterization of weakly magnetic materials. The method is particularly suitable for industrial series production: both the measurement duration and cost are drastically reduced in comparison with state–of–the–art VSM and AGFM methods. Furthermore, drawbacks related to the lack of accuracy for characterizing weakly magnetic materials due to its original conception for high permeability materials are overcome. This work can be considered as a proof of principle: the feasibility was proved and the principal uncertainty sources were pointed out and analyzed. The results are encouraging: the overall uncertainty is estimated to be less than a few percent, in repeated measurements under different drift correction assumptions.
The results in terms of uncertainty are not satisfying when μ_r goes below 1.1. Hence, for weakly magnetic materials with a relative magnetic permeability μ_r less than 1.05, a measurement system based on a novel magneto-metric method was developed and validated. The proposed method identifies the relative magnetic permeability of weakly magnetic materials immersed in a uniform, steady magnetic field. The proposed method solves an inverse problem starting from well-defined local magnetic measurements, followed by a numerical procedure, that is based on the finite element method. The method is general and could be used with different sample geometries (cube, bar, sphere, etc.) provided that appropriate 2D or 3D FE modeling is used. The case study shows good agreement between the estimated relative magnetic permeability and the reference value of

the sample: the accuracy of the proposed method is better than 3% for the susceptibility. This method, while still time-consuming at this stage, has been found to be effective for the difficult problem posed by weakly magnetic materials. In view of future series test campaigns, its efficiency could be improved by standardizing the setup and the shape of the sample.

At CERN, these measurement systems are currently employed to face an increasing number of requests concerning not only the magnetic characterization of materials for magnet components but also for shielding systems and compatibility of various components with high magnetic fields. In particular, in this thesis the characterizations of i) the ITER TF coils quench detection stainless steel, ii) ARMCO® Pure Iron for the construction of the superconducting magnet yokes for the HL-LHC upgrade, and iii) CRYOPHY for the cold magnetic shield material of the crab cavities cryomodule prototype were reported.

The unknown magnetic properties of the ITER TF coils quench detection stainless steel were analyzed by means of the proposed flux-metric method for weakly magnetic materials. The tests were helpful to the producer in order to identify the best annealing and cold work for achieving the lowest material magnetization. This is an essential requirement of the quench detection system, considering the extremely high field working conditions.

The magnetic properties of ARMCO® Pure Iron for HL-LHC magnet yokes were measured within annealing treatment sequences from 750 °C to 850 °C at operating temperatures of 4 K to 300 K by employing the split-coil, cryogenic and superconducting permeameters. It was demonstrated that annealing enhances the magnetic properties of pure iron, but this effect is volatile. It changes at cryogenic temperatures or if a mechanical stress is applied. At cryogenic temperatures, the low-temperature effects are predominant with respect to the effect of the strain. In general, the change in temperature has a more substantial effect on magnetic degradation than mechanical stress. Moreover, this study underlines that the effect of annealing is completely lost after the material is subject to a fast cooling to cryogenic temperatures. Different annealing procedures were used, but without stable results regarding grain size. Moreover, the annealing generated a surface problem of "scaling". For this reason and because the effect of annealing is completely lost after the material is subject to a fast cooling to cryogenic temperatures, the strong annealing phase (initially scheduled) was removed from the production process for the HL-LHC magnet production. The decision to stop annealing the laminations generated a reduction of roughly 9% of the cost. Tests performed before and after the application of mechanical stress were studied to validate the production process.

The behavior of the material for much higher magnetic fields (8.6 to 11 T according to the field distribution in HL-LHC magnets) was studied as well. The results present an initial magnetization and relative permeability curves up to nearly 450 kA/m, the higher value of saturation being 2.82 T. Similar levels of saturation are expected when the magnets will be powered at their nominal current values. The properties of this material have been compared with the material used for the LHC magnet yokes and with similar material from ROXIE database.

Significant discrepancies have been found, especially at higher levels of saturation. The common assumption that heavily-saturated steels with similar chemical composition behave precisely the same way has been proofed wrong. Finally, two case studies based on the new HL-LHC superconducting magnets and Finite Element Analysis have been presented. Whereas the dipole magnets are less affected, the quadrupoles transfer function shows a significant dependency on the magnet yoke properties. In conclusion, for magnet design, it is recommended to avoid to use *B-H* curves of similar materials or fitting equations but always characterize the employed material at its operating temperature and, especially, magnetic saturation level. The effects of temperature and mechanical strain on Cryophy's magnetic properties were studied in detail by employing the proposed flux-metric method for soft magnetic materials, proving the feasibility of its use as the cold magnetic shield material of the crab cavities cryomodule prototype. In particular, the results of the tensile tests show that the stress-strain behavior, within the chosen strain rates, is independent of the strain rate. Therefore, the magnetic properties after straining depend only on the induced strain and its direction, i.e. unidirectional strain creates anisotropic magnetic behavior. Since nickel has negative magnetostriction (i.e. an external magnetic field leads to a compressive strain in the material), the tensile stress in the direction of the magnetization can be seen as the worst-case scenario. Any tensile stress leads to a drastic decrease in the relative magnetic permeability. Care has to be taken during transport, assembly, and cool-down in order to not exceed the yield strength of 140 MPa within an adequate safety factor. However, owing to the rather low external field of about 50 A/m and the additional warm magnetic shield, localized mechanical deformation may be allowed. The results of the DC magnetic characterization showed a strong influence of temperature on Cryophy relative magnetic permeability. Experiments highlight a reduction of the relative permeability peak by a factor of two from room to cryogenic temperature, and then an extra variation of about one third when the temperature goes from 77 K to 4.2 K. Nevertheless, the relative magnetic permeability peak was found to be systematically higher than the magnetic shield design requirement of 100 000.

In this thesis, the importance of assessing the magnetic measurements of materials used for the construction of particle accelerator magnets was also discussed. First, it was shown that ferromagnetic materials used in the construction of yokes of several CERN magnets show different magnetic properties. Then, for standard steel for magnet yokes, a comparison between measurements and data from both in-house and the OPERA database highlighted several discrepancies in terms of B-H and relative permeability curves. This led to investigating how these different B-H curves could affect the results during the design of a magnet. This was assessed using OPERA simulation of a quadrupole magnet installed in the CERN North Area. The case study showed that even similar B-H curves could cause significant differences in the magnet's field quality. In conclusion, the characterization of magnetic materials is essential, not only for the quality control during the production phase of a magnet but also during its design phase.

Finally, a novel method for monitoring in real time the magnetic axis misalignment in single-coil was presented. Relying on a few measurements of the magnetic flux density, this method is primarily intended for applications where the magnet aperture is not accessible. The magnetic axis is determined by calculating the solenoid center and slope parameters. To this aim, a field model of the solenoid must also be employed to extract useful data for the calculations. The mathematical model of the method was derived for the case of radial or axial placement of the Hall transducers, and for the case of four or three transducers per solenoid side. A case study, based on the ELI-NP type B multi-coil solenoid, was considered. In particular, an analytical and an FE model of a single coil of the ELI-NP type B solenoid were employed to assess the uncertainty of the method and to obtain the optimal placement of the Hall transducers. Moreover, simulations were carried out with both models, to verify the capability of the method of estimating an imposed misalignment. Further work will be directed towards an experimental evaluation of the method on an actual solenoid.
A method for monitoring the coils alignment in multi-coil magnets was proposed. This proposal extends the previous method for measuring the magnetic axis of a single-coil solenoid during its operation. In both the cases, it was shown that a set of Hall transducers and a simple first-order Taylor expansion as a local field model are sufficient. In particular, for the multi-coil case, the magnetic field as a whole has been assumed as the superposition of the fields irradiated by the single coils. Simulations employing a proper field model were described to place transducers in order to minimize the measurement uncertainty. The results show that, if the misaligned magnetic axes are rotated by angles up to $\pi/1000$ and translated by 1/1000 times the length of a single coil, which are considered maximum misalignments in the application of interest, the uncertainty is below $100\,\mu\mathrm{m}$. This uncertainty is limited by the Hall transducer technology, but there are large margins for improvement because the estimated measurement model error is below $1\,\mu\mathrm{m}$.

Bibliography

[1] 2014. URL: www.aperam.com/alloysandspecialities/.../CRYOPHY_R_.pdf.

[2] A. A. E. Abdallh and L. Dupré. "A Unified Electromagnetic Inverse Problem Algorithm for the Identification of the Magnetic Material Characteristics of Electromagnetic Devices Including Uncertainty Analysis: A Review and Application". In: *IEEE Transactions on Magnetics* 51.1 (2015), pp. 1–10. ISSN: 0018-9464. DOI: 10.1109/TMAG.2014.2332978.

[3] J. Garcia Perez et al. "Metal Powder Report". In: *the international magazine of the powder metallurgy industry* ().

[4] J. Garcia Perez et al. "Performance of the room temperature systems for magnetic field measurements of the LHC superconducting magnets". In: *IEEE Transactions on Applied Superconductivity* (2006).

[5] L. Alberty. *Engineering Specification: Dressed Bulk Niobium Radio Frequency Crab Cavities*. Tech. rep. 2017.

[6] Daniela Alburquenque et al. "Tailoring the magnetic properties of Ni81Fe19 thin films by varying their thickness". In: *Journal of Magnetism and Magnetic Materials* 441 (2017), pp. 656 –659. ISSN: 0304-8853. DOI: https://doi.org/10.1016/j.jmmm.2017.06.066. URL: http://www.sciencedirect.com/science/article/pii/S0304885317311484.

[7] Giorgio Ambrosio. "Nb3Sn high field magnets for the high luminosity LHC upgrade project". In: *IEEE Transactions on Applied Superconductivity* 25.3 (2015), pp. 1–7.

[8] Giorgio Apollinari et al. "HINS linac front end focusing system R&D". In: *IEEE Transactions on Applied Superconductivity* 19.3 (2009), pp. 1368–1371.

[9] L Arnaudon et al. "The LINAC4 Project at CERN". In: CERN-ATS-2011-041 (2011), 4 p. URL: http://cds.cern.ch/record/1378473.

[10] P Arpaia, E De Matteis, and V Inglese. *Flexible test automation: a software framework for easily developing measurement applications*. Momentum Press, 2014.

[11] P Arpaia et al. "Measuring field multipoles in accelerator magnets with small-apertures by an oscillating wire moved on a circular trajectory". In: *Journal of Instrumentation* 7.05 (2012). URL: http://stacks.iop.org/1748-0221/7/i=05/a=P05003.

[12] P. Arpaia et al. "Proof-of-principle demonstration of a translating coils-based method for measuring the magnetic field of axially-symmetric magnets". In: *Journal of Instrumentation* 10.02 (2015), P02004. URL: http://stacks.iop.org/1748-0221/10/i=02/a=P02004.

[13] P Arpaia et al. "Vibrating-wire measurement method for centering and alignment of solenoids". In: *Journal of Instrumentation* 8.11 (2013), P11006. URL: http://stacks.iop.org/1748-0221/8/i=11/a=P11006.

[14] P Arpaia et al. "Vibrating-wire measurement method for centering and alignment of solenoids". In: *Journal of Instrumentation* 8.11 (2013), P11006. URL: http://stacks.iop.org/1748-0221/8/i=11/a=P11006.

[15] Pasquale Arpaia, Luca De Vito, and Mario Kazazi. "Uncertainty analysis of the magnetic field measurement by the translating coil method in axisymmetric magnets". In: *Metrologia* 53.6 (2016), p. 1317. URL: http://stacks.iop.org/0026-1394/53/i=6/a=1317.

[16] Pasquale Arpaia et al. "A software framework for developing measurement applications under variable requirements". In: *Review of Scientific Instruments* 83.11 (2012), p. 115103. DOI: 10.1063/1.4764664. eprint: http://dx.doi.org/10.1063/1.4764664. URL: http://dx.doi.org/10.1063/1.4764664.

[17] Pasquale Arpaia et al. "A software framework for developing measurement applications under variable requirements". In: *Review of Scientific Instruments* 83.11 (2012), p. 115103.

[18] *ASTM A342 / A342M-14, Standard Test Methods for Permeability of Weakly Magnetic Materials, ASTM International, West Conshohocken, PA*, 2014. URL: https://www.astm.org/Standards/A342.htm.

[19] R Aymar, P Barabaschi, and Y Shimomura. "The ITER design". In: *Plasma Physics and Controlled Fusion* 44.5 (2002), p. 519. URL: http://stacks.iop.org/0741-3335/44/i=5/a=304.

[20] S. Babic et al. "Toward the production of 50 000 tonnes of low-carbon steel sheet for the LHC superconducting dipole and quadrupole magnets". In: *IEEE Transactions on Applied Superconductivity* 12.1 (2002), pp. 1219–1222. ISSN: 1051-8223. DOI: 10.1109/TASC.2002.1018621.

[21] JR Barker. "An improved three-coil system for producing a uniform magnetic field". In: *Journal of Scientific Instruments* 27.7 (1950), p. 197.

[22] J Bauche and A Macpherson. *Estimate of Ambient Magnetic Field in the SPS Crab Cavity Location*. 2014.

[23] F. Bertinelli et al. "Production of Low-Carbon Magnetic Steel for the LHC Superconducting Dipole and Quadrupole Magnets". In: *IEEE Transactions on Applied Superconductivity* 16.2 (2006), pp. 1777–1781. ISSN: 1051-8223. DOI: 10.1109/TASC.2006.873236.

[24] J Billan. "Materials [particle accelerator magnets]". In: (1998). URL: https://cds.cern.ch/record/382437.

[25] Billan, J. "COERCIMETER FOR NON-DESTRUCTIVE MEASUREMENT OF THE COERCIVITY OF STEEL SHEETS". In: *J. Phys. Colloques* 45 (1984), pp. C1–965–C1–968. DOI: 10.1051/jphyscol:19841197. URL: https://doi.org/10.1051/jphyscol:19841197.

[26] J. Bisognano. *Progress Toward the Wisconsin Free Electron Laser*. Tech. rep. Thomas Jeerson National Accelerator Facility, Newport News, VA (United States), 2011.

[27] "Books Received". In: *American Scientist* 76.3 (1988), pp. 320–327. ISSN: 00030996. URL: http://www.jstor.org/stable/27855291.

[28] Lorenzo Bortot et al. "STEAM: A Hierarchical Cosimulation Framework for Superconducting Accelerator Magnet Circuits". In: *IEEE Transactions on Applied Superconductivity* 28.3 (2018), pp. 1–6.

[29] Luca Bottura et al. "Advanced accelerator magnets for upgrading the LHC". In: *IEEE Transactions on Applied Superconductivity* 22.3 (2012), pp. 4002008–4002008.

[30] Richard M Bozorth. "Magnetism". In: *Reviews of modern physics* 19.1 (1947), p. 29.

[31] O Bruning. *The High Luminosity LHC Project*. Tech. rep. 2015.

[32] Marco Buzio and Giuseppe Montenero. "Magnetic properties of co-wound 1.43 stainless steel tape for quench detection in ITER coils". In: *CERN TE-MSC Technical report* EDMS 1375853/2 (2014).

[33] Marco Buzio and Giuseppe Montenero. "Magnetic properties of co-wound 304 stainless steel tape for quench detection in ITER coils". In: *CERN TE-MSC Internal Note 2014-10* (2014).

[34] Robert C. O'Handley. *Modern magnetic materials : principles and applications / R.C. O'Handley.* Oct. 2018.

[35] G Ciovati et al. "Operation of a high-gradient superconducting radio frequency cavity with a non-evaporable getter pump". In: *Nuclear Instruments and Methods in Physics Research Section A: Accelerators, Spectrometers, Detectors and Associated Equipment* 842 (2017), pp. 92–95.

[36] V Coco et al. "Acceleration of Several Charge States of Lead Ion in CERN LINAC3". In: (2004). URL: https://cds.cern.ch/record/925515.

[37] IEC-International Electrotechnical Commission et al. *Methods of measurement of the magnetic properties of electrical steel strip and sheet by means of a single sheet tester*. 2010.

[38] International Electrotechnical Commission et al. *Magnetic materials—Part 2: methods of measurement of the magnetic properties of electrical steel sheet and strip by means of an Epstein frame*. 1996.

[39] International Electrotechnical Commission et al. *Methods of Measurement of the Magnetic Properties of Magnetic Sheet and Strip by Means of a Single Sheet Tester*. 2002.

[40] B. D. Cullity. "Introduction to Magnetic Materials". In: *Reading, MA: Addison Wesley* (1972).

[41] A Dael, O Napoly, and J Plouin. "Magnetic shielding: Our experience with various shielding materials". In: *Proceedings of SRF2013, Paris, France*. 2013.

[42] N Derby and S Olbert. "Cylindrical Magnets and Ideal Solenoids". In: *American Journal of Physics* 78 (3 2010). URL: https://arxiv.org/pdf/0909.3880.pdf.

[43] P. DeVore et al. "Light-weight flexible magnetic shields for large-aperture photomultiplier tubes". In: *Nuclear Instruments and Methods in Physics Research Section A: Accelerators, Spectrometers, Detectors and Associated Equipment* 737 (2014), pp. 222 –228.

[44] E. J. Di Marco et al. "Certification of Superconducting Solenoid-Based Focusing Lenses". In: *IEEE Transactions on Applied Superconductivity* 21.3 (2011), pp. 1817–1820. ISSN: 1051-8223. DOI: 10.1109/TASC.2010.2089489.

[45] E. J. Di Marco et al. "Superconducting Solenoid Lens for a High Energy Part of a Proton Linac Front End". In: *IEEE Transactions on Applied Superconductivity* 23.3 (2013). ISSN: 1051-8223. DOI: 10.1109/TASC.2012.2236374.

[46] Takeshi Dohmae et al. "Investigation of in-house superconducting radio-frequency 9-cell cavity made of large grain niobium at KEK". In: *Nuclear Instruments and Methods in Physics Research Section A: Accelerators, Spectrometers, Detectors and Associated Equipment* 875 (2017), pp. 1–9.

[47] *ELI - Extreme Light Infrastructure, Whitebook, Science and Technology with Ultra-Intense Lasers*. 2011. URL: https://eli-laser.eu/media/1019/eli-whitebook.pdf.

[48] *Evaluation of measurement data — Guide to the expression of uncertainty in measurement*. 2008. URL: https://www.bipm.org/utils/common/documents/jcgm/JCGM_100_2008_E.pdf.

[49] Y. Favennec et al. "Identification of magnetic parameters by inverse analysis coupled with finite-element modeling". In: *IEEE Transactions on Magnetics* 38.6 (2002), pp. 3607–3619. ISSN: 0018-9464. DOI: 10.1109/TMAG.2002.804815.

[50] P Ferracin, G Ambrosio, et al. "Development of MQXF: The Nb 3 Sn Low-β Quadrupole for the HiLumi LHC". In: *IEEE Transactions on Applied Superconductivity* 26.4 (2016), pp. 1–7.

[51] Enzo Ferrara, Elena Olivetti, et al. "Microstructure and magnetic properties of pure iron for cyclotron electromagnets". In: *Journal of Alloys and Compounds* 615 (2014). SI :ISMANAM 2013, S291 –S295. ISSN: 0925-8388. DOI: https://doi.org/10.1016/j.jallcom.2014.01.217.

[52] Fausto Fiorillo. *Measurement and characterization of magnetic materials*. North-Holland, 2004.

[53] Fausto Fiorillo. "Measurements of magnetic materials". In: *Metrologia* 47.2 (2010), S114.

[54] Simon Foner. "Versatile and Sensitive Vibrating-Sample Magnetometer". In: *Review of Scientific Instruments* 30.7 (1959), pp. 548–557. DOI: 10.1063/1.1716679. eprint: http://dx.doi.org/10.1063/1.1716679. URL: http://dx.doi.org/10.1063/1.1716679.

[55] JA García and M Rivas. "A quasi-static magnetic hysteresis loop measurement system with drift correction". In: *IEEE transactions on magnetics* 42.1 (2006), pp. 15–17.

[56] S.S. Grabchikov et al. "Effectiveness of the magnetostatic shielding by the cylindrical shells". In: *Journal of Magnetism and Magnetic Materials* 398 (2016), pp. 49 –53. ISSN: 0304-8853. DOI: https://doi.org/10.1016/j.jmmm.2015.08.122. URL: http://www.sciencedirect.com/science/article/pii/S0304885315305497.

[57] Martin R Gross. *Permeability standard*.

[58] ISO Guide. "98-3 (2008)". In: *Uncertainty of measurement–Part* 3 ().

[59] T. Hacib, M. R. Mekideche, and N. Ferkha. "Inverse Problem Methodology for the Measurement of the Electromagnetic Parameters Using MLP Neural Network". In: *International Journal of Electrical, Computer, Energetic, Electronic and Communication Engineering* 2.2 (2008), pp. 247 –252.

[60] Aerospace Structural Metals Handbook. "Volume 1". In: *Properties and Selection: Irons, Steels, and High Performance Alloys* 1 (2005).

[61] P. Harlet, F. Beco, and L. Renard. *Procédé de production d'acier doux*. Patent EP 0681031A1-B1. 1994. URL: https://patents.google.com/patent/EP0681031A1/en?oq=EP+0681031.

[62] V. Havlíček. "Digitally controlled single sheet tester". In: *Journal of Magnetism and Magnetic Materials* 112.1 (1992), pp. 103 –105. ISSN: 0304-8853. DOI: https://doi.org/10.1016/0304-8853(92)91124-C. URL: http://www.sciencedirect.com/science/article/pii/030488539291124C.

[63] S Henderson et al. "The spallation neutron source accelerator system design". In: *Nuclear Instruments and Methods in Physics Research Section A: Accelerators, Spectrometers, Detectors and Associated Equipment* 763 (2014), pp. 610–673.

[64] K.N. Henrichsen. "PERMEAMETER." In: *pp 735-9 of Proceedings of the Second International Conference on Magnet Technology, Oxford, England, 1967. Hadley, H. (ed.). Chilton, Eng., Rutherford Laboratory, 1967.* ().

[65] K.N. Henrichsen. "Permeameter". In: *II Int. Conf. on Magnet Technology* (1967).

[66] S Henry et al. "Characterisation of superconducting capillaries for magnetic shielding of twisted-wire pairs in a neutron electric dipole moment experiment". In: *Nuclear Instruments and Methods in Physics Research Section A: Accelerators, Spectrometers, Detectors and Associated Equipment* 763 (2014), pp. 155–162.

[67] Werner Herr and Bruno Muratori. "Concept of luminosity". In: (2006).

[68] Ingo Hofmann. "Performance of solenoids versus quadrupoles in focusing and energy selection of laser accelerated protons". In: *Phys. Rev. ST Accel. Beams* 16.4 (2013). DOI: 10.1103/PhysRevSTAB.16.041302. arXiv: 1301.6906 [physics.acc-ph].

[69] James L Horn and Craig A Grimes. "A 0.1–500 Hz analog thin film BH hysteresis loop tracer with automatic Y-axis drift correction". In: *Review of Scientific instruments* 68.2 (1997), pp. 1346–1347.

[70] IEC. *Magnetic materials-Part 4: Methods of measurement of dc magnetic properties of magnetically soft materials*. 2000.

[71] IEC-60402-2. "Magnetic materials—Part 2: Methods of measurement of the magnetic properties of electrical steel sheet and strip by means of an Epstein frame". In: *International Electrotechnical Commission Standard* (1996), pp. 60402–2.

[72] IEC-60402-4. "Magnetic materials—Part 4: Methods of measurement of DC magnetic properties of magnetically soft materials". In: *International Electrotechnical Commission Standard* (2000), pp. 60402–4.

[73] *INSTITUT DR. FOERSTER GMBH & CO. KG, Reutlingen Germany*. URL: www.foerstergroup.de.

[74] National Instruments. *NI 446x specifications*. URL: http://www.ni.com/pdf/manuals/373770j.pdf.

[75] National Instruments. *NI PXI-6289 specifications*. URL: http://www.ni.com/pdf/manuals/375222c.pdf.

[76] ISO-6892-1. "Metallic materials – Tensile testing – Part 1: Method of test at room temperature". In: *International Organization for Standardization* (2016), ISO6892–1.

[77] Y Kadi et al. "Status and Future Perspectives of the HIE-Isolde Project at CERN". In: *Conf. Proc.* C1205201.CERN-ATS-2012-251 (2012), MOOBA02. 4 p. URL: http://cds.cern.ch/record/1481516.

[78] Shuma Kawabata. "Magnetic permeability of the iron yoke in high field superconducting magnets". In: *Nuclear Instruments and Methods in Physics Research Section A: Accelerators, Spectrometers, Detectors and Associated Equipment* 329.1-2 (1993), pp. 1–8.

[79] Charles Kittel, Paul McEuen, and Paul McEuen. *Introduction to solid state physics*. Vol. 8. Wiley New York, 1996.

[80] A. Kponou et al. "Analysis of the magnetic field measured by a rotating hall probe in a solenoid to locate its magnetic axis". In: *Electron Beam Ion Sources and Traps and their Applications*. Ed. by K. Prelec. Vol. 572. American Institute of Physics Conference Series. July 2001, pp. 178–187. DOI: 10.1063/1.1390113.

[81] Manfred Krammer. "The update of the European strategy for particle physics". In: *Physica Scripta* 2013.T158 (2013), p. 014019.

[82] Kronmüller and S. Parkin. *Handbook of Magnetism and Advanced Magnetic Materials, vol. 4 – Novel Materials*. 2018.

[83] Tadeusz Kulik, Howard T Savage, and Antonio Hernando. "A high performance hysteresis loop tracer". In: *Journal of applied physics* 73.10 (1993), pp. 6855–6857.

[84] Vinit Kumar. "Understanding the focusing of charged particle beams in a solenoid magnetic field". In: *American Journal of Physics* 77.8 (2009), pp. 737–741.

[85] M. Küpferling, C. Appino, et al. "Magnetic hysteresis in plastically deformed low-carbon steel laminations". In: *Journal of Magnetism and Magnetic Materials* 316.2 (2007). Proceedings of the Joint European Magnetic Symposia, e854 –e857. ISSN: 0304-8853.

[86] R. E. Laxdal. "Review of magnetic shielding designs of low-beta cryomodules". In: *Proc. SRF, pp 800-807*. 2013.

[87] Rodrigo J. Leão et al. "Magnet alignment on a common girder: Development of a length artefact for measurement accuracy improvement". In: *Precision Engineering* 50 (2017), pp. 53 –62. ISSN: 0141-6359. DOI: https://doi.org/10.1016/j.precisioneng.2017.04.013. URL: http://www.sciencedirect.com/science/article/pii/S0141635916304160.

[88] *Low MU Permeability Indicator*. URL: http://www.severnengineering.com/lomu.htm.

[89] M. S. Lubell and A. S. Venturino. "Vibrating Sample Magnetometer". In: *Review of Scientific Instruments* 31.2 (1960), pp. 207–208. DOI: 10.1063/1.1716932. eprint: http://dx.doi.org/10.1063/1.1716932. URL: http://dx.doi.org/10.1063/1.1716932.

[90] Xing Luo et al. "Design and fabrication of the 2× 4-cell superconducting linac module for the free-electron laser". In: *Nuclear Instruments and Methods in Physics Research Section A: Accelerators, Spectrometers, Detectors and Associated Equipment* 871 (2017), pp. 30–34.

[91] M. Maciejewski. "Co-Simulation of Transient Effects in Superconducting Accelerator Magnets". In: *Lodz University of Technology, PhD Thesis, currently under review* (2018).

[92] "Magnetic induction measurements and identification of the permeability of Magneto-Rheological Elastomers using finite element simulations". In: *Journal of Magnetism and Magnetic Materials* 404.Supplement C (2016), pp. 205 –214. ISSN: 0304-8853. DOI: https://doi.org/10.1016/j.jmmm.2015.12.003.

[93] *Magnetic Measurements on the Beam Transport Quadrupoles for the CERN PS*. URL: https://edms.cern.ch/document/864174/1.

[94] "Magnetic shielding effect from multiple configurations of open-type magnetic shielding walls compared to solid plates". In: *Journal of Magnetism and Magnetic Materials* 322.9 (2010). Proceedings of the Joint European Magnetic Symposia, pp. 1540 –1543. ISSN: 0304-8853. DOI: https://doi.org/10.1016/j.jmmm.2009.07.058.

[95] Helene Mainaud Durand et al. "PACMAN Project: A New Solution for the High-accuracy Alignment of Accelerator Components". In: *Proceedings, 7th International Particle Accelerator Conference (IPAC 2016): Busan, Korea, May 8-13, 2016*. 2016, MOOCB01. DOI: 10.18429/JACoW-IPAC2016-MOOCB01. URL: http://inspirehep.net/record/1469516/files/moocb01.pdf.

[96] G Manfreda, L Rossi, and M Sorbi. "MATPRO upgraded version 2012: a computer library of material property at cryogenic temperature". In: *Tech. Rep. INFN-12-04/MI* (2012).

[97] M Masuzawa, A Terashima, and K Tsuchiya. "Magnetic properties of shielding materials for superconducting cavities". In: *IEEE Transactions on Applied Superconductivity* 22.3 (2012), pp. 3500104–3500104.

[98] M Masuzawa, K Tsuchiya, and A Terashima. "Study of magnetic shielding materials and fabrication of magnetic shield for superconducting cavities". In: *IEEE Transactions on Applied Superconductivity* 24.3 (2014), pp. 1–4.

[99] M Masuzawa et al. "Magnetic shielding effect at cryogenic temperature evaluated for the STF cryomodule". In: *IEEE Transactions on Applied Superconductivity* 20.3 (2010), pp. 1773–1776.

[100] D. Meeker. *Finite Element Method Magnetics, Version 4.2 User's Manual*. URL: http://www.femm.info/wiki/HomePage.

[101] Metrolab. *NMR precision teslameter PT2025*. URL: https://www.metrolab.com/products/pt2025/.

[102] H. Nishio, K. I. Machida, and K. Ozaki. "More Accurate Hysteresis Curve for Large Nd-Fe-B Sintered Magnets Employing a Superconducting Magnet-Based Vibrating Sample Magnetometer". In: *IEEE Transactions on Magnetics* 53.4 (2017), pp. 1–6. ISSN: 0018-9464. DOI: 10.1109/TMAG.2016.2641399.

[103] *Norma database design Q200*. URL: https://norma-db.web.cern.ch/magdesign/idcard/350/.

[104] R OPERA. *Cobham Technical Services*.

[105] P. N. Ostroumov, G. V. Romanov, and A. P. Fateev. "Increase in injection efficiency ina a high current linear proton accelerator". In: *Tech. Phys.* 25 (1980), pp. 710–713.

[106] PN Ostroumov. "Physics design of the 8 GeV H-minus linac". In: *New Journal of Physics* 8.11 (2006), p. 281.

[107] KJ Overshott and IR Smith. "A solenoid with a nearly uniform axial magnetic field". In: *Journal of Scientific Instruments* 41.8 (1964), p. 507.

[108] K. H. Park et al. "Field Mapping System for Solenoid Magnet". In: *AIP Conference Proceedings* 879.1 (2007), pp. 260–263. DOI: 10.1063/1.2436051. eprint: https://aip.scitation.org/doi/pdf/10.1063/1.2436051. URL: https://aip.scitation.org/doi/abs/10.1063/1.2436051.

[109] K. H. Park et al. "Field Mapping System for Solenoid Magnet". In: *AIP Conference Proceedings* 879.1 (2007), pp. 260–263. DOI: 10.1063/1.2436051. eprint: http://aip.scitation.org/doi/pdf/10.1063/1.2436051. URL: http://aip.scitation.org/doi/abs/10.1063/1.2436051.

[110] Plansee. *Tungsten heavy alloys description*. URL: https://www.plansee.com/en/materials/tungsten-heavy-metal.html.

[111] R Pouladian-Kari et al. "A multiple coil solenoid to provide an axial magnetic field with near-linear gradient". In: *Journal of Physics E: Scientific Instruments* 21.6 (1988), p. 557.

[112] L. Pust and D. Dlouhy. "Virtual additive moments measured by a vibrating sample magnetometer on superconducting thin films". In: *Superconductor Science and Technology* (1996), pp. 814–821.

[113] L. H. de Figueiredo R. Ierusalimschy. *Lua 5.1 Reference Manual*. Aug. 2006. URL: https://www.lua.org/manual/5.1/.

[114] Alberto Riminucci et al. "Analytical balance-based Faraday magnetometer". In: *Journal of Applied Physics* 121.9 (2017), p. 094701. DOI: 10.1063/1.4977719. eprint: http://dx.doi.org/10.1063/1.4977719. URL: http://dx.doi.org/10.1063/1.4977719.

[115] Lucio Rossi, O Brüning, et al. "High luminosity large hadron collider". In: *European Strategy Preparatory Group-Open Symposium, Krakow*. 2012.

[116] Lucio Rossi and Massimo Sorbi. "QLASA: A computer code for quench simulation in adiabatic multicoil superconducting windings". In: *Nat. Inst. of Nucl. Phys.(INFN), Rome, Italy, Tech. Rep. TC-04-13* (2004).

[117] Stephan Russenschuck. *Field computation for accelerator magnets: analytical and numerical methods for electromagnetic design and optimization*. John Wiley & Sons, 2011.

[118] Stephan Russenschuck. *ROXIE: the Routine for the Optimization of Magnet X-sections, Inverse Field Computation and Coil End Design*. Tech. rep. CERN, 1993.

[119] S. Sah, G. Myneni, and J. Atulasimha. "Experimental Characterization of Magnetic Materials for the Magnetic Shielding of Cryomodules in Particle Accelerators". In: *IEEE Transactions on Magnetics* 52.2 (2016), pp. 1–6. ISSN: 0018-9464. DOI: 10.1109/TMAG.2015.2494862.

[120] Sanjay Sah, Ganapati Myneni, and Jayasimha Atulasimha. "Experimental characterization of magnetic materials for the magnetic shielding of cryomodules in particle accelerators". In: *IEEE Transactions on Magnetics* 52.2 (2016), pp. 1–6.

[121] Morten Sales et al. "Three Dimensional Polarimetric Neutron Tomography of Magnetic Fields". English. In: *Scientific Reports* 8 (Feb. 2018). ISSN: 2045-2322. DOI: 10.1038/s41598-018-20461-7.

[122] F Savary et al. “The 11 T dipole for HL-LHC: Status and plan”. In: *IEEE Transactions on Applied Superconductivity* 26.4 (2016), pp. 1–5.

[123] C. Sborchia and Y. Fu. “Design and Specifications of the ITER TF Coils”. In: *Design and Specifications of the ITER TF Coils, IEEE transactions on applied superconductivity* 18.2 (2008).

[124] S Sgobba. “Physics and measurements of magnetic materials”. In: *arXiv preprint arXiv:1103.1069* (2011).

[125] S Sgobba. “Physics and measurements of magnetic materials”. In: *CAS 2009 - CERN Accelerator School: Magnets, Proceedings* (Mar. 2011).

[126] S. Sgobba and G. Hochoertler. “A new non-magnetic stainless steel for very low temperature applications”. In: *Proceedings of the International Congress Stainless Steel 1999: Science and Market* 2 (1999), pp. 391–401.

[127] *Specification for Quadrupole Magnets*. URL: https://edms.cern.ch/document/1686577/1.

[128] PT Squire et al. “Digital MH plotter for low-coercivity metallic glasses”. In: *Journal of Physics E: Scientific Instruments* 21.12 (1988), p. 1167.

[129] RM Strnat, MJ Hall, and MS Masteller. “Precision and accuracy study on measurement of soft magnetic properties using DC hysteresigraphs”. In: *IEEE transactions on magnetics* 43.5 (2007), pp. 1884–1887.

[130] Edvard Stubberud. “QLASA in STEAM”. In: *CERN EDMS note 1976188* (2018).

[131] P M special measuring systems. *MACC^{PLUS} 2 specifications*. URL: http://www.pm-sms.com/files/2016/02/Specifications-MACC-2-plus.pdf.

[132] *Technical Specification for the Supply of Low Carbon Steel Sheets for the Superconducting Magnets of the HL-LHC*. EDMS No - 1498836. 2015.

[133] Niklas Templeton et al. “Design of the Thermal and Magnetic Shielding for the LHC High Luminosity Crab-Cavity Upgrade”. In: (2015).

[134] Ezio Todesco et al. “A first baseline for the magnets in the high luminosity LHC insertion regions”. In: *IEEE Transactions on Applied Superconductivity* 24.3 (2014), pp. 1–5.

[135] A.V. Trukhanov et al. “AC and DC-shielding properties for the Ni80Fe20/Cu film structures”. In: *Journal of Magnetism and Magnetic Materials* 443 (2017), pp. 142 –148. ISSN: 0304-8853. DOI: https://doi.org/10.1016/j.jmmm.2017.07.053. URL: http://www.sciencedirect.com/science/article/pii/S0304885317315743.

[136] Slawomir Tumanski. *Handbook of magnetic measurements*. CRC, 2011.

[137] Baichuan Wang et al. "Fiducialization of the small-aperture quadrupoles based on the vibrating wire method". In: *Nuclear Instruments and Methods in Physics Research Section A: Accelerators, Spectrometers, Detectors and Associated Equipment* 812 (2016), pp. 37 –42. ISSN: 0168-9002. DOI: https://doi.org/10.1016/j.nima.2015.12.025. URL: http://www.sciencedirect.com/science/article/pii/S016890021501596X.

[138] H Watanabe. "Further examination of the transient hot-wire method for the simultaneous measurement of thermal conductivity and thermal diffusivity". In: *Metrologia* 39.1 (2002), p. 65. URL: http://stacks.iop.org/0026-1394/39/i=1/a=9.

[139] J. Wenninger. *Linear Imperfections*. https://cas.web.cern.ch/sites/cas.web.cern.ch/files/lectures/chavannes-de-bogis-2017/linearimperfections-casjwfeb17.pdf. 2017.

[140] D.B. Williams and C.B. Carter. *Transmission Electron Microscopy: A Textbook for Materials Science. Diffraction. II*. Springer, 1996. ISBN: 9780306452475.

[141] Zdzisław Włodarski. "Analytical description of magnetization curves". In: *Physica B: Condensed Matter* 373.2 (2006), pp. 323–327.

[142] Carlo Zanoni et al. "The crab cavities cryomodule for SPS test". In: *Journal of Physics: Conference Series*. Vol. 874. 1. IOP Publishing. 2017, p. 012092.

[143] Lefu Zhang and Seiki Takahashi. In: *"Magnetic Study of martensitic transformation in austenitic stainless steel by low field hysteresis loops analysis", AIP conference proceeding 760, 1576* (2005).

[144] Yimei Zhu. "Modern Techniques for Characterizing Magnetic Materials". In: *Modern Techniques for Characterizing Magnetic Materials, by Y. Zhu. XX, 604 p. 407 illus., 53 in color. 1-4020-8007-7. Berlin: Springer, 2005.* (Jan. 2005).

List of Figures

List of Tables